NNT : 2017SACLS210

THÈSE DE DOCTORAT
DE L'UNIVERSITÉ PARIS-SACLAY
PREPARÉE À L'UNIVERSITÉ PARIS-SUD
AU SEIN DU CEA/IRFU

ÉCOLE DOCTORALE N°576
Particules Hadrons Énergie et Noyau : Instrumentation, Image, Cosmos et Simulation (PHENIICS)
Spécialité de doctorat : physique des particules

Par

M. Simon BOUTEILLE

DÉVELOPPEMENT ET APPLICATIONS DE DÉTECTEURS GAZEUX À MICRO-PISTES POUR LA TOMOGRAPHIE MUONIQUE

Thèse présentée et soutenue au CEA Saclay, le 11 septembre 2017

Composition du jury :

Pr. Etienne Augé	*Vice-Président, Université Paris-Sud*	Président du jury
Pr. Lee Thompson	*Professor, University of Sheffield*	Rapporteur
Dr. Jacques Marteau	*Maître de conférences, CNRS/IN2P3/IPNL*	Rapporteur
Pr. Ioannis Giomataris	*Ingénieur de recherche, CEA/DRF/IRFU/DEDIP*	Examinateur
Pr. Arturo Menchaca Rocha	*Professor, Universidad Nacional Autónoma de México*	Examinateur
Dr. Cristiano Bozza	*Researcher, Università di Salerno*	Examinateur
Dr. Sébastien Procureur	*Ingénieur de recherche, CEA/DRF/IRFU/DPhN*	Directeur de thèse

Abstract

This thesis describes the first attempts to perform both absorption and scattering muon tomography using high granularity Micromegas detectors. This imaging technique using the free, available and harmless cosmic ray muons radiation shows great possibilities to study various sized objects. In order to make compact and precise portable devices, using one channel of electronics per readout pattern is not possible. To avoid this problem multiplexed detectors have been designed, extensively tested and used in numerous conditions. The latest developments in Micromegas design have been used such as the genetic multiplexing and the 2D strip readout using a resistive layer. The prototypes made were able to achieve a $300\,\mu\mathrm{m}$ resolution at the scale of $50\,\mathrm{cm}$ while using only 61 channels of electronics.

Using these detectors, muography data taking campaigns have been performed both in the semi-controlled environment of the Saclay site of CEA and in the wild of the Giza plateau in Egypt. These two campaigns succeeded in imaging the CEA Saclay water tower and the Khufu's pyramid despite the extreme conditions endured by the Micromegas muon telescopes. Large temperature variations of a few tens of Kelvin have been recorded together with a stable operation *i.e.* an even gain ensuring a steady self-triggering system. This stability was achieved using high voltage variations with respect to the environmental conditions. Together with this very first worldwide operation of a Micromegas-based tracker outside a laboratory, scattering muographies have also been done. A small setup imaging handheld objects performed well in separating various materials in time scales of the order of the day while a bigger $1\,\mathrm{m}^2$ setup allowing the scan of a full container was successfully operated. The inversion of the ill-posed problem of the muon scattering was performed using the crude PoCA method and the maximum likelihood one described in the literature.

Résumé

Cette thèse décrit les premiers essais de tomographie muonique par absorption et par déviation en utilisant des détecteurs Micromegas à haute granularité. Cette technique d'imagerie utilisant les rayons cosmiques gratuits, sans dangers et disponibles partout a démontré sa capacité à imager des objets de tailles variées. Afin de construire des outils compacts, précis et portables, utiliser une voie d'électronique pour lire chaque motif de lecture est impossible. Pour éviter ce problème, des détecteurs multiplexés ont été conçus, testés et mis en situation dans différentes conditions. Il a été tiré parti des dernières améliorations concernant le détecteur Micromegas telles que le multiplexage génétique ou la lecture 2D par pistes sous une couche résistive. Les prototypes qui ont été fabriqués ont atteint une résolution de 300 µm sur une surface d'un quart de mètre carré en ne nécessitant que 61 voies d'électronique.

Grâce à ces détecteurs, des campagnes de prise de données ont été réalisées, à la fois dans l'environnement semi-contrôlé du centre CEA de Saclay et sur le plateau de Gizeh en Egypte. Ces deux campagnes ont permis d'imager avec succès le château d'eau du CEA Saclay ainsi que la pyramide de Khéops et ce malgré les conditions extrêmes que les télescopes à muon ont endurées. Des variations de température de plusieurs dizaines de Kelvin ont été enregistrées alors que l'acquisition de données se déroulait de manière stable, c'est-à-dire que les variations du gain n'impactaient pas le système d'auto déclenchement. Cette stabilité a été rendue possible grâce à un ajustement des hautes tensions vis-à-vis des conditions environnementales. Cela constitue la première mondiale concernant le fonctionnement d'un dispositif de reconstruction de traces à base de Micromégas en extérieur. En parallèle des expériences de muographie par déviation ont été menées. Un dispositif imageant des objets de petite taille est capable de distinguer divers matériaux sur une échelle de temps de l'ordre d'une journée. Une plus grande installation a permis d'imager un conteneur entier. La résolution du problème inverse a été faite en utilisant à la fois l'algorithme simple dit du PoCA ainsi que celui de maximisation de vraisemblance proposé dans la littérature.

Acknowledgements

First, I want to thank my adviser Sébastien Procureur who introduced me to the great world of the MPGDs. Moreover, his knowledge in science History is endless. Like he pointed out during the defence, our relationship was more like between colleagues than between a student and his adviser. For teaching me how to correctly compute a cross product, I will always help him for 3D geometry problems.

These three years work could not be as fruitful as it was without all the muon team. David Attié who spent a lot of time in the projects despite the fact that he is involved in half of the projects at DEDIP. Irakli Mandjavidze, "le génie", who must have a time turner to be able to do so much work. However, he is always ready to tell one of his work anecdotes around a glass of beer. Without him, the electronics part of our instruments would never work properly. I also want to thank Marc Riallot for his great mechanical designs of the instruments and of course Patrick Magnier whose little tips and tricks allowed us to assemble everything correctly and in no time. I hope his interest for muography will last so that he can take part of the rise of this technology. Also, I want to thank the new comer, Christopher Filosa, for his good mood in all circumstances.

I am also grateful to everybody at DPhN, especially its direction: Heloïse Goutte then Franck Sabatié and Jacques Ball who supported the muography project even though it did not fit in the primary mission of the department as well as the head of the DEDIP, Eric Delagnes. These three years would not have been as pleasing as they have been without the passionate discussions around a meal or a cake with the members of LSN I already mentioned and Hervé Moutarde and Maxime Defurne.

Moreover, people from DEDIP contributed a lot in the success of this work, especially Maxence Vandenbroucke with which I had many discussions about Micromegas (I hope his museum is growing well) and geek tips. But also Stephan Aune and Mariam Kebbiri who managed to build the designed prototypes at the "labo bulk", the electronics engineers Denis Calvet and Pascal Baron who were always available to help solving the multiple problems we encountered.

The ScanPyramids mission would not be such a success without the work done by HIP and in particular Mehdi Tayoubi who had the will to make it happen and Vincent Steiger who achieved to prepare everything such that the science team could work in Egypt.

The NRBC program within the CEA allowed us to build a collaboration with colleagues from DRT, in particular Thomas Dautremer and Frédérick Carrel who were very helpful regarding the image reconstruction in scattering muography.

At last, I want to thank my committee for their helpful remarks and their implication towards the development of this new imaging technique.

Contents

List of Figures

List of Tables

List of Abbreviations

ASIC	**A**pplication **S**pecific **I**ntegrated **C**ircuit
CEA	**C**ommissariat à l'**É**nergie **A**tomique (atomic energy agency)
DREAM	**D**eadtime-less **R**eadout **E**lectronics **A**SIC for **M**icromegas
FEU	**F**ront-**E**nd **U**nit
IRFU	**I**nstitut de **R**echerche sur les lois **F**ondamentales de l'**U**nivers (fundamental laws of the universe research institute)
M^{3}	**M**ultiplexed **M**icromegas for **M**uon tomography experiment
MG	**M**ulti**G**en
Micromegas	**Micro-me**sh **ga**seous **s**tructure
MPGD	**M**icro-**P**attern **G**aseous **D**etector
PCB	**P**rinted **C**ircuit **B**oard
PoCA	**Po**int of **C**losest **A**pproach
SPhN	**S**ervice de **Ph**ysique **N**ucléaire (nuclear physics division)
SEDI	**S**ervice d'**É**lectronique, **D**étecteur et **I**nformatique (electronics, detectors and computing division)
TCM	**T**ime and **C**lock **M**odule
TPC	**T**ime **P**rojection **C**hamber
WatTo	**Wat**er **To**wer experiment

Physical Constants

Speed of Light	$c = 2.997\,924\,58{\times}10^{8}\,\mathrm{ms^{-1}}$ (exact)
Muon life-time	$\tau_\mu = 2.197\,\mu\mathrm{s}$
Muon mass	$m_\mu = 105.66\,\mathrm{MeV}$
Argon molecular mass	$M_{Ar} = 39.95\,\mathrm{gmol^{-1}}$
Air molecular mass	$M_{air} = 28.96\,\mathrm{gmol^{-1}}$
Normal pressure	$P_N = 1024\,\mathrm{hPa}$
Normal temperature	$T_N = 293.15\,\mathrm{K}$ (20 °C)
Avogadro's number	$N_A = 6.022{\times}10^{23}\,\mathrm{mol^{-1}}$
Electron mass	$m_e = 0.511\,\mathrm{MeV/c^2}$
Electron charge	$e = 1.602{\times}10^{-19}\,\mathrm{C}$
Permittivity of free space	$\epsilon_0 = 8.854{\times}10^{-12}\,\mathrm{Fm^{-1}}$ (exact)
Boltzmann's constant	$k_B = 8.617{\times}10^{-5}\,\mathrm{eVK^{-1}}$ $(1.381{\times}10^{-23}\,\mathrm{JK^{-1}})$

List of Symbols

E	energy	eV (J)
$\mathcal{P}$	power	W (kgm^{2}s^{-3})
P	pressure	Pa (kgm^{-1}s^{-2})
P_a	atmospheric pressure	Pa
p	momentum	MeV/c (kgms^{-1})
T	temperature	K (°C)
x, y, z	cartesian coordinates	m
q	particle charge	
Z	atomic charge	
A	atomic number	
s	curvilinear abscissa	m
Q	charge	C (As)
Q_V	volumetric flow	Lh^{-1}
a_P	voltage to pressure correcting factor	VPa^{-1} (m^{3}A^{-1}s^{-1})
a_T	voltage to temperature correcting factor	VK^{-1} (kgm^{2}K^{-1}A^{-1}s^{-3})
a_S	voltage to signal amplitude feedback factor	V/ADC
U	voltage	V (kgm^{2}A^{-1}s^{-3})
v	velocity	ms^{-1}
X_0	radiation length	m
w_i	ionization potential	eV (J)
d	distance	m
G	gain	
S/N	signal over noise ratio	
C	capacitance	F (s^{4}A^{2}kg^{-1}m^{-2})
S	signal amplitude	ADC
n	material amount	mol
t	time	s
$\mathcal{A}$	area	m^2
$\mathcal{E}$	acceptance factor	
$\mathbb{P}$	probability	
$\mathscr{P}$	plane	
H	Heaviside function	
β	velocity wrt. c	$\frac{v}{c}$
γ	Lorentz factor	$\frac{1}{\sqrt{1-\beta^2}}$

θ	zenith angle	rad
φ	azimuth angle	rad
ϕ	particle flux	$\mathrm{s^{-1}sr^{-1}m^{-2}}$
ρ	volumetric mass	$\mathrm{kgm^{-3}}$
ρ_n	molecular density	$\mathrm{m^{-3}}$
ϱ	opacity	$\mathrm{kgm^{-2}}$
χ	radiation length	m
Ω	solid angle	sr
ϵ	efficiency	
α_T	Townsend coefficient	$\mathrm{m^{-1}}$
$\alpha_{V,T}$	relative volume change with the temperature	$\mathrm{K^{-1}}$
$\alpha_{V,P}$	relative volume change with the pressure	$\mathrm{Pa^{-1}}$ $(\mathrm{ms^2kg^{-1}})$
λ	mean free path	m
Σ	correlation matrix	

À ma mère

Synthèse

La muographie utilise les muons issus du rayonnement cosmique naturel qui a été mis en évidence par Hess, Wulf et Pacini au début du XX$^{\text{ème}}$ siècle. Ce rayonnement provient de particules chargées produites essentiellement dans des sources externes au système solaire. La majeure partie est composée de protons et, dans une moindre mesure, de noyaux d'Hélium, qui voyagent pendant des millions d'années avant d'arriver à proximité de la Terre. Ce flux extra solaire, au vu de sa charge, subi le champ magnétique solaire et terrestre. Ce phénomène introduit une dépendance entre l'énergie, ou plutôt la rigidité, et l'angle d'incidence avec lequel le rayonnement cosmique primaire va heurter l'atmosphère. Lorsque cela se produit, la collision avec les atomes de la haute atmosphère va engendrer une cascade de réactions. Celles-ci produisent majoritairement des pions et des kaons. Ces particules instables vont finalement se désintégrer en photons, électrons, neutrinos et muons. La figure I.3 est une représentation d'une gerbe cosmique simulée à l'aide du logiciel CORSIKA. Si presque la totalité des photons et électrons sont absorbés avant d'arriver à proximité de la surface terrestre, les muons et les neutrinos vont même pouvoir pénétrer le sol. En prenant en compte ces différents effets : les champs magnetiques en présence et les interactions avec l'atmosphère, il est possible de construire des modèles de flux de muon dépendant de son énergie et de son angle zénithal comme l'a fait Gaisser. Cependant ces modèles sont ajustés empiriquement pour reproduire au mieux les diverses observations qui ont été faites. Les variations temporelles de ce flux sont principalement dues aux variations du champ magnétique solaire affectant les rayons cosmiques primaires et les variations de l'état thermodynamique de l'atmosphère affectant le transport des muons. En effet, il y a une anti-corrélation entre la pression atmosphérique et le flux de muon à la surface de la Terre. Cela est lié à la perte d'énergie du muon lorsqu'il traverse de la matière. Au long de leur parcours, les muons vont interagir avec le milieu qui les entourent (en frappant les noyaux d'atomes par exemple). Les deux principales sources de perte d'énergie sont les processus radiatifs et la perte d'énergie par ionisation/excitation qui est modélisée par l'équation de Bethe. Ces pertes d'énergie qui dépendent principalement de la densité du milieu traversé peuvent engendrer l'absorption des muons par la matière ou leur désintégration. Microscopiquement, la matière est un milieu chargé qui établit donc des champs électriques qui vont également influencer la trajectoire du muon, non pas en le freinant mais en le déviant de sa course originelle. Puisque cet effet dépend de la force des champs électrique en présence, plus un milieu contient des éléments à haut numéro atomique Z, plus il va pouvoir engendrer de grandes déviations.

Afin d'utiliser ces propriétés intéressantes des muons pour faire de la muographie, il faut pouvoir les détecter. Pour cela, on peut utiliser des détecteurs comme les Micromégas. Ils font partie de la famille des détecteurs gazeux à micro-motif. L'adjectif gazeux vient de la nature de l'interaction entre le détecteur et le muon : ce dernier va ioniser le gaz à l'intérieur du détecteur et c'est grâce à cette formation de paires électrons-ions que l'on va pouvoir induire un signal. En effet, grâce à un premier champs électrique, ces électrons vont migrer vers une micro-grille qu'ils vont traverser. Derrière celle-ci, un deuxième champs électrique va accélerer les électrons, ils vont alors acquérir une énergie suffisante pour pouvoir ioniser le gaz à leur tour. Il s'en suit un phénomène d'avalanche dit de Townsend. Cela permet d'amplifier le signal pour qu'il soit suffisamment fort pour être traité par l'électronique de lecture. Ce signal est induit sur des micro-motifs constituants l'anode du détecteur. En effet, comme le théorème de Shockley-Ramo le décrit, cette avalanche d'électrons se déplaçant vers l'anode induit une charge sur cette dernière. Ces principes de fonctionnement sont résumés Figure II.4. Depuis son invention en 1996, ce détecteur n'a pas cessé d'évoluer. Afin de garantir un espace d'amplification le plus homogène possible, il faut contrôler la hauteur de la micro-grille vis-à-vis de l'anode. Pour cela, en 2006, est apparu le "bulk". C'est une méthode de fabrication du Micromégas issu de l'industrie du circuit imprimé qui permet de capturer la micro-grille dans du plastique photosensible d'épaisseur régulière. Grâce à cette propriété, il va être possible d'imager des plots qui vont soutenir la micro-grille et d'éliminer le reste du plastique pour créer l'espace d'amplification. Les différentes étapes de fabrication sont présentées Figure II.7. De plus, à cause du champ d'amplification, des étincelles peuvent apparaître entre la micro-grille et l'anode. Ce phénomène, en plus de pouvoir endommager le détecteur, est aussi responsable de temps mort dans le détecteur. En effet, le transfert de charge induit par l'étincelle va faire baisser la différence de potentiel entre la micro-grille et l'anode et donc l'intensité du champ d'amplification ce qui entraine une baisse du gain. Pour supprimer ce problème, il est posible d'utiliser une anode résistive. Cela va ralentir l'évacuation des charges et donc enrayer le processus de formation de l'étincelle. Dans ce cas, la collection du signal ne se fait plus sur l'anode elle-même mais sur les micro-motifs placés en dessous. Un couplage capacitif permet la transmission du signal entre ces deux couches. Grâce à cet effet, il est même possible de placer plusieurs épaisseurs de motifs sensibles. Par exemple, deux couches de pistes perpendiculaires peuvent être utilisées à la place d'une seule couche de pixels. Cela permet de réduire drastiquement le nombre de canaux d'électronique nécessaire à la lecture d'une surface donnée à résolution constante comme le montre les équations II.6 à II.9. Finalement, en 2012, la méthode du multiplexage génétique a été inventée. Elle permet d'utiliser la redondance du signal déposé par une particule pour réduire la quantité d'électronique nécessaire pour lire un détecteur. En effet, une particule induit presque toujours un signal sur au moins deux pistes adjacentes. Il est alors possible de relier chacun des canaux d'électronique à plusieurs pistes tout en respectant la règle suivante : pour tout couple de canaux, il doit n'exister qu'une seule position pour laquelle les deux canaux sont reliés à deux pistes adjacentes. Grâce à ces avancées, pendant cette thèse, deux prototypes successifs ont été développés. Ce sont des Micromégas résistifs et multiplexés fournissant une information 2D grâce à deux couches perpendiculaires de pistes de lecture. Ils sont baptisés MultiGen 2D et ont été testés de manière intensive. Leur efficacité est supérieure à 95 % et leur résolution spatiale inférieure à 300 µm pour une granularité de 480 µm et un facteur de multiplexage de 15. Même si cette résolution reste bien supérieure à la limite théorique de 140 µm, le passage de la première à la deuxième version du MultiGen 2D a permis de résoudre des problèmes d'étanchéité en gaz ainsi que de diminuer la surface non sensible.

Afin de mener une acquisition, il est impératif de savoir quelles données enregister. C'est pour cela que l'on utilise un système de déclenchement. Il a pour rôle de signaler quand un muon traverse le système afin que les signaux sur les détecteurs soient lus et enregistrés. Il est commun d'utiliser un système externe comme une paire de scintillateurs en coïncidence mais cela ajoute de la complexité au système. Pour le garder le plus simple possible, il est préférable d'avoir un système de déclenchement utilisant les signaux des détecteurs eux-mêmes : un auto-déclenchement. L'électronique utilisée pendant cette thèse à cette capacité. En effet, la puce de lecture DREAM peut générer un signal de coup si l'amplitude passe un certain seuil simultanément sur plusieurs canaux. La carte frontale FEU est alors capable de combiner ces signaux pour déclencher une lecture d'évènement ou, si plusieurs FEU sont utilisées en parallèle, de passer ces signaux à la carte de synchronisation TCM qui va à son tour pouvoir les traiter et, le cas échéant, générer un signal de déclenchement. Le réglage de cette logique se fait avec des seuils résumés Tableau III.2 et dont l'ajustement permet un compromis entre la pureté (lié au taux de faux-positif) et l'efficacité (lié au taux de faux-négatif) du déclenchement. Toujours dans une optique de construire un système d'acquisition simple, compact et peu consommateur d'énergie, une carte de contrôle d'alimentation haute tension a été développée. Elle permet le contrôle et la surveillance d'au plus 5 modules haute tension miniatures. Les capacités de cette carte ont permis l'étude des effets environnementaux sur la stabilité du fonctionnement des détecteurs Micromégas. En effet, dans le but de pouvoir faire des muographies en pleine nature, il est impératif que le système fonctionne de manière stable malgré les variations de temperature et de pression qu'il pourra subir. La cause de ces variations provient du phénomène d'avalanche : le gain dépend du libre parcours moyen des électrons entre deux ionisations qui dépend lui-même de la densité du gaz. Or, selon la loi des gaz parfait, cette densité est proportionnelle à P/T. En paramétrant le gain en fonction de la densité du gaz et du champ électrique on peut donc calculer ses variations en fonction de la température et de la pression. Mais il est également possible de calculer les variations de l'intensité du champ électrique qu'il faut appliquer suivant T et P pour conserver un gain constant. Par exemple, pour un mélange d'argon et d'isobutane à $5\,\%$, la variation de la tension appliquée à l'espace d'amplification de $128\,\mu\mathrm{m}$ du MultiGen 2D est d'environ $0.67\,\mathrm{VK}^{-1}$. Il a donc été possible, grâce à des sondes, de mesurer les paramètres thermodynamiques du gaz et de les corréler aux variations de gain. Ceci a permis par la suite d'implémenter une correction linéaire de la tension vis à vis des écarts de température et de pression afin de stabiliser le gain. Bien que cette méthode soit efficace, les effets non-linéaires ne sont pas négligeables pour des variations de température que l'on peut observer (de l'ordre de $30\,°\mathrm{C}$). Cependant, s'il est possible de mesurer en temps réel l'amplitude des signaux mesurés par les détecteurs, il est alors possible de faire une boucle de rétroaction ajustant la tension proportionnellement à la différence entre l'amplitude mesurée et une amplitude cible. Malgré une stabilité accrue, la résolution des MultiGen 2D reste supérieure aux attentes. Cela est dû à la dégradation de la résolution pour les traces à grand angle comme le montre la Figure III.10. Pour pallier ce problème, une méthode intéressante est de coupler le démultiplexage, la mise en cluster et la reconstruction des traces. En effet, s'il est possible d'obtenir une approximation de l'angle de la trace, alors cette information peut être utilisée pour modifier les paramètres du démultiplexage et de la mise en cluster afin de mieux rendre compte des effets physiques tels que l'étalement du signal qui peut empêcher le passage au-dessus du seuil de rejet du bruit de fond. Une approche est d'utiliser la transformée de Hough pour trouver les traces potentielles avant le démultiplexage en cherchant les signaux alignés.

Tous ces développements ont permis de mener à bien des expériences du muographie en absorption et en déviation. Concernant l'absorption, le principe est simple, chaque muon a une probabilité de survie qui dépend de son énergie initiale et, à cause de la perte d'énergie, de l'opacité qu'il a traversée. L'opacité étant définie par l'integrale de la masse volumique le long de sa trajectoire. On peut donc, en connaissant le flux lorsque l'opacité est nulle, estimer une opacité grâce au flux de muon mesuré lors d'une expérience. Puisque la source de muons est étendue à tout le ciel, cela permet d'étudier des objets de grande taille tels des volcans ou des structures archéologiques. Nous avons d'abord testé l'instrument de muographie à base de Micromégas au laboratoire, en imageant des briques de plomb. En quelques jours, le déficit de muons à l'emplacement des briques devenait significatif et des cartes de flux telles que présentées Figure IV.3a permettent de distinguer leur position. Grâce à l'expérience gagnée, une nouvelle expérience plus proche des conditions réelles d'une muographie a été mise en place. Elle avait pour but d'imager le château d'eau du CEA de Saclay. Ceci permettait de faire une expérience en extérieur mais relativement proche du laboratoire pour pouvoir intervenir rapidement en cas de problème. Le château d'eau offre un potentiel de contraste suffisant pour être muographié et, à cause des variations de niveau d'eau dans sa cuve, il permet l'essai d'une muographie dynamique. L'expérience s'est déroulée de mi-mai à fin août 2015 et a été divisée en deux phases : une éloignée puis une proche, l'instrument étant déplacé de $40\,\mathrm{m}$ de la base du chateau d'eau à $32\,\mathrm{m}$ afin de profiter du flux de muons plus élevé lorsque l'on se rapproche de la verticale. Le cycle jour-nuit à fait subir de grandes variations de température à l'instrument (de $12\,^{\circ}\mathrm{C}$ à $43\,^{\circ}\mathrm{C}$) ce qui a induit des problèmes de stabilité comme expliqué précédemment. En effet, avant la prise en compte de l'effet de la température, le jour, l'amplitude des signaux baissait sous le seuil de déclenchement et la nuit, ces amplitudes grandissaient au point de saturer l'électronique de lecture. Cependant, grâce aux corrections implémentées, il a été possible de stabiliser le système. Cela a permis de créer des muographies dans lesquelles on voit apparaître la plupart des structures en béton du château d'eau comme il est possible de le constater Figure IV.7. Pendant la prise de données, la cuve a été vidangée plusieurs fois. Il a donc été possible d'essayer de déterminer le moment de ces vidanges uniquement grâce aux muons. Après comparaison avec les données de la sonde présente dans la cuve, une très claire anti-corrélation a été observée entre le niveau de l'eau et le ratio entre le flux de muons passant à travers la cuve et le flux de ceux passant autour. Fort de cette première expérience en extérieur, il a été possible de participer à la mission ScanPyramids. Son but est d'utiliser les technologies les plus innovantes pour sonder l'intérieur des pyramides d'Égypte et en particulier celle de Khéops sur le plateau de Gizeh. Le rejet de gaz pouvant être dangereux pour les touristes visitant l'intérieur de la pyramide, il a été décidé que nos télescopes devraient être installés en extérieur, à proximité de la pyramide. Compte tenu des zones de la pyramide qu'il serait intéressant d'investiguer et cette contrainte, le placement optimal des instruments a été calculé pour sonder l'arrête Nord-Est de la pyramide. La température pouvant atteindre les $50\,^{\circ}\mathrm{C}$, les différentes parties de l'instrument ont été testées dans un four afin de vérifier leur fonctionnement et leur stabilité sous ces conditions extrêmes. Seul un courant de fuite dans le détecteur a été observé mais celui-ci ne perturbe pas son efficacité. Après une période de construction de 6 mois, les 3 télescopes à muon baptisés Alhazen, Alvarez et Brahic ont été installés sur le site de Gizeh. Après trois mois de prise de données et l'épuisement du gaz alimentant les détecteurs, environ 25 millions de muons ont été collectés sur l'ensemble des télescopes. A cause du fort contraste entre le flux à ciel ouvert et celui passant par la pyramide, il n'est pas possible de déceler des cavités d'une dizaine de mètres cubes avec la carte du flux brut. Par contre, puisqu'une éventuelle cavité va produire un gradient anormal dans le flux il est possible de raisonner sur ce gradient. Il est calculé grâce à des méthodes héritées de la vision par ordinateur tel que le filtre de Sobel. Cela permet en particulier de placer précisément le sommet et l'arrête de la pyramide et donc de replacer ce que l'on observe avec la muographie dans l'espace. Cependant, cette méthode, même généralisée au gradient de second ordre, ne permet pas de conclure sur l'existence de cavités le long de l'arête Nord-Est. Pour cela, il faut découper la muographie en tranches d'épaisseur constante faites parallèlement à l'axe de l'arête. Avec cette méthode, il est facile de déceler des excès de muons liés à la présence de cavités puisque ces tranches correspondent à des zones d'opacité quasi-constantes. Deux cavités ont été décelées : une déjà connue (la chambre derrière l'encoche) avec un excès de 144.6 muons (6.4σ) et une inconnue jusqu'alors avec un excès de 129.1 muons (5.7σ).

Concernant la muographie par déviation, sa force provient du fait que l'on peut situer la déviation du muon et donc obtenir une information tridimensionnelle. En effet, lorsque le muon traverse de la matière, il subit les champs électriques nucléaires et peut donc être dévié. La moyenne de l'angle de déviation est nulle mais son écart-type est relié au numéro atomique du matériau traversé. En mesurant la trajectoire du muon avant et après qu'il traverse l'objet à étudier, il est donc possible de mesurer l'angle de déviation ainsi que le lieu de sa déviation. C'est le principe de la méthode dite du PoCA (Point of Closest Approach) qui situe le lieu de la déviation à l'intersection des deux demi-trajectoires. En revanche, cette méthode fait la lourde hypothèse qu'il ne s'est produit qu'une seule déviation significative. D'autres méthodes plus complexes se basent sur le PoCA pour reconstruire l'ecart-type de la déviation associée à chaque zone de l'espace comme le fait la méthode ML-EM (maximisation d'espérance par maximisation de vraisemblance) élaborée par Schultz. Un premier instrument nommé TomoMu a été développé pour tester ces méthodes. Il est très similaire aux télescopes utilisés en muographie par absorption mais un espace est aménagé entre les deux doublets de détecteurs pour pouvoir y placer des objets à imager et la distance entre les détecteurs d'un même doublet est augmentée pour optimiser la résolution angulaire de chaque demi-trajectoire. Celle-ci est en effet cruciale pour mesurer de faibles déviations. En plaçant une pince, une pierre calcaire et une brique de plomb sur une planche de bois dans l'instrument, il est possible après une journée de prise de données de distinguer tous ces objetsen utilisant seulement la méthode basique du PoCA, en particulier la planche de bois comme le montre la figure Figure V.4a. Ce dispositif a également permis de tester en conditions réelles l'algorithme ML-EM qui permet notamment de supprimer les effets d'acceptance sur l'image finale. Dans le cadre du programme NRBC-E (menaces chimiques, biologiques, radiologiques et nucléaires), un bien plus imposant instrument a été développé. Son but est de pouvoir détecter des matériaux à fort numéro atomique (comme l'Uranium) dans des conteneurs en un temps réduit. L'application visée étant le contrôle aux frontières dans les ports qui est contraint par le DNDO (l'organisme américain pour la détection de matière nucléaire) : une méthode ne peut être retenue que si elle est capable de détecter $4\,\mathrm{kg}$ d'Uranium en moins de $2\,\mathrm{min}$. Un portique de $4\,\mathrm{m}$ de haut a donc été construit avec deux plans de détection en hauteur pour mesurer la trajectoire incidente et deux plans de détection sous l'emplacement du conteneur pour mesurer la trajectoire sortante. Chacun des plans comporte 4 MultiGens et présente donc une surface active totale de $1\,\mathrm{m}^2$. A cause du flux limité de muons et la contrainte temporelle forte du DNDO, il n'est pas possible de faire de l'imagerie pour détecter l'Uranium et sa position. En revanche, il est possible de détecter une anomalie dans la distribution de l'angle de déviation des muons en la comparant à un cas connu. Grâce au test de Kolmogorov-Smirnov, il est possible de comparer une distribution test avec une distribution de référence et de mettre à jour le résultat de ce test en temps réel. Cela nous permet d’obtenir l’évolution de la probabilité de compatibilité au cours de la prise de donnée. Si cette probabilité chute sous un certain seuil, alors un signal d’alerte peut être émis pour une acquisition plus longue permettant de faire l’imagerie complète du conteneur. En comparant des données obtenues avec un conteneur rempli de ballots de sciure et avec un conteneur contenant des barreaux d’Uranium appauvri entre les ballots de sciure, il a été prouvé que les contraintes du DNDO peuvent être respectés avec un instrument plus grand que le prototype utilisé.

Introduction

Imaging techniques are in a constant evolution in order to improve the understanding of our world. The use of artificial radiations to enhance these techniques is common. However, such radiations are often harmful, expensive and complex to implement because of safety measures or the high technical level they need to be produced. On another hand, natural radiations are free to use, often harmless so they offer an interesting alternative. Considering the showers of particles they induce when they hit the atmosphere, the cosmic rays are a constant source of radiation. The muon is one of them which can reach the ground. The muography technique was first tested by E.P. George in 1955 to measure the density of rocks over a tunnel but the first image was made by Luis W. Alvarez in 1967. He already made use of gaseous detectors, spark chambers, in order to scan the Khafre's pyramid in Giza, Egypt. Even if he did not discover unknown voids, he was able to put constraints on the size of potential cavities. Moreover, it initiated a new imaging technique that could be used in the future. Geologists and volcanologists were the firsts to reuse this method in order to study the internal structure of volcanoes. This application was initiated by Nagamine *et al.* [1] and then largely spread over the world, in particular among Italians of INFN and INGV, and French of CNRS and IPGP. Robust detectors like scintillators or nuclear emulsions were used as they are well adapted to data taking campaigns in the wild. However, thanks to the recent improvements on MPGD, particularly within the CERN R&D51 collaboration, such detectors can now compete with them.

Among MPGDs, the Micromegas is the result of a long and active development of gaseous detectors. It was designed and improved to fulfill the needs of particle and nuclear physics experiments. Recent progress made them very robust and they can now be made in the industry. Moreover, thanks to multiplexing techniques, they can reach a fine position resolution with their high granularity without requiring too much of electronics channels. Therefore, these improvements made the Micromegas detectors ready to be deployed cheaply in the field to do muon tomography measurements.

In the first part of this thesis, the origin and the characteristics of the cosmic muons created by primary cosmic rays interacting with the atmosphere are presented. To emphasize the imaging capabilities of muons, their interactions with matter are also exposed.

Afterwards, the history of the gaseous detectors is shown to explain the Micromegas working principles along with the latest developments that have been made. Such evolutions enable this detector to go out of laboratories and to be operated outside, in order to be part of muon tomography imaging apparatus.

In the third part, special developments in the field of electronics, detector design and operation are reported. These progresses ensure the stable operation of a Micromegas-based imaging system in the wild, without access to power and enduring strong environmental condition variations.

The fourth part focuses on the work done in the field of absorption (or transmission) muography starting from the first laboratory tests, continuing with the water tower experiment and the ScanPyramids data taking campaign.

The last part is dedicated to the muon scattering tomography technique. The challenges of the data inversion problem is presented together with simulated and experimental data. Such data were taken using a portable scale device called TomoMu and a large scale imager whose aim is to detect high Z material inside containers.

Chapter I

Cosmic Muons

After a short introduction on the history of the discovery of cosmic rays, their origin is discussed. The interactions of the primary cosmic rays inducing the production of muons are then presented to explain the cosmic muon flux characteristics at ground level. The interactions of muons through matter are described to show the imaging potential of such particles.

I.A Origin

I.A.1 Primary cosmic rays

I.A.1.a History

In the early times of the XX$^{\text{th}}$ century, the cause of the observed air ionization was not known. The common belief since the discovery of radioactivity in 1896 by Becquerel and Curie was that it comes from earth radioactivity and the volatile radioactive elements released by rocks. However, several electroscope experiments conducted firstly on high monuments by Wulf and below the sea by Pacini showed hints that the amount of radiation is not changing at the expected rate with respect to the altitude if it would come from the Earth. This trend was confirmed by Hess in 1912 who did several balloon experiments [2]. He measured the amount of radiation at different altitudes from the ground up to $5300\,\mathrm{m}$ high. However, he did not measure any significant flux change up to $2000\,\mathrm{m}$ high and then observed a dramatic increase of it. He concluded that the radiation has to come from the outer space like from the Sun. To test this last hypothesis, one of the balloon experiment took place during a solar eclipse. No significant variation was measured between the measure before and during the eclipse so the solar origin was ruled out. His work was awarded by a Nobel Prize in 1936.

Even if the cosmic origin was demonstrated, the composition of the incoming radiation was still unknown. In the 1920s and 1930s, several physicists, such as Jacob and Compton, measured the variations of the cosmic flux with latitude, emphasizing the interaction between this radiation and the Earth magnetic field, hence ruling out neutral particles. Again in the 1930s, experiments made by Alvarez, Johnson and Rossi showed an excess of radiation coming from the West with respect to the East. Taking into account the geomagnetic field, this showed that the primary cosmic rays are mostly positively charged.

I.A.1.b Origin and composition

Now, it is known that primary cosmic rays are made of atomic nuclei, mostly protons and α particles. The flux of each element is shown in Figure I.1.

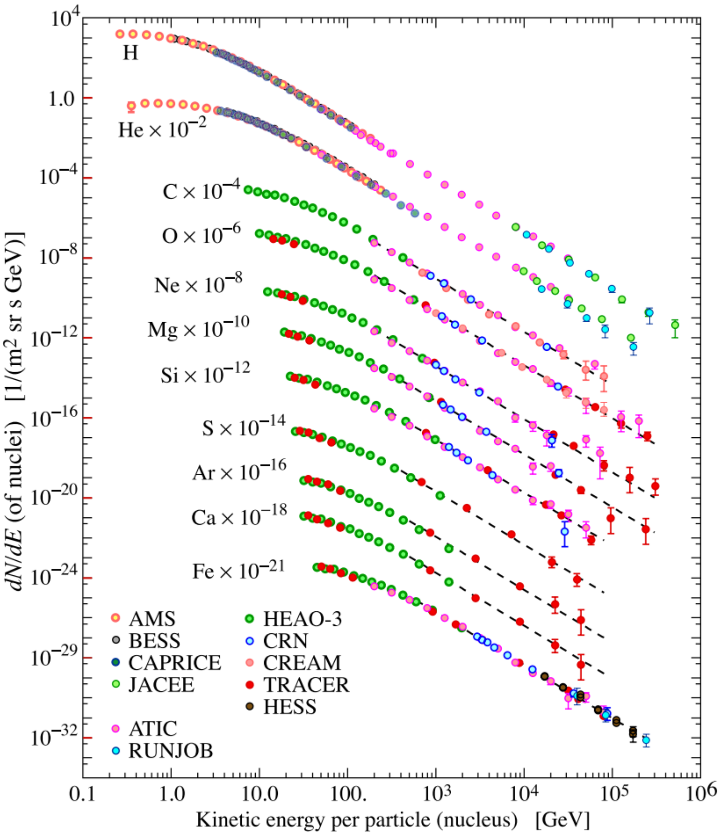

FIGURE I.1 – Flux of the primary cosmic rays with respect to the energy for each component [3].

These primary cosmic rays mainly come from extra solar system sources. These astrophysical sources produce and accelerate these particles which will then travel for a long time ($\sim 1{\times}10^6$ y), interacting with the interstellar medium *i.e.* being deflected and changing composition. After all these transformations, they will eventually reach the solar system and our planet. The solar magnetic field is inducing a primary cutoff of the particles that can reach the Earth. Aside from the magnetic field strength, the path followed by a particle depends on its intrinsic characteristics: its momentum and charge. The rigidity R can then be defined as:

$$R = \frac{pc}{qe} \tag{I.1}$$

Here p is the particle momentum, c is the speed of light, q the particle charge number ($q = Z$ in case of nuclei), and e is the electron charge. The rigidity is defined such as all the particles having the same rigidity follow the same path under the influence of a magnetic field. This way, the cutoff induced by the solar magnetic field is a rigidity cutoff. Indeed, if a particle rigidity is below a critical one $R < R_{c,sun}$, it will be deflected away from the sun. Since this solar field is not constant, the critical rigidity $R_{c,sun}$ is time dependent. So, it depends on the 11 y long solar activity cycle and increases dramatically during coronal mass ejection. This last phenomenon is known as the Forbush decrease [4]. This cutoff also depends on the primary cosmic ray direction. Considering all these effects, it affects primary cosmic ray flux of particles below approximately $10\,\mathrm{GeV}$.

The Earth magnetic field is also influencing the primary cosmic ray distributions. As exposed in section I.A.1.a, the geomagnetic effects are known since the 1920s. As for the sun magnetic field it applies a rigidity cutoff $R_{c,earth}$ depending on the direction and time. The geomagnetic field intensity depends on the geomagnetic latitude[1]: it is fainter near the poles and stronger in the equator. This way, the primary cosmic flux increases with the geomagnetic latitude. Moreover, since the primary cosmic rays are mostly composed of positively charged particles and the Earth magnetic field is a dipole, cosmic rays coming from the East are deflected toward the Earth and the ones coming from the West are deflected away. It creates an asymmetry known as the East-West effect. To summarize this and as presented in [5], for each Earth location and altitude different direction cones can be defined: a first cone corresponding to the allowed directions for every rigidity and a second one corresponding to the direction from which no cosmic rays of any rigidity can come from. Between these two cones is a region in which for each direction there is a different rigidity cutoff which is the Störmer cutoff.

I.A.2 Atmospheric interactions

If a cosmic ray reaches the Earth, it will interact with its atmosphere. Nucleus-nucleus (or proton-nucleus) collisions will happen, inducing a cascade of reactions. These reactions will mainly create pions and kaons. The charge asymmetry of these secondary particles reflects the charge asymmetry of the primary cosmic rays. Since these particles are unstable they will decay according to their lifetimes indicated in Table I.1.

Mesons	**Lifetimes** [s]
π^+, π^-	2.6×10^{-8}
π^0	8×10^{-17}
K^+, K^-	1.2×10^{-8}
K^0_S	9×10^{-11}
K^0_L	5.1×10^{-8}

TABLE I.1 – Meson lifetimes.

The kaons have several decay channels, the hadronic ones involving pions, the semi leptonic ones involving a pion, a charged lepton and a neutrino and finally the leptonic ones involving a charged lepton and a neutrino. The neutral pion will decay in γ pairs which will start an electromagnetic shower by pair creation and Bremsstrahlung. The charged pions will mostly decay in a charged lepton with the associated neutrino following the process shown in Figure I.2.

---

[1] The geomagnetic latitude based on the Earth magnetic field axis has to be distinguished from the geographic latitude based on the Earth rotation axis.

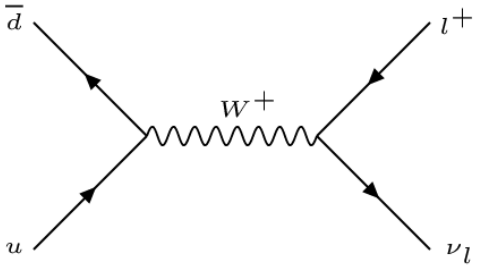

FIGURE I.2 – First order Feynman diagram of π^+ decay.

This way it can produce electrons or muons and the ratio of branching ratios between the two can be computed as:

$$R_{e/\mu} = \frac{m_e^2(m_\pi^2 - m_e^2)^2}{m_\mu^2(m_\pi^2 - m_\mu^2)^2} = 1.283\times10^{-4} \tag{I.2}$$

Where m_e, m_μ and m_π are respectively the masses of the electron, muon and pion. It shows that the muon decay channel is largely favored. This effect can be explained by the helicity suppression. Indeed, only chiral left particles can weakly interact.

At the sea level, the cosmic shower is composed of four parts. The first one is the hadronic part composed of baryons coming from the collisions and the not yet decayed secondary mesons. The second one is the neutrino part since a neutrino is created along each lepton. This component will almost not interact with the Earth matter anymore. The third one is the electromagnetic component initiated by neutral pions and composed of electrons, positron and gamma rays. The last part is the muon (and anti-muon) one which allows us to make muon tomography. Even if there are a lot more electrons and gamma rays than muons that are created, the first ones are losing more energy traveling down the atmosphere. This way, at the ground level, there are more muons than electrons and gamma rays. A simulated cosmic ray shower is shown in Figure I.3.

I.B Characteristics

I.B.1 Zenith angle and energy distributions

According to the primary cosmic rays angular and energy spectra and knowing the processes inducing the creation of muons, the muon flux can be deduced. Indeed, the interaction of primary cosmic rays with the upper atmosphere creates mesons that decay into muons. However, mesons can also interact with the upper atmosphere, inducing another reaction cascade. Since the interaction probability increases with the energy and the atmosphere density which decreases with the altitude, the ratio of mesons interacting with respect to the ones decaying is lower for horizontally propagating mesons than for downward propagating ones. This way, at high energy, the descending mesons will further interact and produce lower energy particles while the nearly horizontally going mesons will decay into high energy muons before losing energy. This first phenomenon explains some flux dependencies with respect to the muon energy and its zenith angle. Following this, Gaisser built a model [7] neglecting

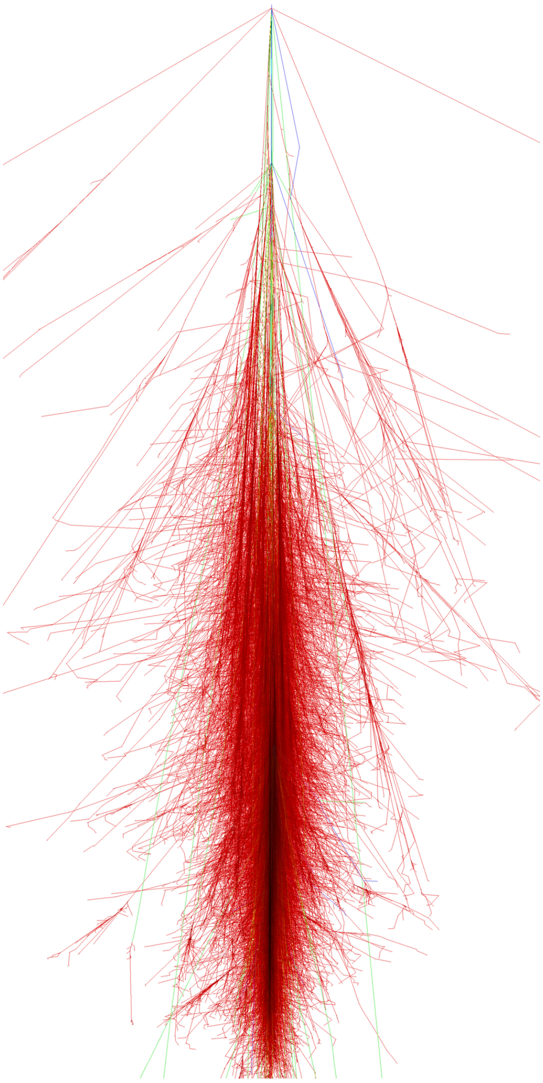

FIGURE I.3 – Cosmic shower induced by a primary $1\,\mathrm{TeV}$ proton showing the hadrons (blue), muons (grey), electrons (red) and neutrinos (green) simulated with CORSIKA [6].

the muon decay, its energy loss and the Earth curvature, estimating the total (positive and negative) muon flux with respect to their energy E and zenith angle θ:

$$\frac{\mathrm{d}\phi}{\mathrm{d}E} = \mathrm{d}\phi_0 \left(\frac{E}{E_0}\right)^{-2.7} \left(\frac{1}{1 + \dfrac{E\cos(\theta)}{E_{0,\pi}}} + \frac{r_{\pi/K}}{1 + \dfrac{E\cos(\theta)}{E_{0,K}}} \right) \tag{I.3}$$

$$\mathrm{d}\phi_0 = 0.14\,\mathrm{cm}^{-2}\mathrm{s}^{-1}\mathrm{sr}^{-1}\mathrm{GeV}^{-1} \qquad r_{\pi/K} = 0.054 \qquad E_0 = 1\,\mathrm{GeV}$$

$$E_{0,\pi} = 104.5\,\mathrm{GeV} \qquad E_{0,K} = 772.7\,\mathrm{GeV}$$

The two fractions correspond to the respective contributions of pions and kaons. However, since this model neglects the muon decay rate and the energy loss while traveling through the atmosphere to reach the ground, this expression is accurate only for muons having a sufficient energy: $E > \frac{100\,\mathrm{GeV}}{\cos(\theta)}$. Moreover, because of the flat Earth approximation, it is only valid for a certain range of zenith angle: $\theta \lesssim 70°$. However, for the majority of muon tomography experiments, the contribution from low energy muons is not negligible. Therefore, another parametrization has to be used for low energy. Indeed, the atmosphere thickness crossed by the incoming muon increases with the zenith angle, increasing the energy loss and decreasing the surviving factor. According to the recorded data so far, a fitted parametrization of the flux with respect to the muon momentum p and zenith angle θ [8] can be used outside of the Equation I.3 validity range:

$$\frac{\mathrm{d}\phi}{\mathrm{d}p} = \frac{\phi_0}{p\cos(\theta) + p_A}(p + p_B sec(\theta))^{-2.7}\frac{p + p_C}{p + p_C\sec(\theta)} \tag{I.4}$$

$$\phi_0 = 18\,\mathrm{m}^{-2}\mathrm{s}^{-1}\mathrm{sr}^{-1} \qquad p_A = 145\,\mathrm{GeV/c}$$

$$p_B = 2.7\,\mathrm{GeV/c} \qquad p_C = 5\,\mathrm{GeV/c}$$

These parametrizations can be used to describe the observed muon spectra shown in Figure I.4. Another widely used zenith angle dependent description consists in writing the muon flux as:

$$\phi(E,\theta) = \phi_\perp(E)\cos^{n(E)}(\theta) \tag{I.5}$$

Where $\phi_\perp(E)$ is the vertical flux of muons having an energy E and $n(E)$ is an energy dependent exponent with:

$$\lim_{E\to\infty} n(E) = -1 \tag{I.6}$$

$$\lim_{E\to 0} n(E) = 2 \tag{I.7}$$

Some meaningful values can be extracted from the cosmic muon observation: the mean muon energy is $\bar{E} \sim 4\,\mathrm{GeV}$, the muon flux integrated over the full energy range is $\phi(\theta) \sim \phi_\perp \cos^2(\theta)$ which corresponds to the zenith angle distribution of $\sim 3\,\mathrm{GeV}$ muons with $\phi_\perp = 70\,\mathrm{m}^{-2}\mathrm{s}^{-1}\mathrm{sr}^{-1}$.

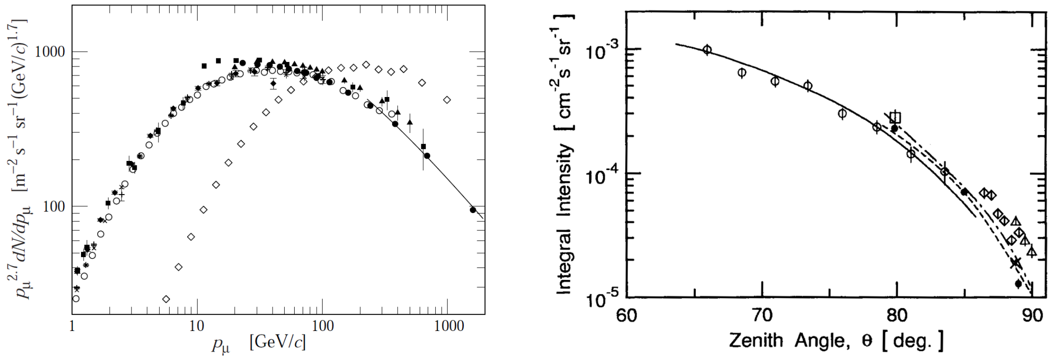

(a) Muon energy spectrum measured at sea level for $\theta = 0°$ except for ◊ data taken at $\theta = 75°$ [3].

(b) Muon zenith angle spectrum measured at sea level integrated over the full energy range [7].

FIGURE I.4 – Muon energy and zenith angle spectra measured at sea level.

These models do not take into account any azimuth angle φ dependence. However, since the East coming flux of the primary cosmic rays is smaller than the West one, the muon flux will have a sinusoid dependence on the azimuth angle: $\phi(E,\theta,\varphi) \sim \phi(E,\theta)(1+\frac{\delta\phi}{2}\cos(\varphi-\varphi_{West}))$ where $\delta\phi$ is the difference between the West and the East flux and φ_{West} corresponds to the West azimuth direction.

I.B.2 Location and time dependencies

As for the energy and zenith angle spectra, the time and location dependencies of the muon flux partly come from the primary cosmic ray dependencies. Concerning the location dependencies: because of the geomagnetic field, the flux of primary cosmic rays reaching the atmosphere is increasing with the latitude so the muon flux is higher near the geomagnetic poles. Concerning the time dependencies: because of the time fluctuations of the sun magnetic field, the primary cosmic rays rigidity cutoff is time dependent. It will induce a timing variation on the flux of primary cosmic rays which reach the Earth and, therefore, a variation of the muon flux. The remaining dependencies arise from the propagation of the muons through the atmosphere. Indeed, the crossed atmosphere thickness depends on its density which depends on the temperature and pressure conditions. This thickness variation is inducing energy loss fluctuations as described in section I.C.1, it shifts the energy spectrum and causes an absorption of the lesser energetic muons. Since these conditions are location and time dependent, so is the muon flux. Therefore, the flux is correlated with the temperature and anti-correlated with the pressure as shown in Figure I.5. The measurement was made with the bench described in section IV.B. Concerning the temperature effect, a first contribution is from the day to night oscillation and a second coming from the seasonal variations of the upper atmosphere as measured by [9] which affect the ratio between the pion and kaon contributions.

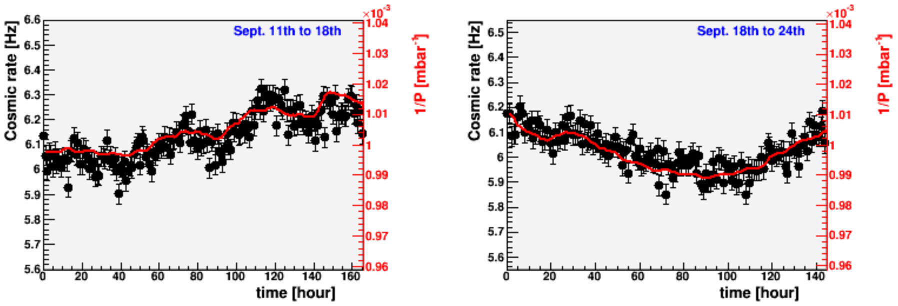

FIGURE I.5 – Measure of the cosmic muon rate compared with the atmospheric pressure variations.

I.C Interaction with matter

As they travel through matter, muons like any other particle can interact with its surrounding environment. These interactions are caused by multiple processes and lead to two major effects:

- decrease of their energy
- change in the direction of propagation

I.C.1 Energy loss

Several processes can lead to a loss of energy by traveling inside matter such as collisions with the atoms of the medium. The impact will lead to some energy transfer between the muon and the matter. This energy can take different forms: recoil energy, atomic and molecular excitations or ionization of the medium. In the case of ionization, the energy is then transferred to the knocked out electron. At high energy, the contribution of radiative processes will become dominant. The main radiative process at cosmic muon energies is the Bremsstrahlung. For cosmic muon energies, the stopping power per unit length $-\frac{\mathrm{d}E}{\mathrm{d}s}$ can be modeled by the following:

$$-\frac{\mathrm{d}E}{\mathrm{d}s} = \rho(B + RE) \tag{I.8}$$

Where E is the muon energy, ρ is the mass density, R is a constant characterizing the radiation process contribution and B is the ionization mass stopping power modeled by the Bethe equation [10]:

$$B = \frac{N_A e^4}{4\pi\epsilon_0^2 m_e c^2} q^2 \frac{Z}{A}\frac{1}{\beta^2}\left(\frac{1}{2}\ln\frac{2m_e c^2\beta^2\gamma^2 W_{max}}{I^2} - \beta^2 - \frac{\delta}{2}\right) \tag{I.9}$$

This formula takes into account the muon characteristics: its charge $q = \pm 1$, its kinetics (β and γ)[1] and the maximum energy transfer per collision W_{max} which depends on the muon energy. It takes also into account the medium properties: its atomic Z and mass A numbers and the mean excitation energy I. The δ term represents a density effect correction which is energy dependent. As an example, the energy loss of a muon traveling through Copper is shown in Figure I.6.

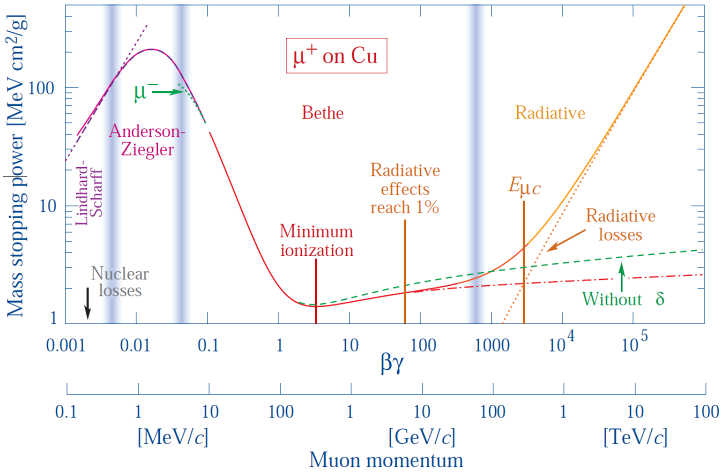

FIGURE I.6 – Muon energy loss in Copper with respect to its energy [3, 11].

The stopping power described here is a mean stopping power because the processes of energy transfer are stochastic.

---

[1] β is the muon velocity expressed in term of a fraction of the light celerity and $\gamma = (1-\beta^2)^{-1/2}$ is the Lorentz factor.

The critical energy E_c above which the radiative processes become dominant can be defined. At first order this energy is $E_c = B/R$.[1] Considering the material crossed, the critical energy is of the order of several hundreds of GeV. As described in section I.B.1 and considering the range of critical energies shown in Figure I.7, the fraction of cosmic ray muons above the critical energy is negligible, so the radiative effects are not taken into account in this work.[2]

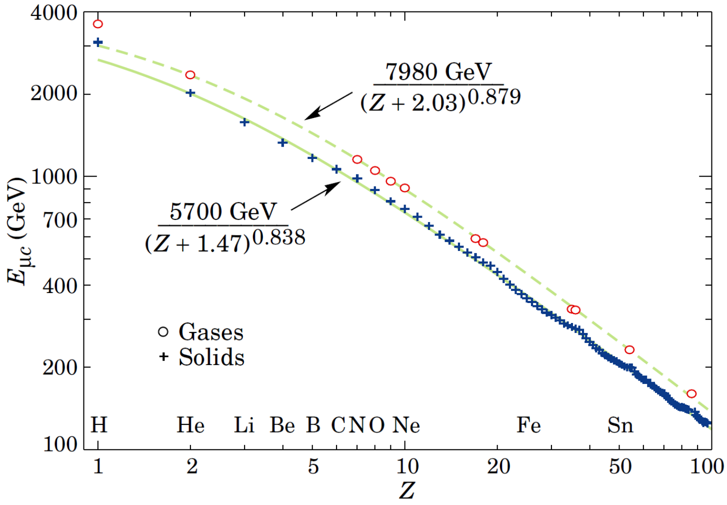

FIGURE I.7 – Critical energy E_c for muons with respect to the composition of the crossed material [3, 11].

Losing energy while passing through matter, the muon Lorentz factor decreases so the time dilatation effect decreases. This way, the muon will eventually decay inside matter.

I.C.2 Multiple scattering

The passage through matter does not lead only to some energy loss. Another important effect is the scattering. Indeed, matter is a charged medium as it is mostly composed of charged particles, so muons can interact with the nuclei and electronic electric fields. Even if the average muon path is straight, Molière's theory allows us to link the standard deviation of the scattering angle ϑ to the muon energy, and its path length s compared to the radiation length X_0 of the scattering medium [12]:

$$\sigma_\vartheta = \frac{E_s}{\beta pc}\sqrt{\frac{s}{X_0}}\left(1 + 0.038\ln\left(\frac{s}{X_0}\right)\right) \tag{I.10}$$

Where E_s is a constant. If ϑ is a projected angle then $E_{s,plane} = 13.6\,\mathrm{MeV}$, if ϑ is the scattering angle in 3D space then $E_{s,space} = \sqrt{2}E_{s,plane} = 19.2\,\mathrm{MeV}$ and p is the muon momentum. The radiation length X_0 is the length scale on which particles lose energy

---

[1] If B and R are considered as constant, the Bethe contribution B equal the radiative contribution RE at $E = B/R$

[2] Indeed, no studied object had sufficient opacity to make this fraction significant.

through radiative processes.

$$X_0 = \frac{\bar{X}_0 A}{\rho Z(Z+1)\ln\left(\frac{287}{\sqrt{Z}}\right)} \tag{I.11}$$

Where $\bar{X}_0 = 716.4\,\mathrm{gcm}^{-2}$ and ρ is the mass density of the crossed material.

Chapter II

The Micromegas Detector

After drawing a brief picture of the history of gaseous detectors, this chapter reviews the working principles of the Micromegas detector. The latest developments which aim to further improve this detector are also presented together with the latest electronics made to read them. Lastly, the prototype detectors designed for muon tomography are described and their performance is shown.

II.A The Micromegas: a MPGD detector

II.A.1 A brief history of gaseous detectors

The latest high energy physics experiments have been made possible by the extensive use of the electronic analysis of the data. In the early days of particle physics, the analysis was made by an optical observation of the detectors or their photographs. By increasing the number of events, this long and fastidious treatment was no longer practically possible. So the use of electronics spread together with electronically readable detectors. A large variety of detectors that do not need a visual, event by event, analysis have been developed. The interactive material which will induce a readable signal can be in a gaseous, a liquid or a solid state depending on the purpose of the detector.

The use of a gas medium to build detectors was initiated well before the rise of the electronic era. One of the first developments was made by Wilson in 1895 who started to develop the so called *cloud chamber* [13]. As all the later gaseous detectors, it uses the ionization energy loss along the path of a charged particle. In this case, ions are good seeds for droplet formation inside a saturated alcohol vapor in such a way that particle paths are shown as droplet trails as shown in Figure II.1. Thanks to this work, Wilson earned the 1927 Nobel prize and his detector had permitted a lot of discoveries such as the muon in the 1930s.

In the early XX$^{\text{th}}$ century, Hans Geiger and Walther Müller developed a new instrument that bear their name: the Geiger-Müller tube [14]. It consists of a wire anode in the center of a cylindrical cathode. The volume is filled with a gas at low pressure ($\sim 0.1\,\mathrm{bar}$) and a high voltage is applied between the two electrodes. When an ionizing particle crosses the tube, it creates electron-ion pairs. Since the field has a cylindrical symmetry, its strength varies with $1/r$ where r is the distance from the wire. This way the electron will first drift toward the wire, until the field grows enough to initiate a Townsend avalanche (Figure II.2).

FIGURE II.1 – Saclay Wilson chamber showing the disintegration of ^{220}Rn.

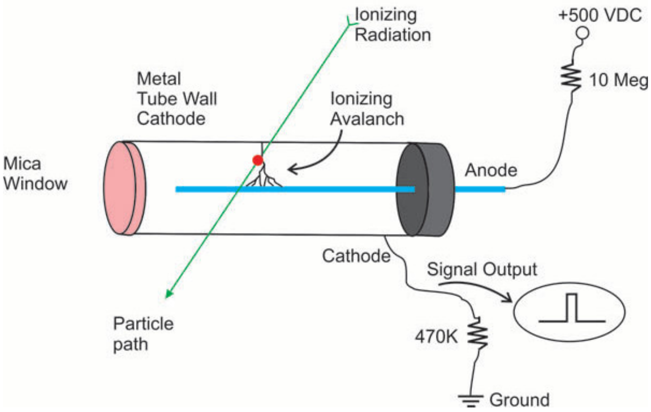

FIGURE II.2 – Sketch of Geiger-Müller tube operation.

At first, it was operated in the saturating region where the amplification induces a discharge. Emitted photons induce secondary avalanches which make the ionization grow along the whole tube and is only stopped by the ion screening effect. Indeed, while many avalanches take place near the wire, lots of electrons are created along with the same amount of slow moving ions. These positively charged particles generate a field which screen the one created by the voltage applied between the wire and the cylindrical cathode. This mode is very useful to make particle counter because the charge collected on the wire creates a voltage drop of the order of 1 V that can be measured with very simple electronics. However, a lot of ions are created and their collection is slow, so the dead time is long. With the development of electronic readout, the use of these tubes as a proportional counter progressed. Adjusting the voltage and using a quencher to absorb the emitted photons will reduce the avalanche spread and keep the signal proportional to the energy lost through ionization while reducing the dead time. As seen in Figure II.3, there are different regimes with respect to the field strength. If the field is too low (region I), the ion and electron are not separated and they recombine. Increasing the field (region II) separate them but the electrons drift without any amplification. Then the Townsend avalanche mechanism starts to occur (region III) up to the Geiger-Müller saturation regime (region IV). If the field keeps increasing, the breakdown voltage is reached and discharges happen.

The need for trackers in the 1960s increased but the development of spark chambers failed to make them capable of handling rates higher than 100 Hz. This is when

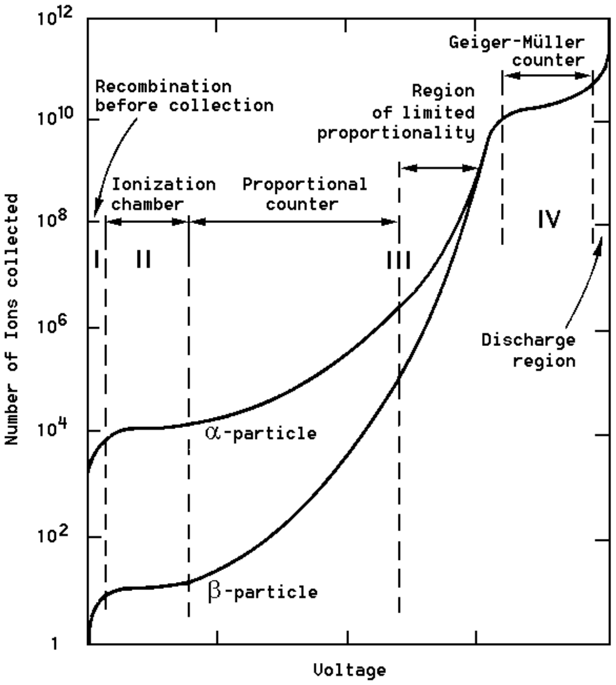

FIGURE II.3 – Operation regimes of a parallel plate gaseous detector illustrated with α and β rays.

Georges Charpak had the idea to combine multiple proportional counters in one unique multiwire proportional chamber (MWPC) [15]. This tracking detector earned him the Nobel prize in 1992. Putting multiple Geiger-Müller tubes side by side can give a position information. However, in a MWPC, the anode wires can be put closer together (down to a few millimeters) and a unique gas volume is used. The cathode is then a plane parallel to the wire plane at a few mm distance. The position resolution can be further improved by measuring the timing of the signal to deduce the distance between the particle path and the fired wire. This type of chamber is called *drift chambers* [16]. Nonetheless, to reach a great precision, wires have to be kept straight. It implies drawing high tension on a large number of very thin wires. This causes wire to break and the mechanical frame to bend under the tension. Also, the ionization can induce ageing effects of the wire: ions can form deposits on the wire surface. These drawbacks made space for more innovation toward new gaseous detectors such as the GEMs [17] and Micromegas [18].

II.A.2 Overview of Micromegas operation

In previous detectors, the ionization of the gas and the amplification stage were made inside the same volume. On the contrary, the Micromegas concept is to separate these two regions.

II.A.2.a Principle of operation

The Micromegas (**Micro**-**Me**sh **Ga**seous **S**tructure) detector is composed of two separate volumes, the first one is defined by a cathode and a metallic micro-mesh typically distant by a few millimeters and is called the drift volume. When an ionizing particle crosses this volume, it creates electron-ion pairs. Applying an electric field of the order of $10^4\,\mathrm{Vm}^{-1}$, the rapid recombination of the pairs can be avoided by separating them *i.e.* making the electrons drift toward the micro-mesh. These primary electrons are too few, they cannot induce a strong enough signal to be read by the electronics. This is the goal of the second space, the amplification volume. It is situated on the other side of the micro-mesh down to the readout anode. A much higher electric field ($\sim 4{\times}10^6\,\mathrm{Vm}^{-1}$) is established inside this volume. This field accelerates the primary electrons so that they have enough energy to ionize the gas on their own. This acceleration occurs also to the secondary electrons in such a way that an electron cascade will develop. The principle described here is illustrated in Figure II.4 showing the two gas volumes and the ionization and amplification processes. As described by the Shockley-Ramo theorem [19, 20], all these moving charges (electrons and ions) induce a signal on the readout pattern. According to this theorem, each charge q moving at a speed v will induce a charge Q:

$$Q = \int Eqv\,\mathrm{d}t \tag{II.1}$$

Considering the field E constant, Q will mostly depend on the distance traveled by each charge $\int v\,\mathrm{d}t$. Since most of the ionizations happen near the anode plane, the electrons will produce a prompt signal and the ions a longer tail which represent $\sim 80\%$ of the total signal as seen in Figure II.5.

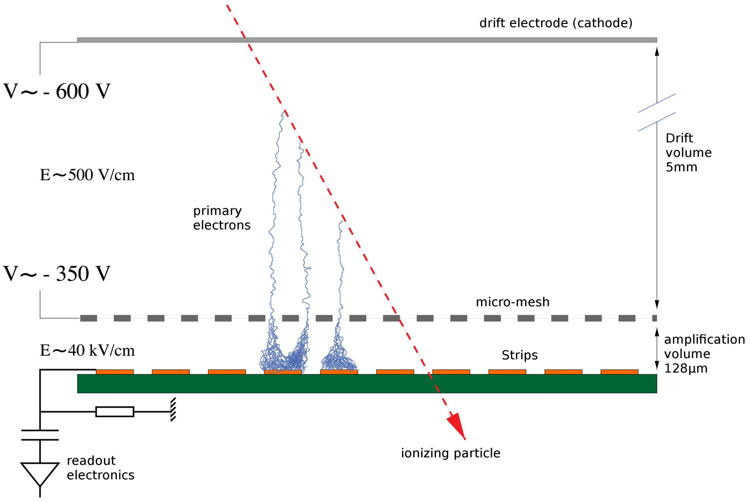

FIGURE II.4 – Sketch of a typical Micromegas detector.

The slowness of these ions can induce some dead time if another event occurs before they are collected. To maintain a small dead time (which means high-rate capability) and good time resolution, these ions have to be collected relatively fast. Since they are collected by the micro-mesh, this is why the distance between the anode and the micro-mesh is kept small, typically $100\,\mu\mathrm{m}$. The signal induced by the whole cascade is now high enough to be readable by a charge amplifier electronics.

Even if the micro-mesh is designed to let the electrons pass through it, some will be collected by the mesh wires. The opposite phenomenon occurs for ions: most of them will be collected but some can pass through it. To quantify these phenomena, the electron (resp. the ion) transparency R_e (resp. R_i) is defined as the probability for an electron (resp. an ion) to go through the mesh. They mainly depend on the ratio of the amplification field over the drift field E_a/E_d. As explained in [18], the electron

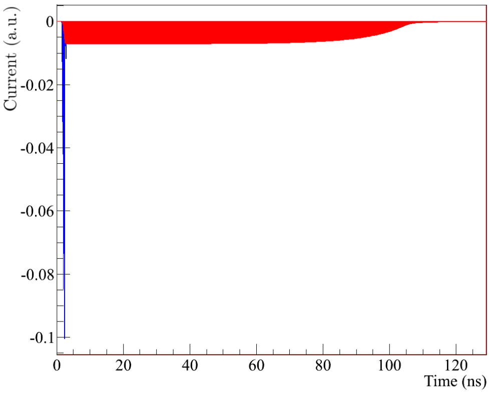

FIGURE II.5 – Typical signal induced by electrons (blue) and ions (red) in a Micromegas detector.

transparency is increasing with this ratio up to a plateau of maximum transparency close to $100\,\%$. The ions are subject to the opposite effect: at low field ratio the probability to go inside the drift region is high while it tends small values ($< 1\,\%$) as the field ratio increases. During typical operation, the field ratio is set to be in the electron transparency plateau region.

By segmenting the anode into strips or pads, the position of the primary ionizing particle which crossed the detector can be inferred. The strength of the collected signal depends on two main factors: the number of primary electrons and the gain of the amplification. To be efficient, the signal has to be above the noise level and below the saturation of the readout electronics so the gain must remain relatively constant in time and through the detector surface. However, the gain depends on the gas characteristics and on the electric field.

II.A.2.b The Townsend avalanche mechanism

When an electron is accelerated inside the gas, it can acquire sufficient energy to ionize another atom. Let λ be the mean free path for ionization: it is the mean distance between two collisions leading to ionization. Some collisions will induce an ionization and others only an excitation of the atom. So the ratio between the energy loss per unit length and the ionizations per unit length w_i (ionization potential) is higher than the minimum energy needed to knock out an electron E_i. The number of electron-ion pairs produced by unit length is: $\alpha_T = 1/\lambda$ where α_T is the first Townsend coefficient. The increase of electron number $\mathrm{d}n_e$ inside a slice $\mathrm{d}x$ can then be expressed as:

$$\mathrm{d}n_e = \alpha_T n_e \,\mathrm{d}x \tag{II.2}$$

So the number of electrons n_f reaching the anode depends on the distance between the two electrodes d and the number of electrons initially near the cathode n_i as follow:

$$n_f = n_i \exp\left(\int_0^d \alpha_T \,\mathrm{d}x\right) \tag{II.3}$$

Considering the first Townsend coefficient constant between the two electrodes, the gain of a parallel plate detector is defined as the ratio between the final electron and the primary electron numbers:

$$G = \exp(\alpha_T d) \tag{II.4}$$

However, the Micromegas amplification space is not a perfect parallel plate device: the micro-mesh is composed of woven wires and the anode is segmented. Thus, the distance parameter d is not properly defined and the field itself is not completely uniform so this expression is only an approximation. The Townsend coefficient hinges on the gas properties, in particular on the molecular density and on the electron kinematics *i.e.* the electric field. A common parametrization of the Townsend coefficient is [21]:

$$\frac{\alpha_T}{\rho_n} = A \exp\left(\frac{-B\rho_n}{E}\right) \tag{II.5}$$

Where A and B are gas dependent coefficients, ρ_n is the molecular density and E is the electric field. Therefore, the gain of a Micromegas detector depends on the gas mixture, the thermodynamic conditions (in particular T and P) and the electric field. Moreover, the collisions and ionizations inside the gas are stochastic phenomena inducing gain fluctuations on an event by event basis. The distribution of the gain closely follows a Polya law [22].

II.A.2.c Sparking phenomenon

Since the signal strength depends on the amplification process, the stability of the corresponding electric field is critical to maintain as few dead time as possible. Rapid instabilities are caused by sparks that can appear between the micro-mesh and the anode. If the applied voltage is above the breakdown voltage given by the Paschen law [23], sparks will develop. However, even below this limit, a single avalanche can reach a critical size, typically $10^7 - 10^8$ electrons, at which point a discharge will occur. This electron number is called the Raether limit [24]. Due to the discharge current, the voltage difference between the two electrodes drops until it cannot sustain the spark anymore. At this point, the amplification electric field is not sufficient for the avalanche phenomenon to occur. It takes some time (10^{-3} to 10^{-2} s) for the power supply to reestablish the nominal voltage. Moreover, sustained sparking can physically damage the detector and in particular the mesh as shown in Figure II.6 for extreme cases.

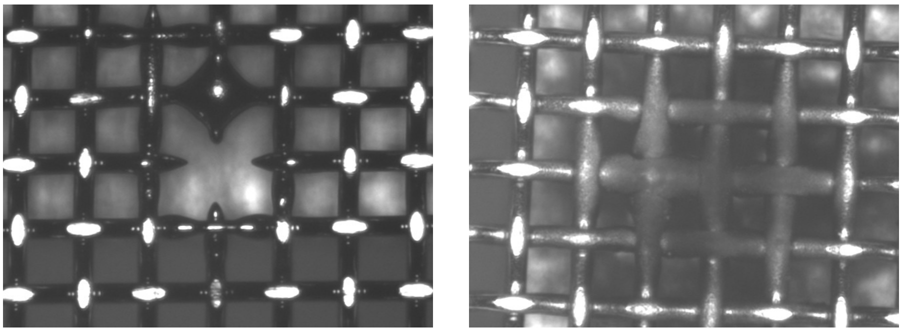

FIGURE II.6 – Two damaged meshes after heavy sparking.

II.A.2.d Gas properties

The gas inside a Micromegas chamber must have two main characteristics: to be ionized easily and to have a low electron affinity to avoid attachment. Indeed, if the crossing particle does not deposit enough energy for ionization to occur, it will not be detected. This is why the ionization energy of the gas has to be low, in a way to maximize the number of primary electrons created inside the conversion volume and to minimize zero ionization events. When primary electrons are created and drift toward the micro-mesh, they undergo collisions with the atoms. If these atoms are electronegative they will be prone to attach these free electrons and the corresponding signal will be lost because the drift velocity of the anions is $10^3 - 10^4$ times slower than that of the electrons. Moreover, during the avalanche process, an electron captured by an atom does not contribute to the signal amplification. Typical gases that fulfill these requirements are noble gas like Argon.[1] However, when a collision occurs between an atom and an accelerated electron, the atom or cation is often left in an excited state. It may get back to its fundamental state by emitting photons. By photo-electric effect, these photons can lead to the creation of new primary electrons which will be amplified. This extra signal is not spatially correlated with the ionizing particle path and will then degrade the measure of its position. The goal is then to capture the photons without creating additional electrons. This is done by another species put in the gas which is called the quencher. A good quencher is a molecule with numerous vibrational and rotational degrees of freedom that can be excited by photons. They will relax down by thermal effects. Typical used quenchers are carbon dioxide (CO_2), isobutane (iC_4H_{10}) or other molecular gases. Gas contamination by air or changes in the ratio between the noble gas and the quencher will alter the ionization and amplification processes and therefore impact the efficiency and the gain. For this reason, the quality of the gas throughout the operation has to be conserved *e.g.* by maintaining an over pressure inside the detector and continuously flushing the gas. The typical flow rate is a few liters per hour.

II.A.2.e Bulk technology

In order to maintain a uniform and constant gain, one has to take care of the gas purity but also of the strength of the electric field which is directly related to the gap between the micro-mesh and the anode. Originally, the mesh was maintained at a constant height by glued threads but this was not so robust nor very reliable. Improvements to make the amplification gap more homogeneous came from the PCB industry: the bulk technology [26]. It consists of laminating UV sensitive polymer on top of the anode (Figure II.7b) and then laminating the tightened mesh with another polymer layer on top of it. This way the mesh is completely held by the polymer but the detector sensitive area is covered as it can be seen in Figure II.7c. The detector is then exposed to UV light through a specific mask in order to harden the polymer outside the sensitive area and on tiny dots ($\sim 350\,\mu\mathrm{m}$) inside it (Figure II.7d). After a chemical development (etching) which removes all the non-hardened polymer, the sensitive area is cleared except on tiny spots where the polymer forms pillars to support the mesh (Figure II.7e). With this technique, the mesh is kept tight by the polymer on the detector sides and at a constant distance from the anode by the pillars, the result being shown in Figure II.7f.

---

[1] Micromegas operation with air has been demonstrated [25] but the very electronegative oxygen it contains is likely to capture a large part of the electrons

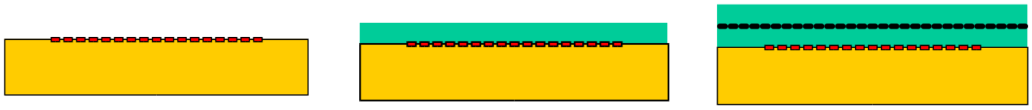

(a) Bare PCB.

(b) Coverlay laminated on top of the PCB.

(c) Coverlay sandwiched mesh laminated on top of the PCB.

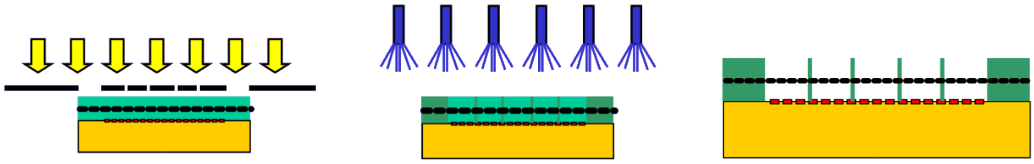

(d) UV light exposition through a mask.

(e) The coverlay etching with a NaOH solution.

(f) Finished bulk Micromegas.

FIGURE II.7 – Step by step sketch of the bulk process (courtesy of S. Aune).

II.A.2.f Resistive anode

To prevent the sparking process, one can act on different parameters. In particular, Alexopoulos *et al.* had the idea to slow down the electron evacuation by making the anode resistive [27]. Indeed, at the spark location, if the charges do not evacuate quickly, the anode voltage will rapidly drop close to the mesh potential so the spark cannot develop. Moreover, the voltage of the anode everywhere else is not affected. So the discharge current is reduced and maintained well below the maximum that can output the power supply. As a consequence, the electric field is kept very close to its nominal value, resulting in negligible dead time of the detector. In this configuration, the readout strips are not the anode anymore, this function is achieved by resistive strips on top of them as seen in Figure II.8. Their resistivity is between $100\,\mathrm{k\Omega}/\square$[1] and $1\,\mathrm{M\Omega}/\square$, and they are connected to the power supply through an additional resistor of a few tens of $\mathrm{M\Omega}$. In practice, this allows for the operation of the Micromegas with a grounded mesh and a positive high voltage applied to the resistive strips. This is particularly interesting as improperly cut wires of the micro-mesh can touch metallic parts of the detector during the manufacturing process creating short circuits. The grounded mesh operation can then prevent shortcuts or the fastidious removal of these wires with binocular inspection. The signal is induced on the readout structure by capacitive effects between the two strip layers.

II.A.3 Typical performance

Micromegas detectors are more and more used in high energy physics experiments because they fulfill most of the requirements to make an excellent tracking device. Using the bulk technology, the PCB industry is now capable of manufacturing such detectors at low cost. Moreover, large area detector construction is possible. Its spatial resolution is limited by the size of the anode pattern and the transverse diffusion

---

[1] For a constant thickness of resistive material, the resistivity measured between two electrodes is proportional to the distance between them but also inversely proportional to the extension of the resistive material perpendicular to the electrode axis. This way, the resistivity measured between two opposite sides of a square does not depend on the square size.

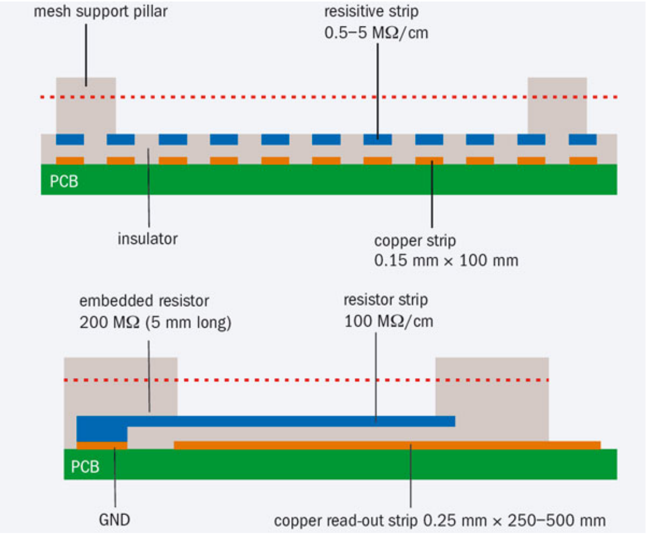

FIGURE II.8 – Sketch of the readout plane principle of a resistive strip Micromegas along the strip direction on top and perpendicular to it on bottom [27].

of drifting electrons so it can reach a precision under $100\,\mu\mathrm{m}$. Concerning the time resolution, precision lower than $10\,\mathrm{ns}$ can be achieved [28]. Because of manufacturing limitations while making the resistive layer (resistivity inhomogeneities), it has been shown however that this technology worsens the time resolution [29].

II.B Latest developments

II.B.1 2D strip readout

The Micromegas detector is mostly used as a tracking device. For this purpose, precise 3D points where a particle passed have to be identified. The Micromegas can provide a measure at its readout plane location. This way, the 2D position where a particle crossed this plane has to be measured. If a strip-based readout is used, only a 1D information is available: the position across the strip direction. A second chamber with strips placed perpendicularly with respect to the first one can be used to get the missing coordinate but it will reduce the overall efficiency and increase the material budget of the tracker. Indeed, the product of both the efficiency $\epsilon_{tot} = \epsilon_1\epsilon_2$ will be lower than the lowest individual efficiency of the chambers: $\epsilon_{tot} < \min(\epsilon_1, \epsilon_2)$. A second approach is to use readout pads instead of strips, the pad position will directly give a 2D information while using a single chamber. The drawback of this method is that it increases drastically the number of electronic channels needed. To read a detector of size $L \times l$ with a pitch of l_0, n_{tot} channels are needed:

$$n_L = \left\lfloor \frac{L}{l_0} \right\rfloor \tag{II.6}$$

$$n_l = \left\lfloor \frac{l}{l_0} \right\rfloor \tag{II.7}$$

$$n_{tot,strips} = n_L + n_l \tag{II.8}$$

$$n_{tot,pads} = n_L \times n_l \tag{II.9}$$

Where n_L (resp. n_l) is the number of readout elements along the length (resp. the width) and $x \mapsto \lfloor x \rfloor$ the floor function. The number of channels for a pad structure $n_{tot,pads}$ becomes much larger than $n_{tot,strips}$ for large and precise detectors.

A first alternative is to make electrical connections between the pads to form discontinuous strips like it has been done for the CAST [30] and ASACUSA [31] experiments. Another alternative emerged during the ATLAS New Small Wheel development with the resistive technique [32]. If a signal can be induced on strips below the resistive coating, it may be possible to induce it on two perpendicular layers stacked on each other. This way combines the advantage of having a single chamber and having fewer electronic channels like the designs uses in CAST and ASACUSA. However, it rises some technological challenges because the charge signal is split between the two readout layers. This also means that the distance between the layers has to be properly controlled, indeed the induced signal is decreasing with the distance between the readout strip and the resistive one. Moreover, there is a screening effect of the middle layer such that this layer must have a larger inter-strip distance, that is to say (to keep the pitch constant) a thinner width like it is shown on Figure II.9 and Figure II.17.

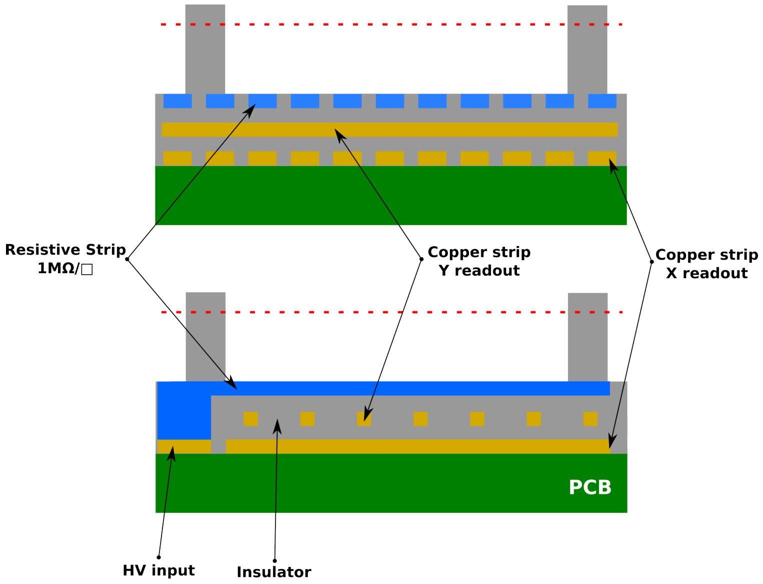

FIGURE II.9 – Sketch of the readout plane principle of a resistive strip Micromegas with 2D readout on two perpendicular views.

Nevertheless, using this layout induces some discrepancy between the X and Y signals. There is no particular change on the readout strips which are parallel to the resistive strips other than a lower amplitude. For the strips perpendicular to the resistive strips, however, there are two competing phenomena, the standard signal formation due to the electron avalanche and the signal induced by the charge diffusion inside the resistive layer. The charges created during the amplification process are collected on the resistive material. These charges will evacuate by moving along the strip which is perpendicular to the readout ones. So the charges are going away from the readout strip inducing a signal opposite to the avalanche one. Moreover, the evacuating charges will pass above neighboring readout strips, so according to the Sockley-Ramo theorem, the induced current sign will flip, forming a bipolar signal. The signal saved by the electronics is then the sum of these contributions in such a way that we can observe an undershoot on the center strips and a weak signal extending far away on many strips. This effect is shown in Figure II.10.

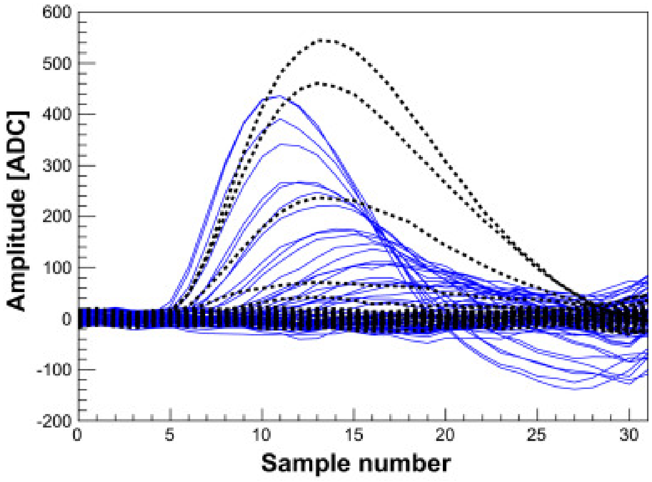

FIGURE II.10 – Plot of the signal (pedestal and common noise subtracted) induced in a 2D readout resistive Micromegas on strips parallel to the resistive ones in black and perpendicular to the resistive ones in blue.

II.B.2 Multiplexed readout

When operating a Micromegas detector, the collected signal is often spread over adjacent strips. This redundancy can be used to reduce the number of electronics channels needed to read each strip [33]. The goal is not to have a direct relation between the electronic channel to the position inside the detector anymore but to have such a relation with doublets of channels and more generally with k-uplets of channels as shown on figure Figure II.11. This was firstly developed to make low-cost cosmic bench in order to test detectors from hadronic physics experiments [34, 35].

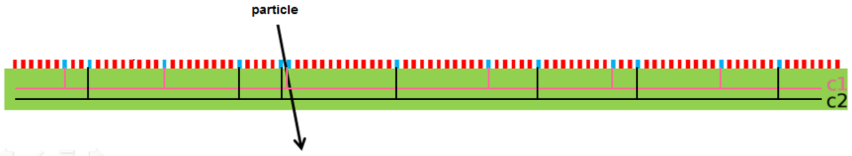

FIGURE II.11 – Sketch of the principle of genetic multiplexing illustrated by a particle which induces a signal on channel c_1 and c_2 [33].

Let's consider two electronic channels c_1 and c_2, each of them are wired to several strips in such a way that any strip connected to c_1 is not adjacent to any of the ones connected to c_2 except on one unique location s_1 and s_2. With this setup, if a signal is recorded on c_1 and c_2 simultaneously, it can be inferred that the particle crossed the detector at the location of s_1 and s_2. The multiplexing factor can be adjusted with respect to the data taking condition. Indeed, ambiguities may occur when it is not possible to distinguish the signals of several crossing particles. So the maximum multiplexing factor is determined by the rate the detector is supposed to undergo. Moreover, this factor is capped by the maximum number of unique doublets n_2 that can be created with n_C number of channels which is:

$$n_{2,max} = \frac{n_C(n_C - 1)}{2}. \tag{II.10}$$

Furthermore, in n_S strips, it exists $n_2 = n_S - 1$ doublets. So the maximum number of strips $n_{S,max}$ that can be read with n_C channels is:

$$n_{S,max} = \frac{n_C(n_C - 1)}{2} + 1. \tag{II.11}$$

II.C Micromegas readout electronics

Because the signal that has to be read out from a MPGD differs from other types of detectors, specific electronics have been developed. Indeed, the time width of the signal, its charge, its shape are some parameters that are different from one detector to another. Shaping electronics with a dynamic range adapted to the MPGDs have been developed at Saclay (IRFU/SEDI). In the recent years, three successive chips were designed following the same base idea. Each channel is connected to a charge sensitive amplifier (CSA) whose output is filtered and shaped. The result of this chain is stored in an analog circular memory made of a switched capacitor array (CSA): the amplitude is continuously stored at each time step. When a trigger occurs, the analog memory is read and digitalized by an ADC and then sent for storage.

A protection circuit is generally added between the detector and the CSA to avoid any chip damage in the case of a spark. To avoid such damage, a decoupling capacitor is usually placed before the CSA.

The first chip that was developed is AFTER (**A**SIC **f**or **T**PC **E**lectronic **R**eadout) for the T2K experiment [36]. Each chip can read 72 channels at one dynamic range in an interval from 120 fC to 600 fC, recording the signal samples at 1 MHz to 100 MHz[1]. The analog circular buffer is 511 buckets deep so for each from 1 to 511 time samples can be recorded. However, writing in the buffer is forbidden during reading operation leading to a dead time of about 2 ms.

The evolution of this chip is AGET (**A**SIC for **G**eneral **E**lectronics for **T**PC) [37] which is part of a worldwide collaboration whose purpose is to develop a universal electronics to read TPCs. Compared to the AFTER chip, the number of channels has been decreased to 64, the dynamic range upper bound pushed to 10 pC as well as the sampling rate to 100 MHz. Yet, the key new feature is the self-triggering capability. The chip is capable of generating a hit signal when the amplitudes pass over an adjustable threshold which can be used to trigger the whole acquisition on the MPGD signal itself without using any external trigger source.

The third evolution of this family of chips is the DREAM (**D**ead-time less **RE**adout **A**SIC for **M**icromegas) chip [38] whose diagram is shown in Figure II.12. Its characteristics are similar to AGET even if it has the same dynamic range as AFTER. However, while the previous chips could not save the signal during reading operation, the writing and reading to the DREAM circular buffer takes place in parallel so the dead time caused by the reading of the interesting signal is suppressed. This way, events

---

[1] The designed maximum recording rate is 50 MHz but extensive tests showed that it works up to 100 MHz.

can be read at rates of tens of kHz using DREAM, whereas the two previous ASICs were capped to $1\,\mathrm{kHz}$ due to dead-time. Moreover, this chip has been optimized to read large capacitance detectors.

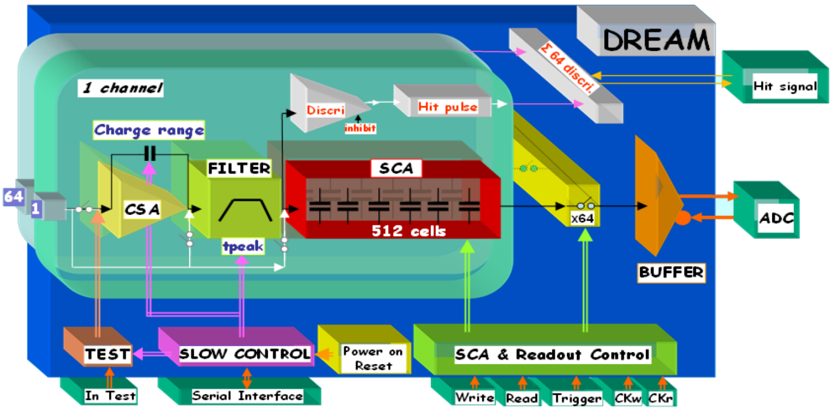

FIGURE II.12 – Diagram of the DREAM chip.

Tests comparing these electronics in the framework of this work will be presented in section III.A.

II.D MultiGen detector development

II.D.1 New detectors for muography

A genetic multiplexed Micromegas with a 1D readout was already extensively tested at Saclay. Targeting a decrease of complexity, the idea to develop a genetic multiplexed Micromegas having a 2D readout grew. Indeed, it allows to divide the number of chambers by a factor of two. Combining the multiplexing and the strip stack, prototypes were made. The first version demonstrated the feasibility of such a detector together with its actual performance. Mosaic making capabilities have been taken into account so dead surfaces at the edges of the detectors were minimized. In association with Elvia PCB industry, three prototypes were built and resulting in a second version after design optimization. This last version was produced extensively by ELVIA (24 detectors) and by CERN (8 detectors).

II.D.2 First prototype

II.D.2.a Description and characteristics

This prototype was a first step to test the performances of a 2D readout multiplexed Micromegas [39]. It inherits from multiple characteristics of older prototypes made at Saclay in 2013 and presented in [33]. It has an active area of $50 \times 50\ \mathrm{cm}^2$ on a $56 \times 56\ \mathrm{cm}^2$ wide PCB. The readout is made of 1024 strips for each coordinates under 1024 resistive strips like presented in Figure II.9, so the pitch is $l_0 = 488\,\mu\mathrm{m}$. The bottom strips are $388\,\mu\mathrm{m}$ wide which makes the inter-strip $100\,\mu\mathrm{m}$ wide, whereas the middle layer has reversed proportions: the inter-strip is made large ($388\,\mu\mathrm{m}$) in order not to screen the signal for the bottom layer as explained in section II.B.1. The strips are multiplexed by being connected to each other in 61 different channels in the so called *multiplexing bus*, this bus being perpendicular to the strips it connects and located at the edge of the active area. This displaced the active area from the center of the PCB and pushed it on a corner as shown in Figure II.13a.

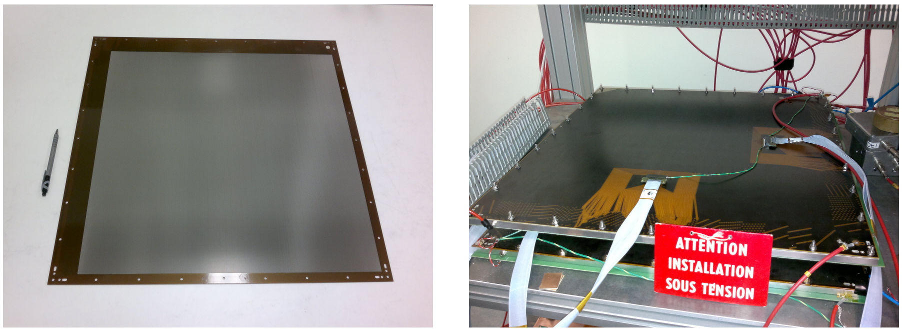

(a) PCB and active area view. (b) Operating detector.

FIGURE II.13 – Version 1 of MultiGen 2D.

They have been operated with a 1 cm drift gap provided by an Aluminum frame. A PCB with a plain Copper plane makes the cathode side of this frame. The Copper plane faces the detector active area. Each PCB is screwed to the frame and the gas tightness is ensured by silicone seals.

All the prototypes were extensively tested inside the Saclay cosmic bench using a Ar-iC_4H_{10} mixture in 90:10 proportion. Each detector has an efficiency above 95% with a good homogeneity while having a resolution below 300 μm as shown in Figure II.14[1]. Their time stability has been shown by their daily use for over 18 months.

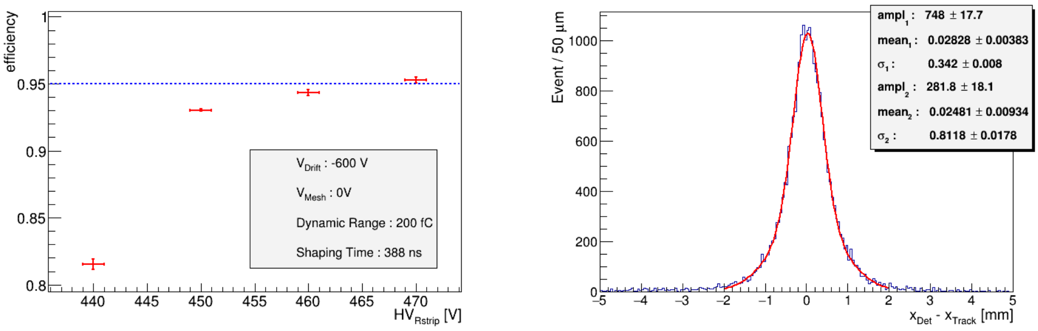

(a) Efficiency measured at different amplification fields. (b) Measured position compared to muon track position.

FIGURE II.14 – Characterization of one MultiGen 2D prototype.

II.D.2.b Drawbacks and design flaws

Some practical details have been neglected during the design of this first version. The position of the active area which is very close to a corner of the PCB is a problem because of the distance to the frame forming the chamber. To ensure the gas tightness, this frame has to be pressed on the PCB in such a way the silicone seal is in contact

---

[1] The plot shows the fitted residual whose standard deviation does not exactly correspond to the detector resolution since the extrapolated track position is not perfectly known.

with both parts. Even if the mesh is kept at the same electrical ground as the frame, the pressure brings the mesh closer to the anode. Therefore, a current appeared which forbade to increase the gain of the detector at a level where it is efficient. To avoid this problem, the detector is operated by losing out the pressure at this corner as shown in Figure II.15. Gas is therefore slightly leaking so the detector is flushed with a higher flow to keep a good gas mixture inside the chamber.

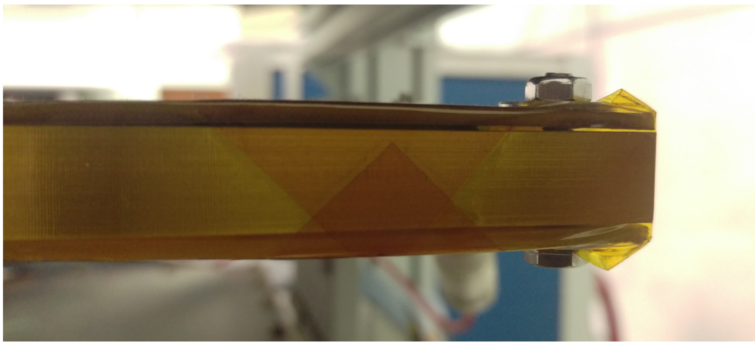

FIGURE II.15 – MultiGen corner not properly sealed.

Another characteristic that was not sufficiently addressed during the design of this prototype is the electrical grounding and shielding. Proper electrical mass connections were not possible and high voltage filters could not be placed on the detector itself as shown during operation in Figure II.13b. Moreover, no shielding layer is present on the back of the PCB so the noise levels are degraded in particular on the most external layer of strips. This effect is shown on Figure II.16, which compares the noise level for each channel of four different detectors where each measured coordinate is separated by red dotted lines. The external layer of strips (measuring the x coordinate) corresponds to the channels 0 to 61, 183 to 243 and 305 to 365.

A degraded resolution is also observed: the measured $280\,\mu\mathrm{m}$ is largely above the minimum theoretical value of $l_0/\sqrt{12} = 141\,\mu\mathrm{m}$. One origin of this degradation is the shape of the detector. Indeed, the PCB is quite thin and maintained only on the edge by the aluminum frame. Due to the mesh tension, the PCB is not flat and is bulging outward. The other causes are detailed later in section II.D.3.b.

II.D.3 A second version of the MultiGen detector

To build the bench for the M^3 experiment (described in details later on section V.D), an optimized detector was required and a second version of the 2D readout MultiGen detector was thus developed. This new design also allowed solving problems identified in the first prototype design.

II.D.3.a Design enhancements

The maximum number of channels that can be used to read each coordinate of one detector is capped by the connector capacity which is 64. Due to the multiplexing construction, the number of channels has to be prime, so the number of used channels is the greatest prime smaller than 64 which is 61. The multiplexing factor used in the first prototype is 17 but it contained only 1024 strips due to historical reasons. The maximum readable strips is $17 \times 61 = 1037$ so 13 strips were added. In the second

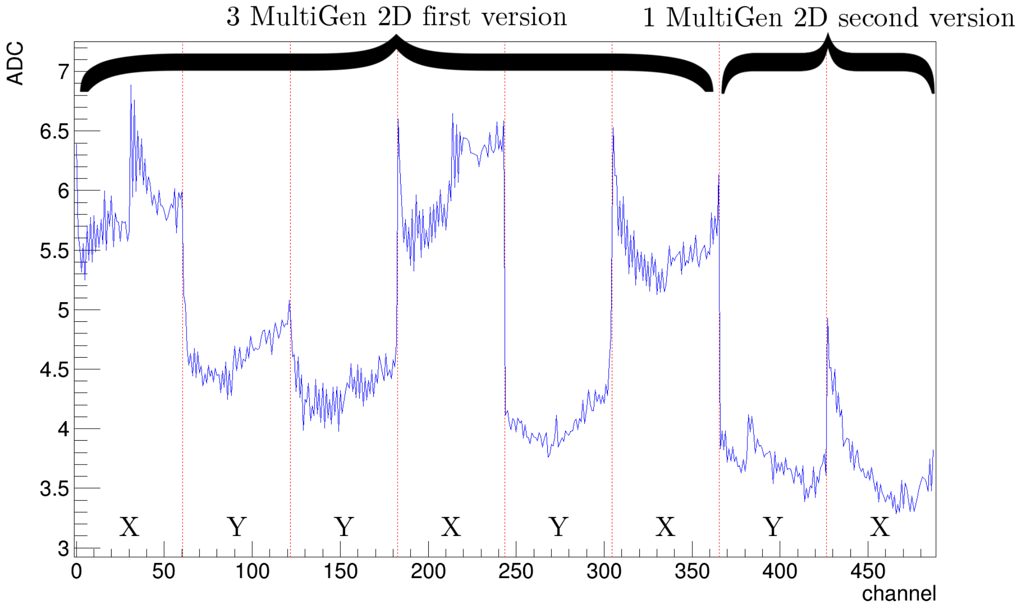

FIGURE II.16 – Plot of channel by channel noise level after pedestal subtraction and before common noise subtraction for the 8 coordinates measured by 4 detectors.[1]

version, the pitch is then slightly reduced to $l_0 = 482\,\mu\text{m}$. The inter-strip and strip widths of both coordinates were reduced accordingly, and the strip layout is shown in Figure II.17.

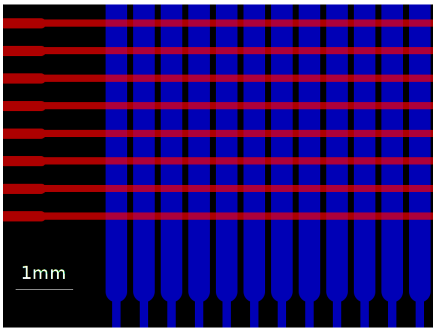

FIGURE II.17 – Strip and inter strip layout of a MultiGen V2 detector, lower strips in blue, intermediate layer in red.

To address the corner problem, the active area was placed at the center of the PCB. This modification implies that the multiplexing bus has to be shifted in a new internal PCB layer, partially under the active area. To avoid crosstalk and to enhance the overall shielding, copper layers are also added. The effect of this shielding on the noise level before common noise subtraction is shown in Figure II.16 by comparing three first version detectors with the first operational second version MultiGen. Increasing the number of layers serves another purpose: it thickens the PCB so it is much more rigid. When fastened to the aluminum frame, the flatness is improved compared to the first prototype.

---

[1] Each coordinate is read by a single ASIC, the overall parabolic shape that can be observed is partially explained by the routing inside the chip. This effect is present in the three chips of the familly: AFTER, AGET and DREAM.

By solving the corner problem, the gas leaks are also diminished dramatically. Sealed operation becomes theoretically possible.

II.D.3.b Characteristics and performance

The characteristics remain quite close to the first prototype: 1037 strips in each direction read a 50×50 cm^2 active area in the center of a 54.6×54.6 cm^2 PCB. To enhance the S/N ratio by increasing the number of primary electrons the drift gap is widened to $1.5\,\mathrm{cm}$. This wider drift gap is supposed to help the muon reconstruction by allowing a micro-TPC mode. As shown in Figure II.18, the efficiency plateau is larger than the one of the first prototype. The 2D efficiency (Figure II.18c) is larger than the product of both coordinate efficiencies because of the large correlation ($\sim 70\,\%$) of the signal formation. Moreover, the E014 detector is the first detector built by ELVIA which was successfully tested, validating their expertise. The CERN and ELVIA detectors show similar performance.

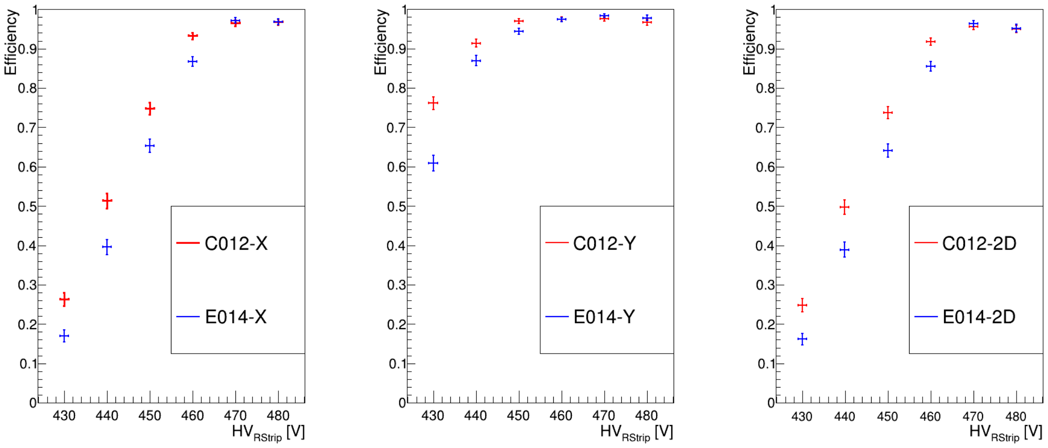

(a) 1D efficiency of the coordinate perpendicular to the resistive strips.

(b) 1D efficiency of the coordinate parallel to the resistive strips.

(c) 2D efficiency.

FIGURE II.18 – Efficiency plateau of two second version MultiGen 2D, one manufactured at CERN (C012) and the other by the ELVIA company (E014). Measurements made with a 90:10 Ar-iC$_4$H$_{10}$ mixture, $U_{\text{Drift}} = -500\,\mathrm{V}$ and $U_{\text{Mesh}} = 0\,\mathrm{V}$.

Resolutions down to $250\,\mu\mathrm{m}$ are measured (Figure II.19). It is still above the theoretical limit determined by the pitch: $l_0/\sqrt{12} = 139\,\mu\mathrm{m}$ because of various effects. The predominant outcome is the non-contiguity of the signal. This effect is explained in details in section III.F.1.

However, characteristics of the resistive layer still induce some clustering and demultiplexing problems. Indeed, differences of resistivity from one detector to another lead to strong variation of the cluster size in the coordinate perpendicular to the resistive strips because of the charge spread as shown in Figure II.20. Moreover, using the standard screen printing to manufacture the resistive layer, the maximum achievable resistivity induces cluster sizes over 17. Because the largest unique k-uplets are 17 strips wide, it is not possible to match this cluster with a unique position inside the detector. Furthermore, the inhomogeneities inside a detector degrades the time resolution, forbidding the use of enhanced clustering techniques such as the

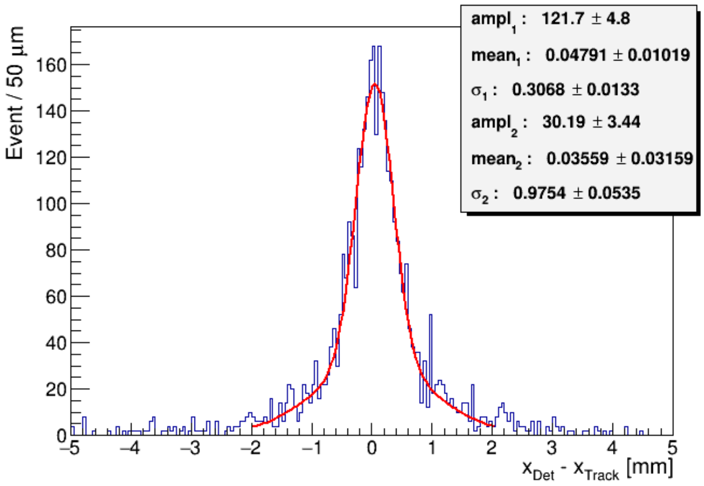

FIGURE II.19 – Position measured by a second version MultiGen compared to muon track position for perpendicular tracks ($\Delta\theta < 5.7°$).

micro-TPC method. New prototype with resistive layers made using the Diamond Like Carbon technique are planned since ten times higher resistivity can be achieved with a better homogeneity [40].

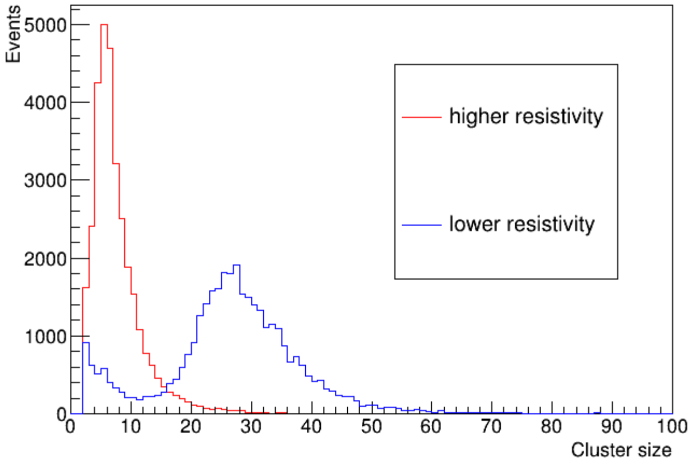

FIGURE II.20 – Cluster size distribution measured in two different second version MultiGens.

The sum up of the characteristics of each prototype is presented in Table II.1

Prototype	**V1**	**V2**
Active area [cm^2]	50×50	50×50
Total area [cm^2]	56×56	54.6×54.6
Channel number	61	61
Strip number	1024	1037
Pitch [µm]	488	482
Resolution [µm]	280	250
Drift gap height [cm]	1	1.5
Efficiency	$> 96\%$	$> 96\%$

TABLE II.1 – MultiGen characteristics.

Chapter III

Experimental Developments

Muography data taking campaigns bring high energy physics detectors and equipment outside the laboratory. It has then to fulfill the constraints of various outdoor environments concerning for example stability, power consumption, compactness or autonomy.

III.A Readout electronics

Due to the multiplexing of the MultiGen detectors, the capacitance of each channel ($\sim 2\,\mathrm{nF}$) is much higher than a typical MPGD. Since it is a source of a deterioration of the signal over noise ratio S/N, adapted electronics have to be used. For the CLAS12 experiment at Jefferson Laboratory (USA), a Micromegas vertex tracker has been designed. Because of the stringent place and material budget restrictions, an off-detector front-end electronics had to be developed. The connection between the electronic and the detectors is made by long (up to $2.2\,\mathrm{m}$) micro-coaxial cables. This increases the total capacitance up to $200\,\mathrm{pF}$ which thus becomes an important issue for this experiment. This is why the developed electronics is optimized for high-capacitance: the DREAM chip integrated into the FEU (**F**ront-**E**nd **U**nit) readout card. This electronics turned out to be well adapted to read the MultiGen detectors. Each DREAM chip can read 64 channels *i.e.* one coordinate of a MultiGen. The FEU card controls 8 of these ASICs, one can then read four MultiGen with a single readout card. When more detectors are required, the use of a TCM (**T**ime and **C**lock **M**odule) [41] is needed to synchronize multiple FEUs by providing a common clock and to propagate the trigger signals.

Tests were made using AGET and FEMINOS cards to compare both electronics using four first version MultiGen flushed with an Ar-iC_4H_{10} 95:5 gas mixture. The signal over noise ratio was compared between the two electronics setups:

- 1 FEU
- 2 FEMINOS synchronized with 1 TCM[1]

The performance using both electronics did not present a significant discrepancy. Practical criteria were then used to choose the final electronics: the DREAM setup is less complex (only one component) and uses less power.

---

[1] Two cards were indeed used as a FEMINOS card bears only four AGET, each one reading 64 channels.

As described in section II.C, a decoupling capacitor protects the ASIC but the MultiGens are resistive Micromegas so the protection is *a priori* no longer needed. Readout using an unprotected FEU card has therefore been tested. However, the signal and noise amplitude improvement was so large that, whatever the dynamic range used, it often saturated. So the unprotected option was ruled out. Even if this capacitor cannot be removed, its capacitance has an influence on the S/N ratio because it affects the charge transfer to the ASIC: the more capacitive it is, the more charge is transferred. Four different capacitances were compared: $220\,\mathrm{pF}$, $470\,\mathrm{pF}$, $1\,\mathrm{nF}$ and $2.2\,\mathrm{nF}$. The tests were made using a modified FEMINOS: each AGET was protected by capacitances of a specific value. For the four detectors, the Y measuring strips were connected to an unmodified FEMINOS and each X measuring strips were then connected to an AGET through a different capacitance on the modified FEMINOS. To rule out detector effects, four runs have been taken so each detector-capacitance combination was measured. This method allows us to average out the detector effect and to measure accurately the signal over noise ratio. The noise level is defined as the standard deviation of the signal amplitude after pedestal and common noise subtraction for signal-less event. These events are recorded using a random trigger following an exponential law of mean $20\,\mathrm{Hz}$. The signal level is defined as the mean over all reconstructed muons of the amplitude of the strip bearing the maximum charge. The results are shown on Table III.1.

C [pF]	$\boldsymbol{S/N}$
220	24±4
470	24±5
1000	23±5
2200	23±1

TABLE III.1 – Influence of the decoupling capacitor on the signal over noise ratio.

As expected, the decoupling capacitance has indeed some influence on the signal but also on the noise. All in all, the S/N ratio did not change much and the common mode noise was slightly higher with more capacitance. These tests are not as relevant as expected because the AGET chip is not well adapted to the MultiGens capacitance. As explained in the next section, the noise increase can hinder the self-trigger operation so the nominal $220\,\mathrm{pF}$ version was chosen.

III.B Self-triggering operation

A triggering system is a key part of the data acquisition. Since the permanent recording of the signals is not realistic, it is needed to specify when the recording should occur *i.e.* to discriminate interesting signal from the noise. In other words, the crossing of a muon has to be detected to trigger the acquisition. Most of the time with MPGDs, an external system is used, like a coincidence signal between two scintillators. However, modern electronics can trigger themselves directly from the signal of the Micromegas. The DREAM chip, the FEU readout card and the TCM card have this capability. The so-called self-triggering appears at three levels as seen in Table III.2. At first, each chip can output a triggering signal considering the channel signal amplitude and the multiplicity of hit channels. For each of these parameters, there is a matching tunable threshold. Some channels can be specifically disabled, for example if they are not connected to the detector. In our case, the MultiGen detector only uses the 61 first channels of the 64 available so the last three are disabled. Each of the eight DREAMs then sends its hit signal to the FEU, the signal stays on a high state for as long as the multiplicity condition is verified. The length of each chip hit signal is then constrained and a multiplicity condition is applied. For a trigger signal to be generated, the multiplicity condition has to stay true during a time window whose length can be programmed. If needed, topological conditions can be used to refine the trigger. The topological trigger is a lookup table in which the DREAMs hit signal combinations are distinguished for the trigger to actually occur: because each DREAM outputs a binary hit signal, through the lookup table, the FEU can distinguish $2^8 = 256$ cases. If multiple FEUs are used and synchronized with a TCM, a higher level trigger has to be defined. In multiplicity mode, each FEU sends a boolean signal to the TCM which will then apply a multiplicity criterion on how many FEUs are triggered. In topological mode, the output of the lookup table is a tunable 4-bit word. The TCM will add each bit of each word it receives and will compare it to the multiplicity criterion.

level	measure	threshold type
DREAM	signal amplitude channel multiplicity	min min
FEU	signal TOT hit TOT chip multiplicity	min min min and topological
TCM	multiplicity	min and max

TABLE III.2 – Self triggering parameters and thresholds.

Tuning all the parameters is a crucial step to build an efficient trigger and optimize the trade-off between purity (*i.e.* the capacity of rejecting noise) and efficiency (*i.e.* avoiding the rejection of proper events). This becomes particularly tricky when dealing with a noisy environment. Multiple factors can increase the noise inside the instruments such as EM wave emitting devices nearby or unfiltered power supplies. Moreover, since the various thresholds are fixed for a given run, variations of the detector signal with time can alter the triggering capabilities. For example, when using an external trigger, the only constraint is that the sum of the common noise and the signal amplitude is less than the saturation limit. However, using the self-triggering mode, this constraint is not stringent enough because the common noise amplitude can still be above the amplitude threshold.

III.C High voltage power supply

The operation using a self-triggering system is a first step toward the reduction of the complexity of the system. Operation in the field, outside the laboratory, appeals for a simple system which is autonomous in particular in terms of power supply. Micromegas detectors need two high voltages of a few hundreds of volts: one for the drift field and one for the amplification field. Since currents flowing through the detectors are weak ($< 1\,\mu\text{A}$), the needed power is low. Recently, low consumption high voltage power supply modules have been made by CAEN.[1] Powered by 12 V DC current, they can provide a single suitable high voltage while consuming less than 0.4 W. They are controlled by two analog settings: the output voltage and the maximum current. It is also possible to monitor the output voltage, output current and the over current status ("tripping" status). A dedicated control board (HVPS board) has been designed at Saclay to control and monitor up to six of these modules. Constraints on the voltage and noise of the drift field are not as stringent as for the amplification one so a unique supply powers several detectors. This way, five modules can power four MultiGen detectors. As shown in Figure III.1, the HVPS board is composed of one ASIC which controls the high voltage modules. These modules are analog: the parameters are set by a voltage between 0 V and $U_{ref} = 5\,\text{V}$. The monitored values are sent back the same way. The ASIC role is to make the conversion between digital and analog values using DACs (**D**igital to **A**nalog **C**onverter) and ADCs (**A**nalog to **D**igital **C**onverter) but also to make the communication with the controlling computer. This communication can be made via an I2C (**I**nter-**I**ntegrated **C**ircuit) or SPI (**S**erial **P**eripheral **I**nterface) bus.

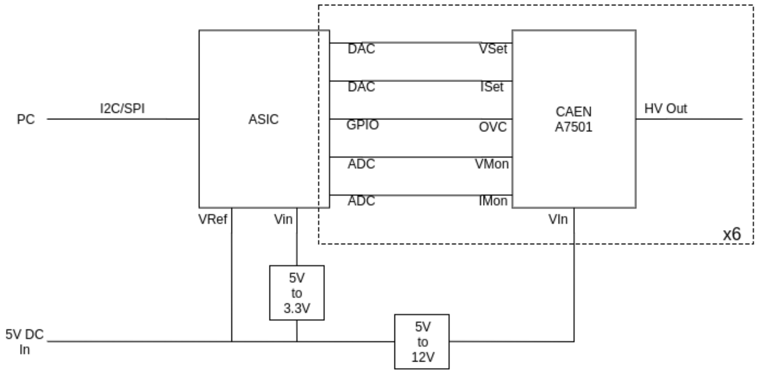

FIGURE III.1 – Scheme of the HVPS board.

A slow-control software have been developed to manage the communication with the chip, set the high voltage parameters and monitor them. This software whose interface is shown on Figure III.2 allows for live monitoring in addition to the periodical saving of the values to the disk. It also collects data from environmental sensors in order to change the voltage with respect to the conditions as discussed in section III.D.3. A FEU status can also be monitored in order to avoid damage by preventing high voltage to be set on while the FEU is powered off and by switching the FEU off when an overheating signal is received. Finally, current run monitoring can be fetched in order to make a feedback between the voltage and the mean signal amplitude inside the detector as discussed in section III.D.4.

III.D Environmental effects on Micromegas operation

III.D.1 Gain and amplification voltage dependence

As explained in section II.A.2.a, the gain inside the amplification gap is dependent of the electron mean free path. If it is too short, the acquired energy between two

---

[1] The module used is the A7501 model: A7501P outputting positive voltage to polarize the resistive strips and A7501N outputting negative voltage to polarize the cathode.

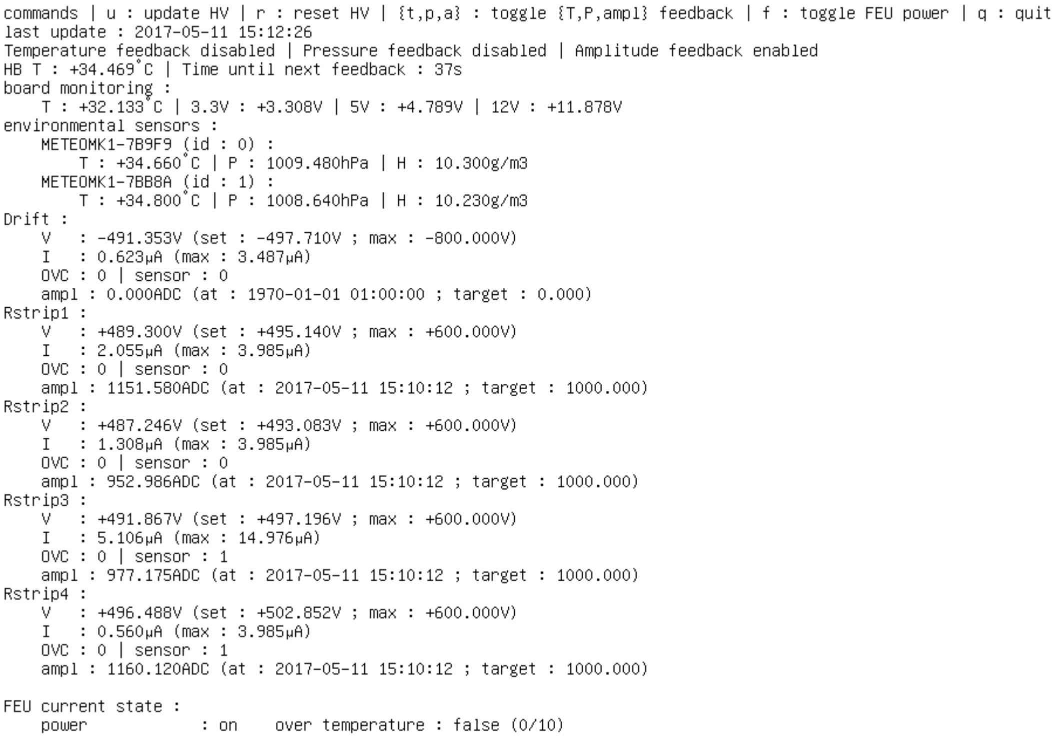

```
commands | u : update HV | r : reset HV | {t,p,a} : toggle {T,P,ampl} feedback | f : toggle FEU power | q : quit
last update : 2017-05-11 15:12:26
Temperature feedback disabled | Pressure feedback disabled | Amplitude feedback enabled
HB T : +34.469°C | Time until next feedback : 37s
board monitoring :
    T : +32.133°C | 3.3V : +3.308V | 5V : +4.789V | 12V : +11.878V
environmental sensors :
    METEOMK1-7B9F9 (id : 0) :
        T : +34.660°C | P : 1009.480hPa | H : 10.300g/m3
    METEOMK1-7BB8A (id : 1) :
        T : +34.800°C | P : 1008.640hPa | H : 10.230g/m3
Drift :
    V   : -491.353V (set : -497.710V ; max : -800.000V)
    I   : 0.623μA (max : 3.487μA)
    OVC : 0 | sensor : 0
    ampl : 0.000ADC (at : 1970-01-01 01:00:00 ; target : 0.000)
Rstrip1 :
    V   : +489.300V (set : +495.140V ; max : +600.000V)
    I   : 2.055μA (max : 3.985μA)
    OVC : 0 | sensor : 0
    ampl : 1151.580ADC (at : 2017-05-11 15:10:12 ; target : 1000.000)
Rstrip2 :
    V   : +487.246V (set : +493.083V ; max : +600.000V)
    I   : 1.308μA (max : 3.985μA)
    OVC : 0 | sensor : 0
    ampl : 952.986ADC (at : 2017-05-11 15:10:12 ; target : 1000.000)
Rstrip3 :
    V   : +491.867V (set : +497.196V ; max : +600.000V)
    I   : 5.106μA (max : 14.976μA)
    OVC : 0 | sensor : 1
    ampl : 977.175ADC (at : 2017-05-11 15:10:12 ; target : 1000.000)
Rstrip4 :
    V   : +496.488V (set : +502.852V ; max : +600.000V)
    I   : 0.560μA (max : 3.985μA)
    OVC : 0 | sensor : 1
    ampl : 1160.120ADC (at : 2017-05-11 15:10:12 ; target : 1000.000)

FEU current state :
    power            : on    over temperature : false (0/10)
```

FIGURE III.2 – Screenshot of the HVPS control software.

collisions may not be sufficient to induce further ionization and if it is too long, the number of ionizations inside the gap is decreasing. As a consequence, at constant field the gain depends on the gas molecular density ρ_n which is, according to the perfect gas law:

$$\rho_n = \frac{P}{k_B T} \tag{III.1}$$

The pressure inside the detector is greater but close to the atmospheric pressure P_a so it can vary of the order of a few percent. Inside a laboratory, the temperature variations are quite low (a few percent) but outside, in a non-controlled environment, these variations can be more than 10% and strongly affect the gain. Since we use the Micromegas as a tracking detector, it may not be a problem. However, using a self-triggering system, if the gain variations lower the signal amplitude below the triggering threshold, the efficiency of the whole system is affected. Also, if the signal is saturating, the determination of the charge barycenter will be biased so the spatial resolution is degraded. Therefore, a stabilization of the gain is needed by adjusting the amplification high voltage over time.

The gain of a Townsend avalanche has been expressed in Equation II.4. Using the Townsend coefficient parametrization (Equation II.5), the expression of the gain as a function of the field E and the molecular density ρ_n is [42]:

$$G = \exp\left(A\rho_n d \exp\left(\frac{-B\rho_n}{E}\right)\right) \tag{III.2}$$

Let A_n (resp. B_n) be the normalization of A (resp. B) with respect to k_B:

$$A_n = \frac{A}{k_B}\ ;\ B_n = \frac{B}{k_B} \tag{III.3}$$

Therefore, using the perfect gas law (Equation III.1) and the relation between the field and the amplification voltage $U = Ed$, the gain expression becomes:

$$G = \exp\left(\frac{A_n P d}{T}\exp\left(\frac{-B_n P d}{TU}\right)\right) \tag{III.4}$$

To explicit the variations of G with respect to the environment parameters (T, P) the derivative is computed:

$$\frac{\partial G}{\partial P} = G\frac{A_n d}{T}\left(1 - \frac{B_n P d}{TU}\right)\exp\left(\frac{-B_n P d}{TU}\right) \tag{III.5}$$

$$\frac{\partial G}{\partial T} = -\frac{P}{T}\frac{\partial G}{\partial P} \tag{III.6}$$

As a consequence, there are two regimes:

$$\frac{B_n d}{U} < \frac{T}{P} \quad\Rightarrow\quad \frac{\partial G}{\partial P} > 0 \text{ and } \frac{\partial G}{\partial T} < 0 \tag{III.7}$$

$$\frac{B_n d}{U} > \frac{T}{P} \quad\Rightarrow\quad \frac{\partial G}{\partial P} < 0 \text{ and } \frac{\partial G}{\partial T} > 0 \tag{III.8}$$

Moreover, for a given gas at a given (T, P) environmental conditions and for a given detector with an amplification gap of height d, the needed voltage U to have a gain G can be inferred as:

$$U = \frac{B_n P d}{T \ln\left(\dfrac{A_n P d}{T \ln G}\right)} \tag{III.9}$$

As before, at a constant gain G, there are two regimes for the dependence of the voltage with respect to (T, P):

$$\frac{A_n d}{e \ln G} > \frac{T}{P} \quad\Rightarrow\quad \frac{\partial U}{\partial P} > 0 \text{ and } \frac{\partial U}{\partial T} < 0 \tag{III.10}$$

$$\frac{A_n d}{e \ln G} < \frac{T}{P} \quad\Rightarrow\quad \frac{\partial U}{\partial P} < 0 \text{ and } \frac{\partial U}{\partial T} > 0 \tag{III.11}$$

where e is the Napier Constant. Using the Ar-iC$_4$H$_{10}$ 95:5 mixture values of $A_n = 5.1\times10^3\,\mathrm{Km^{-1}Pa^{-1}}$ and $B_n = 4.0\times10^5\,\mathrm{VKm^{-1}Pa^{-1}}$ extrapolated from [43, 44], the gap width of the MultiGen detector $d = 128\,\mu\mathrm{m}$, the gain during operation $G \sim 4\times10^4$, and the normal environmental conditions $(T_N, P_N) = (20\,°\mathrm{C}, 1000\,\mathrm{hPa})$, the dependence of U (resp. G) with respect to the temperature should be negative (resp. positive) but experimentally it is positive (resp. negative) and strongly depends on the gas mixture as shown in section III.D.2.

$$\left.\frac{\partial U}{\partial T}\right|_{th,T_N,P_N} < 0\,;\ \left.\frac{\partial G}{\partial T}\right|_{th,T_N,P_N} > 0 \tag{III.12}$$

$$\left.\frac{\partial U}{\partial T}\right|_{exp} > 0\,;\ \left.\frac{\partial G}{\partial T}\right|_{exp} < 0 \tag{III.13}$$

Moreover, we are mainly using two different gas mixtures: the T2K one (Ar-CF$_4$-iC$_4$H$_{10}$ 95:3:2) and the 5 % isobutane one (Ar-iC$_4$H$_{10}$ 95:5). Comparing the behavior of the MultiGen between both mixtures, we observe that the variation of gain with temperature is more important with the T2K gas. However, at a constant gain, the variation of the voltage is more important with $5\,\%$ isobutane and argon: $0.67\,\mathrm{VK^{-1}}$ compared to $0.55\,\mathrm{VK^{-1}}$.

III.D.2 Measure of gain variations with respect to T and P

During an outdoor experiment showing the full day-night cycle of the temperature, the variation of the signal amplitude induced by cosmic muons was monitored in different conditions. Three stacked triggering detectors were used to track the cosmic muons crossing the apparatus. They were flushed with an Ar-iC$_4$H$_{10}$ $95{:}5$ gas mixture at a flow rate of $2\,\mathrm{Lh^{-1}}$. To provide a stable trigger, their gains were stabilized using a technique described later. A test detector was placed between these detectors. It was flushed with an Ar-CF$_4$-iC$_4$H$_{10}$ $95{:}3{:}2$ gas mixture at a flow rate of $1\,\mathrm{Lh^{-1}}$. The temperature and pressure of the gas mixture were monitored both at the input and at the output of the detector. This way, the signal amplitude of cosmic muons crossing the test detector can be monitored and its variations with respect to the environmental variables can be measured. During a one day experiment, the test detector was operated with a constant amplification voltage: $U = 435\,\mathrm{V}$. Since the influence of the (T, P) variations on the primary ionization process is negligible compared to the influence on the gain, the variation of the gain is proportional to the variation of the amplitude of the signal induced by muons. This variation is shown in Figure III.3. As stated in Equation III.13, the amplitude decreases with the temperature at a rate of roughly $-17.9\,\mathrm{ADC/K}$, this rate being itself P-dependent.

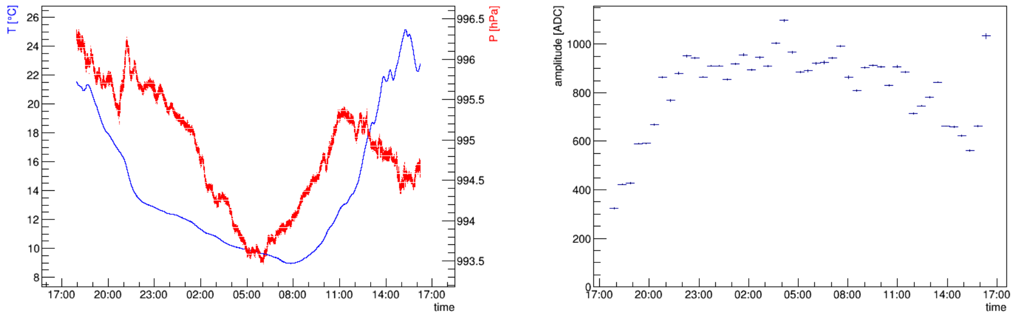

(a) Variations of (T, P)

(b) Variations of the signal amplitude

FIGURE III.3 – Variations of the signal amplitude while using a second version MultiGen flushed with an Ar-CF$_4$-iC$_4$H$_{10}$ $95{:}3{:}2$ gas mixture at a constant amplification voltage $U = 435\,\mathrm{V}$.

III.D.3 Correcting the voltage according to the environmental conditions

For conditions close to the normal (T_N, P_N), the voltage U can be written in function of the voltage at normal conditions $U_N = U(T_N, P_N)$ and the difference of the pressure (resp. the temperature) with respect to the standard reference $P = P_N + \Delta P$ (resp. $T = T_N + \Delta T$) as:

$$U = U_N + a_T \Delta T + a_P \Delta P \tag{III.14}$$

$$a_T = \frac{U_N}{T_N}\left(1 + \frac{U_N}{B_n P_N d}\right) \tag{III.15}$$

$$a_P = \frac{U_N}{P_N}\left(1 - \frac{U_N}{B_n P_N d}\right) \tag{III.16}$$

For the T2K gas, a 95:3:2 Ar-CF_4-iC_4H_{10} mixture, the experimentally determined coefficients are: $a_T \sim 0.5\,\mathrm{VK}^{-1}$ and $a_P \sim 50\,\mathrm{mVhPa}^{-1}$. The same way as before, this adjustment can be tested. The results are shown in Figure III.4. Since the temperature coefficient was not perfectly optimized, the amplitude is not made constant but the effect of temperature is tempered: the coefficient is slightly too high so, instead of decreasing at high temperature, the amplitude increases. This experiment was made during one day so the variations with respect to the pressure were negligible. Adjusting the temperature and pressure coefficients for a long period and for variations of the temperature of $30\,\mathrm{K}$ and of the pressure of $50\,\mathrm{hPa}$ is a much more difficult task. This is because the variation of temperature ($\sim 10\%$) is too high for the linearization to be accurate. Moreover, it requires sensors inside the gas because its temperature and pressure do not vary the same way as the air or between several detectors, in particular some delay may occur during the daily temperature cycle as shown in Figure III.5. This effect is important during fast variations of the temperature *e.g.* when the sun is shining on the detector.

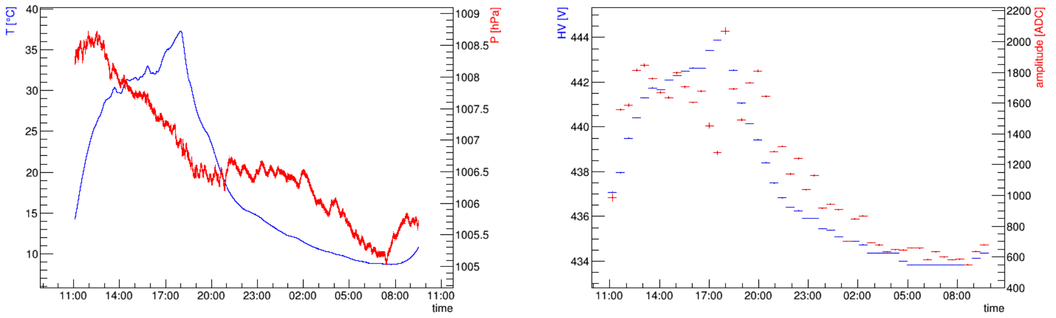

(a) Variations of (T, P) (b) Variations of the signal amplitude and U

FIGURE III.4 – Variations of the signal amplitude while using a temperature dependent voltage. Measured with $a_T = 0.38\,\mathrm{VK}^{-1}$, using a second version MultiGen flushed with an Ar-CF_4-iC_4H_{10} 95:3:2 gas mixture.

III.D.4 Improving the gain stability over time

A better way to deal with this problem is to monitor the signal amplitude inside the detector in real time and to make a feedback, adjusting the voltage periodically to reach a target amplitude. Because the individual signal amplitude is subject to stochastic fluctuations, an average amplitude is calculated. There is a trade-off between sufficient statistics in the low muon flux and the gain variation speed due to changes in environmental conditions. The implemented solution is to compute the average amplitude of about 1000 muons (which corresponds to $5\,\mathrm{min}$ at $3.5\,\mathrm{Hz}$). This mean amplitude $S(t_i)$ is compared to the target one S_T and the amplification voltage $U(t_i)$ is changed with respect to the difference:

$$U(t_{i+1}) = U(t_i) + a_S(S(t_i) - S_T) \tag{III.17}$$

Where a_S is a set parameter. For the T2K gas, a_S of the order of $-1\,\mathrm{mV/ADC}$ is suitable. Using this convention, $a_S < 0$ because the gain increases as the field

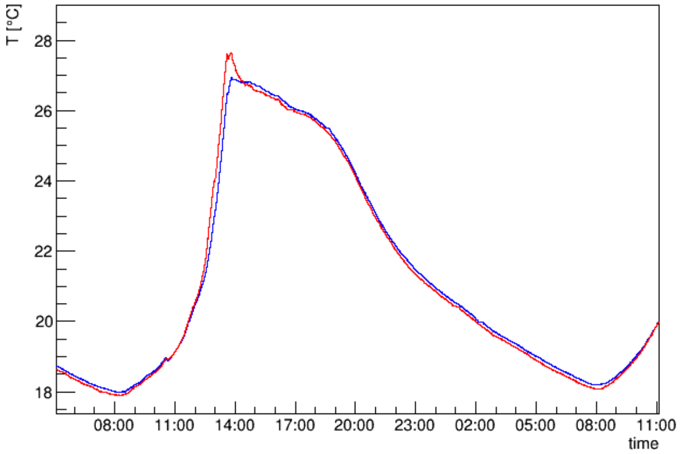

FIGURE III.5 – Temperature of the gas mixture at the entrance (blue) and at the exit (red) of the detector.

increases (*i.e.* the voltage), so if $S(t_i) > S_T$, $U(t_{i+1})$ must be less than $U(t_i)$. This parameter can be tweaked as a function of the operation conditions, in particular with respect to the speed at which the temperature and pressure changes. This is how the triggering detectors were stabilized for the experiment described in this section. Using the same setup, the operation stability was measured with this amplitude feedback method. The results are shown in Figure III.6, the first points correspond to the transition between the starting voltage and the nominal voltage for the (T, P) conditions. After this temporary regime, the signal amplitude variations induced by the (T, P) variations are less than $150\,\mathrm{ADC}$.

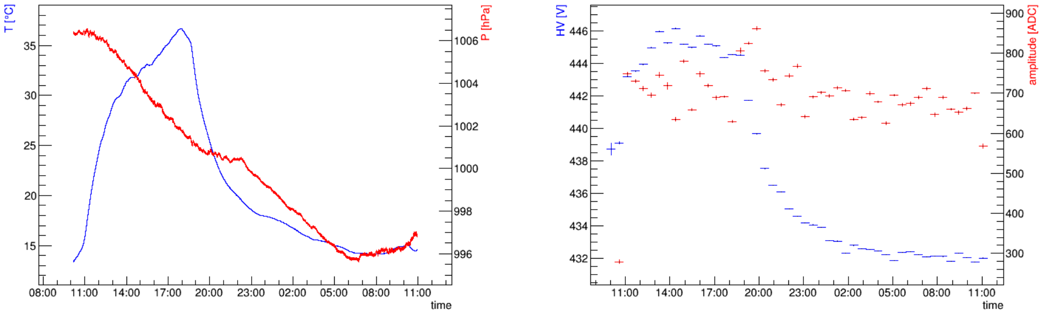

(a) Variations of (T, P) (b) Variations of the signal amplitude and U

FIGURE III.6 – Variations of the signal amplitude while using a feedback on the high voltage every five minutes. Measured with $a_S = -8\,\mathrm{mV/ADC}$, using a second version MultiGen flushed with an Ar-CF_4-iC_4H_{10} 95:3:2 gas mixture.

Using this method, the stable operation of Micromegas is possible even in environments with large temperature and pressure variations such as the Giza plateau as described in section IV.E.

III.E Gas quality and stability

Improving the operation of a Micromegas-based instrument in the wild essentially consists in improving its stability and its autonomy. Addressing the gas tightness problem is helping both of these issues. Indeed, if the gas does not leak, it means the flushing flow rate can be lowered so with a given supply (*e.g.* a gas bottle), the instrument can be operated for a longer time. Moreover, with fewer leaks, the contamination by the air surrounding the detector decreases. Because air contains a lot of Oxygen atoms (O_2 and water), which are prone to electron attachment, it disturbs the proper working of the detector. However, ensuring the tightness is not enough to maintain the quality of the gas over time. Indeed, the outgassing of the materials composing the detectors will induce a pollution of the nominal mixture by potentially releasing electronegative compounds.

To ensure the gas tightness of the detector, seals are present between each parts. There is a $2.5\,\mathrm{mm}$ depth and $3.4\,\mathrm{mm}$ width seal groove on both sides of the aluminum frame to prevent leaks in the separation between the frame and the cathode PCB on one side and the frame and the Micromegas PCB on the other. In each of these grooves sits a 20 Shores[1] silicone seal of $3.2\,\mathrm{mm}$ diameter.

At first, to measure the leaks, two calibrated flow meters can be used: one measuring the input flow and the other the output flow. While flushing the gas through the detector, the difference measured by each flow meter corresponds to the leak flow. Using this method, the minimum measurable leaks have a flow down to a few tenth of Lh^{-1} which corresponds to the flow meters accuracy. Another method can be used to measure lower leaks. An over pressure of a few tenth of hPa can be established inside the detector. By measuring the evolution of the pressure, the leak flow can be inferred. Following the law of perfect gases, the amount of gas inside the system is:

$$n = \frac{PV}{RT} \tag{III.18}$$

where P is the pressure, V the system volume, R the perfect gas constant and T the temperature. The only way n can change is through leaks:

$$n(t + \mathrm{d}t) = n(t) - \mathrm{d}n_{leak}(t) \tag{III.19}$$

However, to compare with the previous method with flushing flow, the leak has to be expressed in terms of its volumetric flow Q_V:

$$Q_V\,\mathrm{d}t = \mathrm{d}V_{leak} = \frac{RT}{P_a}\,\mathrm{d}n_{leak} \tag{III.20}$$

Where P_a is the atmospheric pressure. Therefore, if the volume is considered constant the leak flow can be expressed as:

$$Q_V(t) = \frac{T(t)V}{P_a(t)\,\mathrm{d}t}\left(\frac{P(t)}{T(t)} - \frac{P(t+\mathrm{d}t)}{T(t+\mathrm{d}t)}\right) \tag{III.21}$$

Which is equivalent to:

$$Q_V = \frac{PV}{P_a}\left(\frac{1}{T}\frac{\partial T}{\partial t} - \frac{1}{P}\frac{\partial P}{\partial t}\right) \tag{III.22}$$

---

[1] A Shore is a unit of hardness defined by Albert Ferdinand Shore.

To approximate the derivative, the difference between two successive measurements can be used. For short measurements, P_a and T can be considered as constant. An average leak can then be computed:

$$\widetilde{Q}_V = \frac{V(P(t+\Delta t) - P(t))}{P_a \Delta t} \tag{III.23}$$

However, while measuring leaks below a few $\mathrm{mLh^{-1}}$ ($\sim \mathrm{mm^3s^{-1}}$), the volume variations cannot be neglected anymore. Indeed, the thermal dilatation of the material and its rigidity induce variations of the volume with respect to T and $\Delta P = P - P_a$:

$$V = V(\Delta P, T) \tag{III.24}$$

If $\alpha_{V,P} = \frac{1}{V}\frac{\partial V}{\partial \Delta P}$ and $\alpha_{V,T} = \frac{1}{V}\frac{\partial V}{\partial T}$ are known, then the leak flow can be calculated by measuring P, T and P_a:

$$Q_V = \frac{PV}{P_a}\left(\left(\frac{1}{P} + \alpha_{V,P}\right)\frac{\partial P}{\partial t} + \left(\alpha_{V,T} - \frac{1}{T}\right)\frac{\partial T}{\partial t} - \alpha_{V,P}\frac{\partial P_a}{\partial t}\right) \tag{III.25}$$

When leak flows allow for sealed operation for a few days, the stability can still be degraded by effects on the gas mixture like the outgassing of materials that can release quenching or electronegative molecules. In order to get rid of these polluting species, the gas can be circulated through a filtering capsule as it was done for the HARPO TPC [45].

The tightness of each part of the gas circuit was measured independently: the (T, P) probe boxes, the circulating turbine with the filtering capsule and the detectors. The setup schematic is shown in Figure III.7 and the results are compiled in Table III.3.

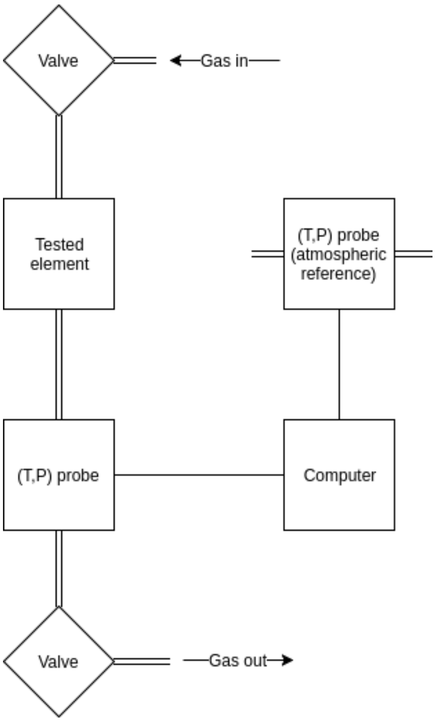

FIGURE III.7 – Schematics of the experimental setup used to measure the leak flows.

component	$\mathbf{Q_V}[\mathrm{mLh}^{-1}]$
(T, P) probe	< 1
turbine + capsule	~ 1
detector	1 to 10

TABLE III.3 – Leak flow of the different gas circuit components.

The leak flows of the probes themselves are so low that no proper measurement can be made without an estimation of $\alpha_{V,T}$ or outside of a T controlled environment. Concerning the turbine and the capsule, leak flows have been significantly reduced but the effects of the filter material can explain part of the remaining leak. Concerning the detectors, they leak a lot more but the boundary surface is bigger: the total length of seal ($\sim 2\,\mathrm{m}$) is 12 times higher than the one of the probe casings. Moreover, the front and back surfaces of the detector are made of PCB which is known as a porous material. Gluing both PCBs to the aluminum frame has been done recently, it improves the gas tightness but any maintenance operation such as cleaning becomes complicated.

III.F Enhanced demultiplexing

Depending on the acquisition conditions, about 10% of the reconstructed events are multiple events *i.e.* two or more muons cross the telescope at the same time. Because of the large multiplexing of the MultiGen detectors, some ambiguities can then arise. After the failure of addressing the resolution issue with methods from the literature such as the one described in [46], other ways to solve these problems have been developed.

III.F.1 Association and clustering issue

The association between hit channel and hit position inside the detector is trivial for most of the detectors but with MultiGen, the association is made at the level of the multiplets. If k channels are considered as carrying a signal, one needs to check if k contiguous strips are wired to these k channels. If found, then the position of the crossing particle is reconstructed, if not, the search then focuses on the k $\{k-1\}$-uplets and so on until a contiguous set of strips is found. If n particles cross the detector at the same time, each firing k_i channels, the maximum sized uplet that can be found is of size k_{tot}:

$$k_{tot} = \sum_{i=0}^{n-1} k_i \tag{III.26}$$

Every multiplet of size between $\max(k_i)$ and k_{tot} does not correspond to any physical event and will lead to a misplaced cluster. Another problem that can occur is non-contiguous signal. Indeed, if a strip is connected to a faulty channel or the strip is cut, the signal induced on this channel may not be high enough to pass the threshold. When such a strip corresponds to the edge of the cluster (where the signal is fainter), it just induces a slight error on the cluster position but if it is inside the cluster it will divide it in two non-contiguous parts of total size $k-1$. However, the demultiplexing will still search for the biggest cluster and will try to find a $k-1$ wide cluster or a cluster wider than each of the two non-contiguous parts. This effect is likely to end with a cluster placed elsewhere inside the detector. Another source of non-contiguous signal is the randomness of ionization inside the drift volume. As seen in section II.A.2.a, the primary electrons are created by the ionization of the gas by the crossing particle. The randomness of this process can lead to large distances between two successive ionizations in particular with large angle tracks. The signal induced in the detector will then be intrinsically non-contiguous. This last effect grows with the track angle, the conversion gap width and decreases with the transverse diffusion during the drifting process. Indeed, when some energy is transferred to the gas by the incoming particle, several ionization electrons are produced. If the transverse diffusion is negligible (with respect to the strip pitch), the signal induced by these primary electrons will not likely overlap with others coming from farther ionizations.

This problem is not specific to multiplexed Micromegas. GEANT4 simulations with the cosmic muon flux given by the CRY generator [47] and a $1.5\,\mathrm{cm}$ drift gap Micromegas with a granularity of $482\,\mu\mathrm{m}$ have been made for various transverse diffusions corresponding to different gas mixtures. Muons generated by CRY are propagated through the detector by GEANT4, giving the deposited ionization energy and the path inside the detector. This information is also given for secondary particles generated by GEANT4 during the propagation process *e.g.* δ electrons. Given these data, interaction positions are generated uniformly on the muon path inside the conversion volume. For each position, the number of primary electrons generated follows a Poisson distribution of parameter the number of ionizations per interaction N_e. This number is the ratio of the total number of primary electrons created by unit length N_t and the number of ionization collisions by unit length N_p. The values given by [48] lead to *e.g.* $N_e = 4.1$ for Argon. The strip on which each primary electron will cause signal is then calculated taking into account the transverse diffusion. The position is shifted by a length following a Gaussian distribution of zero mean and of standard deviation given by the transverse diffusion coefficient of the gas and the square root of the height at which the electron is generated with respect to the micromesh. The signal strength is then calculated using a Polya distribution to take into account the Townsend avalanche. New interactions are generated until the deposited ionization energy corresponds to the total number of generated primary electrons times the average energy needed to create an electron-ion pair w_i. This simulation shows the influence of the track angle and the transverse diffusion on the resolution of the track position in Figure III.8. For normal tracks, if the transverse diffusion is lower than the strip pitch, then every primary electron essentially cause signal on the same strip at the position of the track but for larger transverse diffusion, the signal is spread over more neighboring strips, worsening the resolution. However, for larger track angles, with a small transverse diffusion, the signal spreading is not sufficient to maintain the contiguity of the signal so the cluster is split in multiple parts. Each of these parts carries only a fraction of the total charge so the reconstructed position is shifted. This way, when the track angle grows, the resolution using large transverse diffusion gas is better.

At first glance, allowing the clustering algorithm to jump some strips without signal seems a good solution. This same simulation shows that in noise-less simulation, the resolution improves especially for large track angles as shown in Figure III.9. Introducing holes (signal-less strips) during the clustering process helps to lower down the resolution at high track angles. The benefits of this method appear at even lower track angles for lower transverse diffusion.

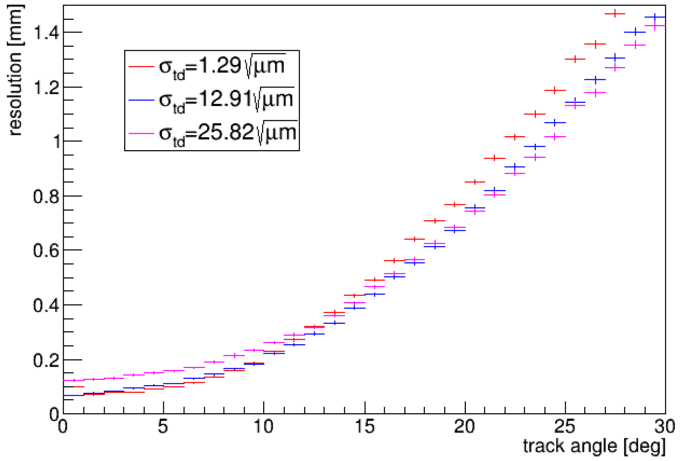

FIGURE III.8 – Simulated resolution in function of the track angle for three values of the transverse diffusion.

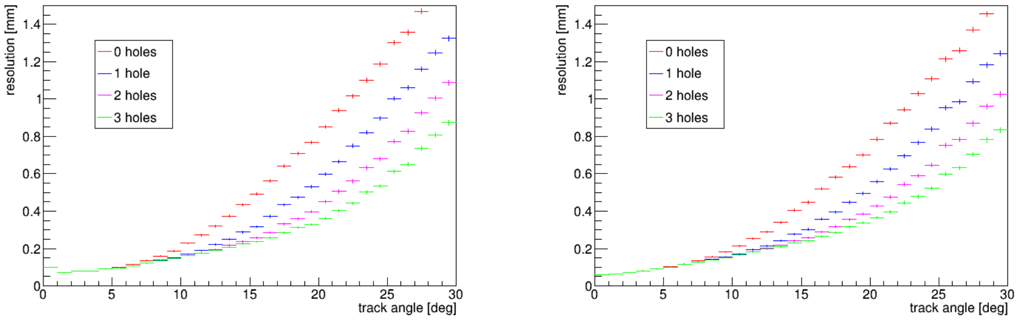

(a) $\sigma_{td} = 1.29\ \sqrt{\mu\text{m}}$ (b) $\sigma_{td} = 12.91\ \sqrt{\mu\text{m}}$

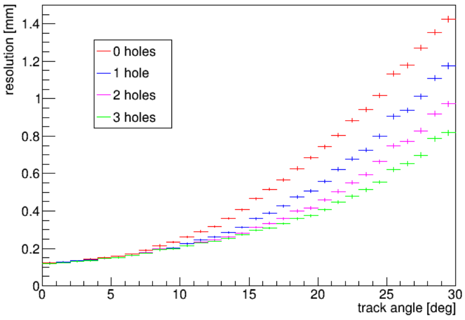

(c) $\sigma_{td} = 25.82\ \sqrt{\mu\text{m}}$

FIGURE III.9 – Simulated resolution in function of the track angle for different clustering algorithms allowing jumps for three transverse diffusions.

However, because of the noise, some strips can be misidentified as carrying a signal. Introducing holes in the algorithm can then include these noisy strips inside a cluster. Doing so will shift again the cluster position and degrade the resolution.

The influence of the angle track is a purely geometrical effect, the signal is spread over more and more strips as the track angle increases so if the distance between two ionizations remains constant, this distance projected on the readout plane also increases. If the transverse diffusion is negligible with respect to the strip size, non-contiguity will arise if the projected distance becomes larger than roughly two times the pitch. Moreover, the length between two successive ionization follows an exponential law, so it is possible to compute the rate R at which this distance is above the two times the pitch limit:

$$R = exp\left(-\frac{2l_0}{\lambda_{ion}\sin(\theta_{track})}\right) \tag{III.27}$$

where l_0 is the pitch, λ_{ion} is the mean free path between two ionizations and θ_{track} the angle of the track. For argon, this rate can go up to $11\,\%$. Because several primary electrons are created at each ionization point, the transverse diffusion will counterbalance this effect. Indeed, the signal from a single ionization point will be spread according to the diffusion and the distance between the ionization and the mesh. This spreading reduces the average distance between the signal coming from two different ionization points.

This effect is enhanced by the multiplexing as shown in Figure III.10 even if there is only low statistics at very large angles. Along with the failure to fulfill the demultiplexing requirements by having a disjoint signal, if the cluster size exceed 17, the association of the set of channels with a set of contiguous strips is not unique anymore.

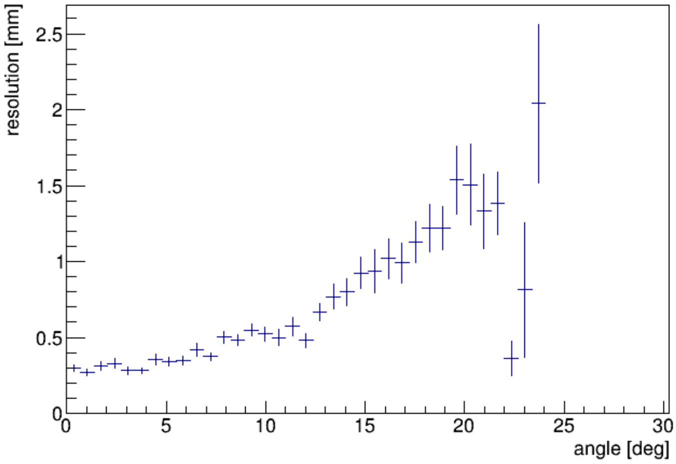

FIGURE III.10 – Second version MultiGen position resolution with respect to the track angle.

To reduce the error on the cluster position, these problems need to be addressed by enhancing the demultiplexing process. One way to do this is to take more information into account. Since the aim is to track muons crossing the whole system through straight lines, it will lead to aligned hits inside the detectors. This property can be used to enhance the tracking.

The current way to perform the track reconstruction from channel to channel signal is to first run a demultiplexing coupled with a clustering algorithm. It will search for the biggest set of contiguous strips which carry a significant signal *i.e.* of amplitude 4σ above the noise level. When such a set is found a cluster is made and stored. The channels used to make the cluster are discarded and the search is run again until there is no channel carrying signal anymore. The position of the cluster is then the barycenter of the position of the strips weighted by their amplitude. To get the absolute position, an offset corresponding to the position and the angle of the detector with respect to the cosmic bench is applied. Then a track finding and fitting algorithm is run independently in both measured coordinates. For one coordinate, some quality cuts are made on the clusters. If there is at least one cluster remaining in at least three detection planes then a track can be found. All the possible combinations of clusters taken out from different detection planes are tested in order to make a track. The one with the lowest χ^2 is kept, the clusters used to build it are discarded and the track finding is run again until no combinations of clusters can be made. Then some quality cut can be applied to the set of tracks *e.g.* a χ^2 threshold. So this technique is able to reconstruct multiple muons events but the correct correlation between the x and y clusters in each detector is not guaranteed.

III.F.2 Reprocessing approach

A simple idea to solve the problem of non-hit strips inside a cluster is to give the information about the track angle before doing the demultiplexing because the main factor is the transversal length traveled by the muon inside the drift gap. A first crude demultiplexing can be done in order to do a first processing giving an approximate track angle. Then a finer demultiplexing is made using this information by grouping nearby clusters. The distance between two clusters that can be grouped is determined by the angle: if the track angle is close to the normal of the detector plane, no grouping is done, whereas if it is large, grouping between more and more distant clusters is allowed. This way the charge barycenter is corrected to give a more accurate position. At the end, a final processing is done to extract the track parameters. The clustering algorithms allowing holes (described in the previous section) can be used while the effect of noisy strips is tempered because the allowed hole number is dependent to the track angle. Strips which can be tagged as noisy through a whole run can also be listed and explicitly ignored by the tracking algorithm.

III.F.3 Hough transform approach

The basic idea of the Hough transform is to associate for each point of the position space every line that crosses that point [49]. Each point is then projected to a curve *e.g.* a line or a sinusoid. The projections of two points will then intersect, allowing the identification of the unique line defined by these two points *e.g.* its slope and intercept. For multiple points, one can then verify if they are aligned by checking if their Hough projections intersect. For our particular use, the specificities of the detectors make it easier to split the tracking in two 2D trackings: one in the xz-plane and the other in the yz one. To make a parametrization of the Hough space, since all possible 3D lines do not correspond to a physical track, we restrain the Hough space to the lines that cross the planes defined by the most upstream and the most downstream detectors. The two crossing points defining a unique straight line, we can use them as the Hough parameters. So each (x, y, z) hit will lead to a set of $((x_{top}, x_{bot}), (y_{top}, y_{bot}))$ corresponding to the location where the lines passing by (x, y, z) cross the $z = z_{bot}$ and $z = z_{top}$ planes. The relation between the position space and the Hough space coordinates are given by:

$$(x_{bot} - x)(z_{top} - z) = (x_{top} - x)(z_{bot} - z) \tag{III.28}$$

$$(y_{bot} - y)(z_{top} - z) = (y_{top} - y)(z_{bot} - z) \tag{III.29}$$

This way, Hough curves are straight lines with the wider possible crossing angle which will simplify the recognition of these crossings. Instead of only searching for the wider k-uplet of contiguous hit strips, all these contiguous uplets where $k \geq 2$ (*i.e.* those that have an unambiguous position) can be listed. Using the Hough transform, the clusters likely to represent a muon track can be identified even if there are more than one of them by searching for aligned clusters. Since there is an error on the measured position, no more than two Hough curves can perfectly cross each other. The standard method is to divide the Hough space into bins, each curve adding one into the bin it crosses and then search for the maximum bin. However, this method is largely dependent of the bin size. The Hough curve being straight lines, clusters from n detectors will form an n-gon which will reduce to a single point in the perfect case. To evaluate the distance to the perfect case, the area of this polygon can be used. But computing the area $\mathcal{A}$ of a complex polygon which is not convex in most of the cases is not easy. An upper limit is enough and can be given by a length scale d_{max} such as.

$$\mathcal{A} < d_{max}^2 \tag{III.30}$$

To compute this scale, the distance between a vertex $V \in \mathcal{V}$ and an edge $L \in \mathcal{L}$ of the n-gon $d(V, L)$ can be considered. Let $\mathcal{L}_V^*$ be the set of all edges but the ones intersecting at V:

$$\mathcal{L}_V^* = \{L \in \mathcal{L} \mid d(V, L) \neq 0\} \tag{III.31}$$

A suitable length scale d_{max} can then be computed as:

$$d_{max} = \max_{V \in \mathcal{V}} \min_{L \in \mathcal{L}_V^*} d(V, L) \tag{III.32}$$

Finding the n-gon with the smallest d_{max} is finding the most well aligned set of clusters, corresponding to a physical track. An example of a track candidate in Hough space is shown in Figure III.11 together with the track candidate computed by the standard algorithm. In some cases both track candidates are the same but for other cases they can be significantly different.

To apply this method to the MultiGen demultiplexing, strips can be scanned for every contiguous cluster of any size greater than two inside the detector. Since all detector planes are parallel, all the clusters coming from a single detector will transform to parallel lines in the Hough space. The d_{max} is then computed for each track candidate. The ones below a threshold $d_{max,thr}$ are selected. At this point, for each event, the number of tracks is known along with crude information about their trajectories, in other word, crude information about where the muons crossed the several detectors. With this knowledge, a fine clustering can be made. Like before, holes can be introduced regarding the track angle. Moreover, the information about the number of tracks can be used to avoid grouping channels that bear signal corresponding to different tracks.

III.G Alignment of the detectors

As mentioned in section III.F.1, to be able to reconstruct the tracks with the highest possible precision, the relative position and angle of the detectors have to be known. Indeed, the detectors can measure the position where a muon passed to a fraction of

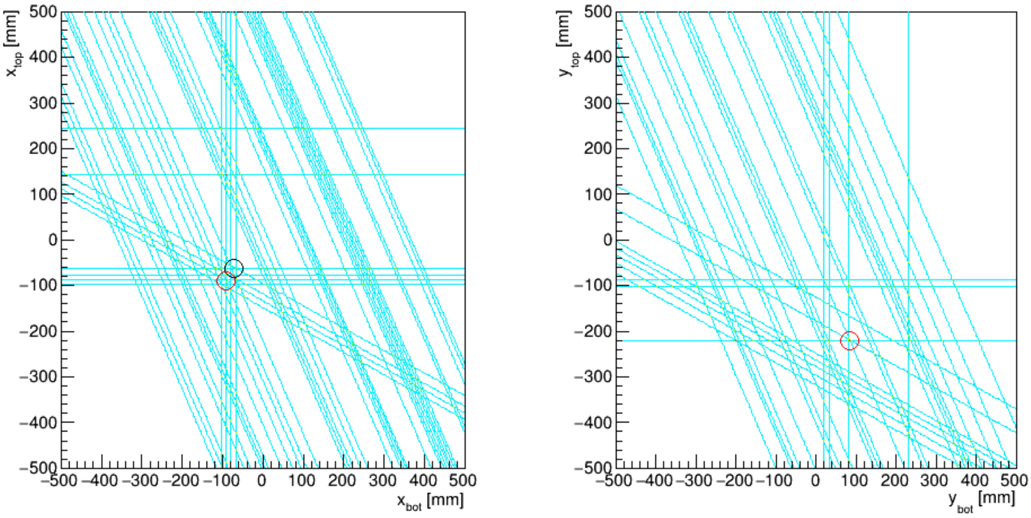

(a) x coordinate projection.

(b) y coordinate projection, the red and black circles are superimposed.

FIGURE III.11 – Hough space visualization for a typical event measured by four stacked MultiGen detectors, the red circle is the best track candidate computed using the Hough transform compared to the black one which corresponds to the standard tracking algorithm.

mm but the relative position of the detectors cannot be measured to that precision. Using an approximate positioning of the detectors, it is possible to refine it using the muon tracks themselves. By setting the two extreme detectors as references *i.e.* their position is supposed to be perfectly known, the straight tracks of muon reconstructed by these detectors can be used to align the others. Actually, the muon track position can be extrapolated on the plane of other detectors and compared with the measured position. Considering a detector measuring the x coordinate, if the distribution of the residual (the difference between the extrapolated and the measured one) have non-zero mean, it means that the detector position has to be shifted by this mean. To correct the position with respect to the axis perpendicular to the detector plane z, the dependence of the residual with the track angle in the xz-plane can be used. If the detector is above its considered position, the residual will increase with the track angle as shown in Figure III.12. Indeed, the mean residual $\bar{\Delta x}$ in function of the track angle θ_x can be expressed as:

$$\bar{\Delta x}(\theta_x) = \Delta z \tan(\theta_x) \tag{III.33}$$

where Δz is the misalignment along the z axis.

When the translation alignment has been made, the rotation alignment can be done. The angle within the detector plane can be determined using the dependence of the mean residual $\bar{\Delta x}$ to the measured position along the strip direction because $\bar{\Delta x}(y) = \tan(\alpha_z)y$ where y is the extrapolated position and α_z is the detector angle as shown in Figure III.13.

The effects of the two remaining angles are more complex and one has to be careful because even if this alignment corresponds to three rotations around perpendicular axes, they do not commute so the set of $(\alpha_x, \alpha_y, \alpha_z)$ will be different for each order.

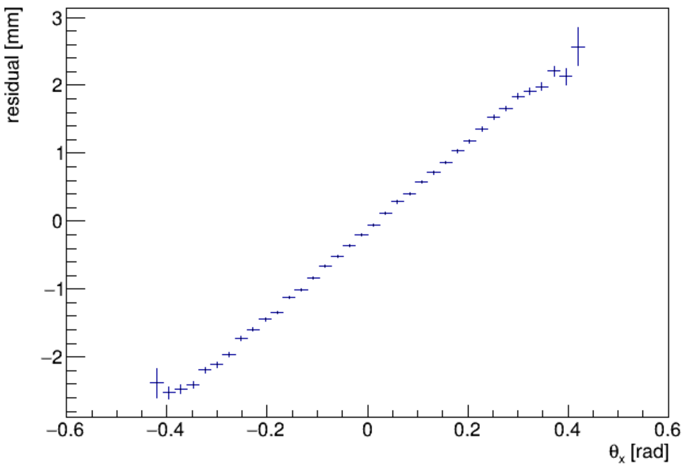

FIGURE III.12 – Mean residual with respect to the reconstructed track angle for a detector considered $5\,\mathrm{mm}$ above its true position.

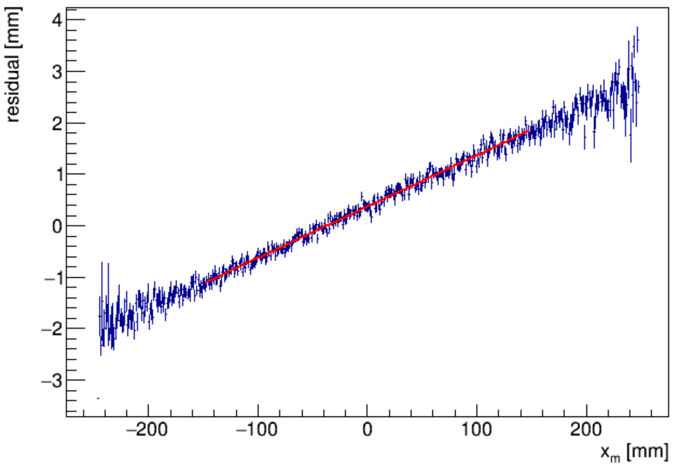

FIGURE III.13 – Mean residual with respect to the coordinate perpendicular to the measured one for a detector rotated by $\alpha_z = 10\,\mathrm{mrad}$.

The rotation around the strip axis can be measured using the correlation between the residual and the position measured by the strip while the last rotation can be measured using the correlation between the residual and the track angle in the yz-plane. However, at low track angles the misalignments α_x and α_y have a negligible effect compared to the four other parameters.

Chapter IV

Absorption Muography

IV.A Principle

As developed in section I.C.1, muons crossing matter lose energy and thus can be stopped. This stopping power will result in a decrease of flux ϕ beneath the matter. In other terms, matter creates a muon shadow. By measuring the flux coming through open sky and/or through matter, a muon deficit can be computed and will give information on matter density. This idea was tested for the first time by George to measure the depth of a tunnel [50].

IV.A.1 Opacity measurement

As shown by Equation I.8, muons lose energy the further they travel through matter and the denser the material is. Indeed, the radiative term is mostly constant but the Bethe term described in Equation I.9, shows a first order dependency in $\frac{Z}{A}$. However, since we want to image solid structures, it can be shown that this ratio is not varying significantly and $\frac{Z}{A} \approx 0.5$.

The effect of matter is present all along the muon path, for a given direction the absorption factor will depend both on the density and the length of crossed matter so it is convenient to introduce the opacity ϱ:

$$\varrho = \int_D \rho \, \mathrm{d}s \tag{IV.1}$$

Where D is the muon path. The stopping power of Equation I.8 can then be written as:

$$-\frac{\mathrm{d}E}{\mathrm{d}\varrho} = B + RE \tag{IV.2}$$

If the Bethe term B and the radiative term R are considered as constants, the minimum energy E_{min} needed to cross a given opacity ϱ can be deduced:

$$E_{min} = \frac{B}{R}\left(e^{R\varrho} - 1\right) \tag{IV.3}$$

We can then define the survival probability $\mathbb{P}(E, \varrho)$ of a muon of initial energy E crossing a volume of matter of opacity ϱ. A crude approximation will be to consider:

$$\mathbb{P}(E, \varrho) = \mathrm{H}(E - E_{min}) \tag{IV.4}$$

Where H is the Heaviside function. But since the energy loss processes are discrete, E_{min} just indicates at which point the probability changes from near 0 to near 1. Considering that muons travel on straight lines, knowing the open sky flux Φ (discussed in section I.B.1) the muon flux ϕ below a massive object can be deduced:

$$\phi(\theta, \varphi, E) = \int \Phi(\theta, \varphi, E)\mathbb{P}(E, \varrho)\,\mathrm{d}E \tag{IV.5}$$

By comparing the two fluxes, it becomes possible to deduce $\varrho(\theta, \varphi)$.

However, when measuring the fluxes with an actual instrument, its geometry and intrinsic characteristics will affect the measurement. To take this effect into account we have to introduce the acceptance factor $\mathcal{E}$ which is the probability for a muon coming from the direction (θ, φ) to be actually detected. The measured flux ϕ_m can then be expressed as:

$$\phi_m(\theta, \varphi) = \mathcal{E}(\theta, \varphi) \int \Phi(\theta, \varphi, E)\mathbb{P}(E, \varrho)\,\mathrm{d}E \tag{IV.6}$$

One way to get rid of this experimental factor and reduce systematic errors is to measure an open-sky flux Φ_m and to compare both measured fluxes.

$$\Phi_m(\theta, \varphi) = \mathcal{E}(\theta, \varphi) \int \Phi(\theta, \varphi, E)\,\mathrm{d}E \tag{IV.7}$$

During an actual experiment, the flux is not measured directly. The observable is the number of muons in each direction $\mathrm{d}N_\mu\,(\theta, \varphi)$:

$$\mathrm{d}N_\mu\,(\theta, \varphi) = \Delta t \mathcal{A} \phi_m(\theta, \varphi) \tag{IV.8}$$

where Δt is the time of exposure and $\mathcal{A}$ is the surface of the muon collecting area. Since the time of arrival of a single muon is random with a mean frequency determined by the flux, $\mathrm{d}N_\mu\,(\theta, \varphi)$ then follows a Poisson distribution and the error on the measure $\sigma_{\mathrm{d}N_\mu}$ is:

$$\sigma_{\mathrm{d}N_\mu} = \sqrt{\mathrm{d}N_\mu} \tag{IV.9}$$

The relative error on the flux $\frac{\sigma_\phi}{\phi}$ is then:

$$\frac{\sigma_\phi}{\phi} = (\Delta t \mathcal{A} \phi \mathcal{E})^{-\frac{1}{2}} \tag{IV.10}$$

As seen in section I.B.1, the average open sky muon flux is quite low and depends on the zenith angle so the collection area and the time of exposure have to be correctly estimated to be sensitive to a certain opacity contrast at a given line of sight elevation.

At this point several methods exist to extract the desired information. On one hand, the measured flux can be compared to a simulated expected flux to pinpoint discrepancies. This method is useful in cavity search or when the anomalies that are looked for have a high enough contrast. On the other hand, the problem can be inverted in order to extract the opacity or an average density $\bar{\rho}$ along a line of sight:

$$\bar{\rho}(\theta, \varphi) = \frac{\varrho}{L} = \frac{\int_D \rho\,\mathrm{d}s}{\int_D \mathrm{d}s} \tag{IV.11}$$

The second method is more accurate and gives actual characteristics of the imaged object but is much more complex to set up.

IV.A.2 Application

Absorption muography is a technique constrained by two factors: the muon flux and the muon absorption probability. The source of contrast in the measured flux is the contrast in opacity that can be intensified by the time of acquisition and surface of detection. Rock imaging suits this requirement, time constants involved are sufficiently big to produce a contrasted image. Moreover, void research or mineral veins provide large enough opacity differences to be measured by muon absorption.

The main domain in which rock imaging is useful and accessible through muon tomography is volcanology. Initiated by Japan using nuclear emulsions in, for example, Mont Asama [51], the technique spread around the world. In particular in Italy where INFN and INGV collaborate to image volcanoes *e.g.* the Vesuvius [52] with scintillator and nuclear emulsion based telescopes. The collaboration between particle physicists and volcanologists was also successful in France with the DIAPHANE collaboration using scintillators to image the active Soufrière of Guadeloupe [53, 54] and the TomuVol project imaging the inactive Puy de Dôme [55] with resistive plate chambers.

Large archaeological structures can also be muographed like it has been done in Mexico with the scan of the pyramid of the Sun [56] employing MWPC detectors. In Europe, the scan of an Ancient Greek tomb is also planned [57].

The technique is also actively developed for geological imaging in general and in particular for mining prospection to detect dense material deposits [58].

IV.B Proof of concept

A very first simple experiment was made to demonstrate the capability of muography to measure opacity.

IV.B.1 Experiment

A setup of two $60 \times 60\ \mathrm{cm}^2$ plastic scintillators with photomultiplier tubes and a coincidence module was used to count the muons. A first $7\,\mathrm{h}$ long measurement was made outside. It corresponds to an open-sky measurement. During this data taking, the measured muon rate was: $(6.40{\pm}0.02)\ \mathrm{Hz}$. Then a second $7\,\mathrm{h}$ long measurement was made inside, below the concrete roof of the laboratory. This roof absorbs muons, thus reducing the muon flux reaching the instrument. Indeed, a muon rate of $(6.25{\pm}0.02)\ \mathrm{Hz}$ was measured, the absorption factor is then $(2.3{\pm}0.4)\ \%$.

IV.B.2 Simulation

The experimental protocol was simulated using the CRY engine to generate cosmic muons [47] and GEANT4 to propagate them through the concrete roof and the scintillating detectors. Using these tools, the simulated counting rate between several roof thicknesses and the experimental one can be compared. The result of these simulations is shown together with the data in Figure IV.1.

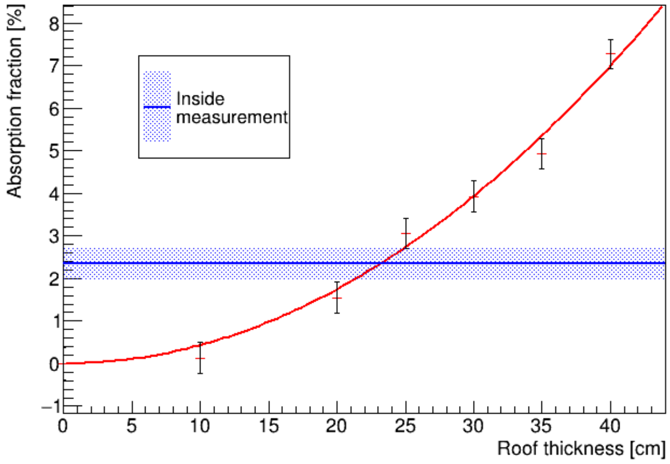

FIGURE IV.1 – Simulated absorption fraction for different concrete roof thicknesses.

IV.B.3 Result

The density of the roof can be inferred using its composition. The only unknown left is the roof thickness that can be estimated by comparing the data and the simulation. An estimate of the actual roof thickness then leads to $(23{\pm}2)\,\mathrm{cm}$. The remaining source of uncertainty is the actual composition of the roof and the particle spectra generated by the CRY engine. For the simulation a standard concrete of $\rho = 2.3\,\mathrm{g\,cm^{-3}}$ was used, whose composition is shown in Table IV.1, but some metallic reinforcement can be present.

Element	**mass fraction**
O	0.605 41
Si	0.227 915
H	0.099 72
Ca	0.049 86
Al	0.014 245
Fe	0.002 85

TABLE IV.1 – Composition of the simulated concrete.

IV.C First Saclay muographies

When the first detectors were fully operational, first muography tests were conducted inside, using the cosmic bench at Saclay laboratory in Spring 2014.

IV.C.1 Overview

In order to test detectors made for high energy physics, a cosmic bench is used. This test bench is instrumented with MultiGen detectors described in section II.D.

At the top of it, an aluminum table is available to support objects to be imaged. Patterns have been made using $10 \times 10 \times 5\ \mathrm{cm}^3$ lead bricks. This enabled us to image different thicknesses and patterns to test the imaging resolution and detail separation capabilities.

IV.C.2 Experimental setup

The Saclay cosmic test bench is an aluminum frame in which four first version MultiGen detectors are placed. They are disposed in two doublets. The level arm between the detectors can be adapted but the distance between the doublets is typically $1\,\mathrm{m}$ and the distance between the two detectors of a doublet is typically $11\,\mathrm{cm}$.

They were flushed with a Ar-iC$_4$H$_{10}$ mixture in $90{:}10$ proportion. The gas passed successively in both detectors of a doublet but each doublet was flushed in parallel with a volumetric flow of $Q_V = 2\,\mathrm{Lh}^{-1}$.

The trigger is provided by two $60 \times 60\ \mathrm{cm}^2$ plastic scintillators. The bottom one is placed approximately $11\,\mathrm{cm}$ below the lowest Micromegas and the top one at approximately the same distance above the upper detector. The disposition of the cosmic bench after the alignment procedure is summed up in Table IV.2.

Element	**altitude** [mm]
Al table	$\sim$1550
Scintillator 1	$\sim$1370
MG 3	1277.9
MG 2	1161.5
MG 1	115.65
MG 0	0
Scintillator 0	~ -110

TABLE IV.2 – Cosmic test bench composition and positioning.

A NIM analog coincidence module uses both scintillator signals to build a trigger which is sent to the FEU readout electronics. For muons, the efficiency of the triggering system is near 100% and its acceptance is larger than the Micromegas telescope if at least three hits are required to correctly identify a muon. This way, the number of muons crossing the bench which are not recorded are negligible but some muons induce a trigger without being in the acceptance of the Micromegas. The cosmic bench is shown in Figure IV.2

To reconstruct the muon tracks, a simple tracking is made. Since the MultiGen detectors measure the x and y coordinates independently, two 2D tracking are made: one in the xz-plane and the other in the yz-plane. The result is then merged to reconstruct the full 3D track.

For this experiment, the lead bricks to be scanned have been put on the aluminum table.

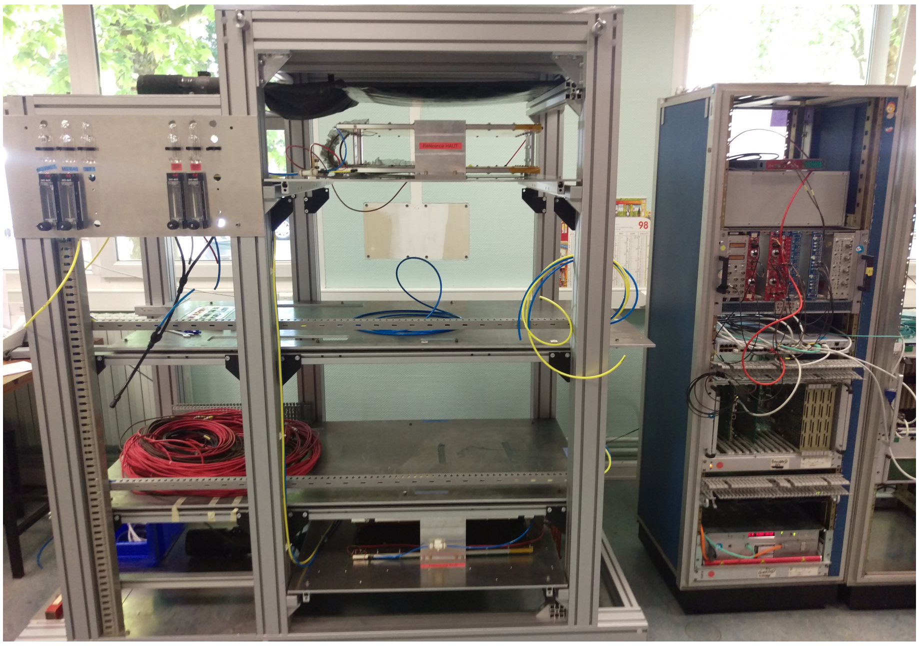

FIGURE IV.2 – Cosmic bench using four MultiGen detectors, two triggering scintillators, the gas system at the left and the triggering logic and acquisition electronics at the right.

IV.C.3 Data analysis

Since the imaged object is very close to the detector, expressing only the flux in term of the θ and φ angles will not take any parallax effect into account. Then the muon position can be extrapolated at the imaging plane $\mathcal{P}$ to plot the flux crossing this plane. Calculations are simplified because $\mathcal{P}$ is perpendicular to the bench axis.

$$\mathcal{P} : z = z_I \tag{IV.12}$$

$$\phi_{m,z_I}(x, y) = \frac{N(x, y, z_I)}{\Delta t \mathcal{A}} \tag{IV.13}$$

where $N(x, y, z)$ is the number of measured muons that passed by (x, y, z) location.

To take into account the acceptance effect and the muon flux anisotropy, two methods are possible. The first one is to have two sets of data in the same conditions: one with the object to be imaged and one without. Comparing the two sets will cancel out these effects. The other one is to compute an expected $\phi_{th,z_I}(x, y)$ by estimating these effects. Indeed, as seen in section I.B.1, the muon flux can be approximated with a $\cos^2(\theta)$ distribution and the acceptance effect is a geometrical effect. The probability for a muon having a zenith angle θ, an azimuth angle ϕ and passing by the (x, y, z_I) point is:

$$\mathbb{P}(x, y, z_I, \theta, \varphi) = \mathbb{P}_0 \cos^2(\theta) \mathbb{1}(x, y, z_I, \theta, \varphi) \tag{IV.14}$$

where $\mathbb{1}(x, y, z_I, \theta, \varphi)$ is one when the muon path crosses the cosmic bench and 0 otherwise and $\mathbb{P}_0$ is a normalization factor such that:

$$\int_{x\in\mathbb{R}} \int_{y\in\mathbb{R}} \int_{\theta=0}^{\frac{\pi}{2}} \int_{\varphi=0}^{2\pi} \mathbb{P}(x, y, z_I, \theta, \varphi) \, \mathrm{d}x \, \mathrm{d}y \, \mathrm{d}\theta \, \mathrm{d}\varphi = 1 \tag{IV.15}$$

This function is determined by the detector size L_{det} and the position of the top and bottom most detectors. Let the detector centers be at $(x, y) = (0, 0)$ and their altitudes be respectively z_{top} and z_{bot}. The indicator function is then:

$$\begin{aligned}\mathbb{1}(x, y, z_I, \theta, \varphi) =& H\left(\frac{L_{det}}{2} - \left\|(z_I - z_{top})\tan(\theta)\begin{pmatrix}\cos(\varphi)\\ \sin(\varphi)\end{pmatrix} + \begin{pmatrix}x\\ y\end{pmatrix}\right\|_\infty\right)\\ &\times H\left(\frac{L_{det}}{2} - \left\|(z_I - z_{bot})\tan(\theta)\begin{pmatrix}\cos(\varphi)\\ \sin(\varphi)\end{pmatrix} + \begin{pmatrix}x\\ y\end{pmatrix}\right\|_\infty\right)\end{aligned} \tag{IV.16}$$

where H is the Heaviside function and $\|\cdot\|_\infty$ is the infinity norm[1].

At the end, the flux estimate is the probability integrated over the muon angular parameters:

$$\phi_{th,z_I}(x, y) = \phi_0 \int_{\theta=0}^{\frac{\pi}{2}} \int_{\varphi=0}^{2\pi} \mathbb{P}(x, y, z_I, \theta, \varphi)\,\mathrm{d}\theta\,\mathrm{d}\varphi \tag{IV.17}$$

Where ϕ_0 is a normalization factor such that:

$$\iint \phi_{th,z_I}(x, y)\,\mathrm{d}x\,\mathrm{d}y = \iint \phi_{m,z_I}(x, y)\,\mathrm{d}x\,\mathrm{d}y \tag{IV.18}$$

To compare both fluxes, a first method is to subtract one from the other: $\Delta\phi = \phi_m - \phi_{th}$. This way, it shows the muon deficit created by the imaged object and cancels out the acceptance effects. However, not only the flux differences but significant flux differences have to be pinpointed. The way to do that is to plot the difference in unit of the error σ. The observable is then:

$$\frac{\Delta\phi}{\sigma_{\Delta\phi}} = \frac{\phi_m - \phi_{th}}{\sqrt{\sigma^2_{\phi_m} + \sigma^2_{\phi_{th}}}} \tag{IV.19}$$

IV.C.4 Results

The Figure IV.3a shows the accumulated muon map $N(x, y, z_I)$ during two weeks where z_I is the altitude of the table on which lead bricks were put: $z_I = 1550\,\mathrm{mm}$. The deficit of collected muons can clearly be seen and corresponds to each of the lead brick positions. However, the outer edge of the bricks are not clearly defined due to the acceptance effect. To reduce it, the difference with a brick-less run or a theoretical estimate computed as explained before can be plotted as it is done respectively in Figure IV.3b and Figure IV.3c. This is not the flux difference but the accumulated muons difference $\Delta N = N_m - N_{th}$ which is plotted since it differs only by a $\Delta t \mathcal{A}$ factor. It flattens the image around a null mean value but it does not show any information concerning the significance of this difference. It could arise from statistical fluctuations of the number of collected muons. So the significance as defined in Equation IV.19 is shown in Figure IV.3d and Figure IV.3e.

While the four squares of significant muon deficit are created by the lead bricks, flux differences at the edges are artefacts. For the experimental subtraction (the left plots of Figure IV.3), they come from the detector position. Indeed, the signal and background

---

[1] $\left\|\begin{pmatrix}x\\ y\end{pmatrix}\right\|_\infty = \max(|x|, |y|)$.

runs could not be taken one after the other so between the two runs the detectors were moved slightly ($\sim 2\,\mathrm{mm}$) along the z direction. So the acceptance slightly changed between the two runs and most of the differences are on the sides were few muons are collected. For the theoretical subtraction (the right plots of Figure IV.3), they come from acceptance effects that are not taken into account. The model only takes into account muons that passed through the top most and bottom most detector. However, the scintillator based trigger and the tracking algorithm allows muons passing through three out of four detectors. So the true theoretical acceptance function $\mathbb{1}(x, y, z_I, \theta, \varphi)$ should take into account the altitude of the triggering scintillators and a check on whether the muon is passing through enough MultiGens.

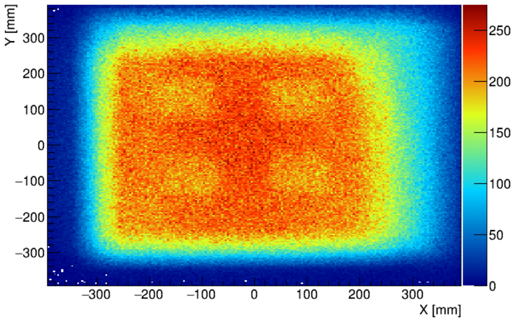

(a) Muon flux expressed in number of accumulated muons.

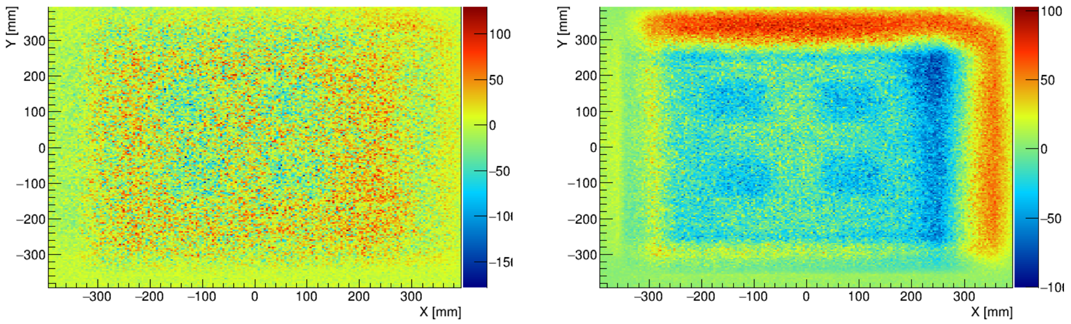

(b) Difference with lead brick-less run.

(c) Difference with theoretical flux expectation.

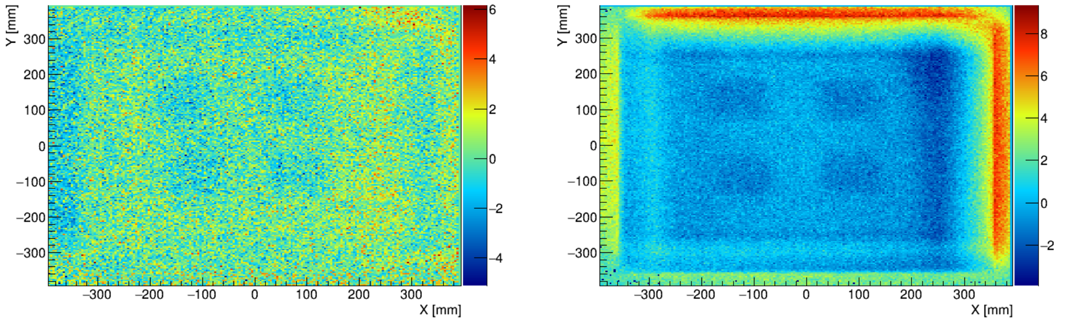

(d) Significance of the measured muon flux with respect to the brick-less run.

(e) Significance of the measured muon flux with respect to the theoretical expectation.

FIGURE IV.3 – Absorption muography of four $5\,\mathrm{cm}$ thick lead bricks.

IV.D WatTo experiment

The technique was already proven to be successful but our Micromegas setup had never been tested outside a laboratory. The behavior of the detector in a non-controlled environment had to be tested together with the static and dynamic imaging capabilities [59].

IV.D.1 Overview

Micromegas detectors work well inside a lab and are suitable to make a muon telescope but their performance in the field are not yet proven. To validate the operation of a Micromegas-based telescope a relevant object had to be chosen as a model to image.

The criteria for this validation test are:

- easy deployment
- access to network and power
- large enough to have enough flux
- with enough contrast in opacity
- with an opacity changing slowly with time

The last criterion was optional but allowed to test the dynamic imaging capabilities. The perfect candidate was the water tower of the Saclay research center. The concrete tank is a dense enough structure to be seen with muons and it is high enough to be able to image it with a telescope pointing close to the zenith to minimize acquisition time. The tank is roughly at $23\,\mathrm{m}$ height. The level of the water inside the tank is varying with time constants of the order of the day, providing a source of variation of the opacity. Last, the telescope is placed inside the research center area so it is protected from unwanted visits, the center further providing access to power plugs and the network.

Two successive campaigns were made during the 2015 summer. During the first phase (WatTo1), from 12 May to 6 July, the telescope was placed $40\,\mathrm{m}$ away from the base of the tower, pointing at the tank with an angle of $30°$ above the horizon. Power and network were brought by cables from a nearby building. For the second phase (WatTo2), from 17 July to 8 September, the telescope was moved closer, at $32\,\mathrm{m}$. This way the telescope pointed more toward the zenith, at $35°$. The telescope was then in total autonomy: no network connection and powered by a battery and solar panels.

IV.D.2 Experimental setup

A muon telescope has been designed for this experiment. Four MultiGen detectors can be placed parallel to each other. The distance between them was fully adjustable. This way the field of view and the angular resolution can be tuned with respect to the constraints on the muography resolution. To reconstruct a straight track, only two detectors are needed but a third one is mandatory to cut off the noise. The fourth one is added for two main reasons: it provides a backup if any detector is failing during the campaign and it is increasing the overall efficiency.

$$\epsilon_{3/3} = \epsilon_1^3 \tag{IV.20}$$

$$\epsilon_{3/4} = \binom{4}{3}\epsilon_1^3(1-\epsilon_1) + \epsilon_1^4 = 4\epsilon_1^3 - 3\epsilon_1^4 \tag{IV.21}$$

Considering the same efficiency ϵ_1 on all detectors, if only three of them are used, all of them have to have a signal which leads to an overall efficiency $\epsilon_{3/3}$ whereas if four detectors are used, one can ask for at least three of them to be hit so $\epsilon_{3/4} > \epsilon_{3/3}$. To read the four Micromegas, a FEU card is used, providing on the same time the readout system and the trigger. Drift and amplification voltages are provided by the HVPS card described in section III.C. A unique negative channel is linked to the 4 cathodes through a derivation box. All micro-meshes are set to electrical ground and each resistive layer is linked to a dedicated positive high voltage channel. To control both the readout and the high voltage a nano-PC is used. It is an ARM-based (smartphone technology), credit card size board that is capable of storing the data and control the run parameter [60, 61]. At the cosmic muon rate, even a full online treatment (demultiplexing, clustering tracking and storing) is possible. The whole setup used 40 W of power, including the cooling fans. The power came through a standard laboratory supply for WatTo1 (220 V AC to 12 V DC) and through a controller during WatTo2. The controller switched between battery and solar panel, taking care of the battery charge and cutting the power when it is exhausted. During the whole campaign, the muon telescope was placed inside a tent to protect it from rain, wind and the wildlife as shown in Figure IV.4.


(a) First phase (b) Second phase

FIGURE IV.4 – Telescope setups inside its protecting tent for both phases of the WatTo experiment.

IV.D.3 Acquisition specificities

During the first phase, the four detectors were MultiGen of the first version. The production of the first MultiGens of the second version permitted to substitute the bottommost detector from a version 1 to a version 2 for the WatTo2 phase. The summer weather combined with the shadow of trees surrounding the area produced daily variation of temperature of an amplitude up to 31 °C (from 12 °C to 43 °C) as shown in Figure IV.5. It induced large variations of gain which perturbed the data taking for the reasons explained in section III.D. In particular, the gain dropped below the triggering threshold around noon as shown in Figure IV.6. To deal with it, a feedback of the resistive layer voltage with respect to the temperature measured by a precision USB probe from Dracal has been implemented. Linear corrections of the amplification voltage with respect to the temperature were enough to keep the signal below the saturation regime and above the triggering threshold even if the gain variation is not linear with respect to the temperature. The correction is detector dependent but it is of the order of $1\,\mathrm{V K^{-1}}$. Furthermore, the triggering threshold was carefully adjusted as detailed in section III.B.

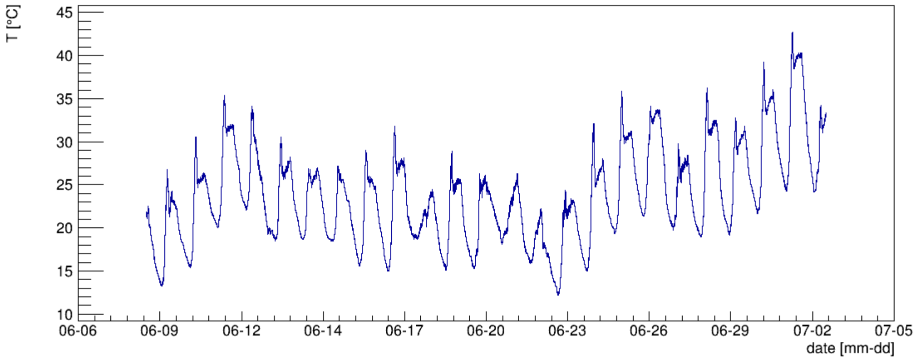

FIGURE IV.5 – Variations of the temperature during the first phase of the WatTo experiment.

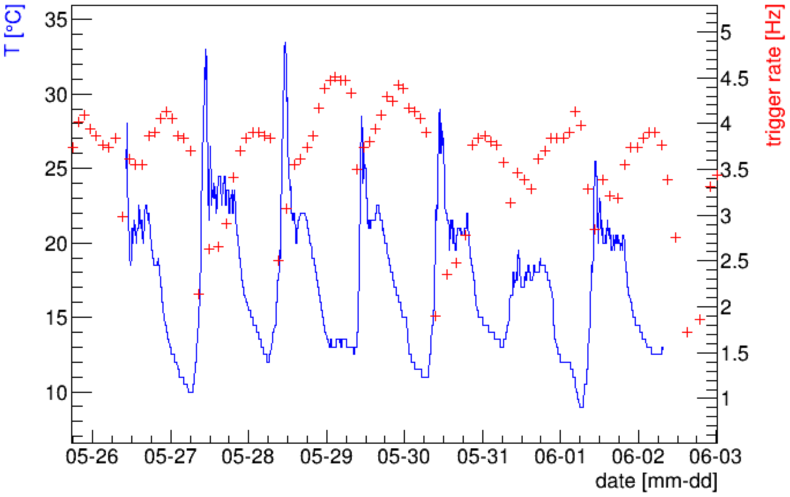

FIGURE IV.6 – Variations of the trigger rate compared to the temperature before corrections were implemented.

During the second phase, the only power input available was a 12 V-160 Ah truck battery recharged by two solar panels. The total surface of the panels was $1.75\,\mathrm{m}^2$ with a peak power production of 300 W. The battery charge was controlled by a maximum power point tracker (MPPT) regulator. However, as seen in Figure IV.4b, there are a lot of trees all around the experimental area so very few direct sunlight was available. This led to very poor solar panel efficiency so the 48 h autonomy of the battery was only extended by two days. After the four days of data taking, the battery controller shut down the telescope allowing the battery to charge up. When the battery was fully recharged, the controller switched on the telescope again and an operator was able to start a new acquisition. In this configuration, there was no proper electrical ground. For this reason and because the telescope was composed of the first version MultiGens, the noise levels did not allow for the self-trigger operation. To avoid this problem, a ground rod was hammered in the soil and connected to the telescope metallic frame.

IV.D.4 Results

The muonic shadow of the water tower has been successfully recorded during both phases as seen in Figure IV.7a and Figure IV.8. The bright spot exactly in the middle corresponds to coherent noise misidentified as muon tracks that could not be suppressed, this is not a physical signal. The presented plots correspond to the muon flux extrapolated to the plane perpendicular to the telescope line of sight passing through the center of the water tower tank. The flux extrapolated to the water tower mid plane does not present further interests. Moreover, since the dimension of the instrument is nearly negligible with respect to the water tower dimensions, the parallax effect does not significantly affect the image if it is plotted with respect to the zenith and azimuth angles.

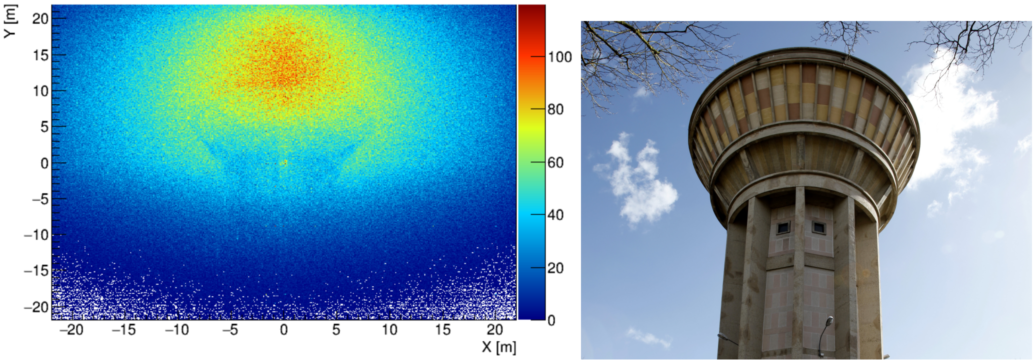

(a) Muograph.

(b) Photograph.

FIGURE IV.7 – Raw muon flux measured during the first phase of WatTo expressed in term of collected muons compared with the photograph.

The overall time of both phases is roughly the same (55 days for the first phase and 52 for the second one) but because of the powering problems during the second phase the acquisition time is smaller. Nevertheless, the muon statistics is higher in phase two because of the telescope inclination which was closer to the zenith: 25° (resp. 35°) above the ground in phase one (resp. in phase two). This orientation takes advantage of the $\cos^2(\theta)$ mean distribution of cosmic muons. Thanks to the higher flux, an image of the empty water tower was made during the only two days annual purge of the tower as shown in Figure IV.8b. The images produced with every data set show details of the structure, in particular the three concrete rings supporting the tank, the pillars of the lower parts and also the hollow spiral stairwell in the center. As expected, the water also appears clearly, with an absorption around $50\,\%$, representing around $10\,\mathrm{m}$ of water in addition to the concrete walls. The architectural structures are even more visible in Figure IV.8b because the water absorption is not masking the concrete one. Furthermore, the upper ring is more visible in the data

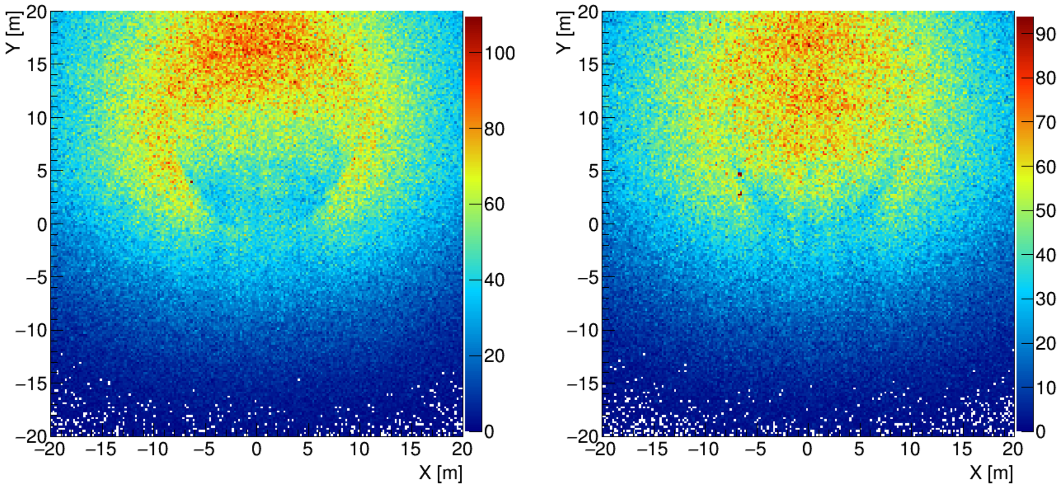

(a) Data taken while water was inside the tank.

(b) Data taken during a drain.

FIGURE IV.8 – Muon flux measured during the second phase of WatTo expressed in term of collected muons.

from phase one because it happened to be nearly aligned with the convex roof of the tank.

Knowing that we can visually distinguish the empty from the full tower we measured the evolution of the tank water level throughout the days. Indeed, during a time window, one can study the variation of the number of muons passing by the tank area which can be defined from the static images. To suppress systematic effects due to the muon flux variations *e.g.* with the atmospheric pressure, a normalization by the flux passing anywhere but by the tank can be made. Since the muon opacity of all the structures around the tank does not change, it can be used as a reference. Significant variations of the relative opacity $\Delta\varrho/\varrho$ occurring with a time scale down to the order of a few hours have been monitored using this technique. A drain of the tank has been monitored with this method, the comparison between the muon data and the probe inside the tank is shown in Figure IV.9, the correlation coefficient between both data sets is -0.69.

Because of the acceptance and open-sky flux difference between the different parts of the image, the proper visualization of the structures can be altered. One way to temper this effect is to use image processing techniques to make a normalization of the flux along a direction. An interesting direction is the vertical one:

$$\widetilde{\phi}_{m,z_I}(x,y) = \frac{\phi_{th,z_I}(x,y)}{\int \phi_{th,z_I}(x,y)\,\mathrm{d}y} \tag{IV.22}$$

This normalization is shown in Figure IV.10 and allows us to see more clearly the water inside the tank and the concrete roof.

Data corrected from the acceptance effect are not presented here because of the difficulty to model the correct acceptance of the detector. Indeed, because of the tight schedule, open-sky data could not be taken for any of the WatTo phases so this subtraction has to rely on a model. However, for the whole set of tracks three contributions are convoluted. These contributions correspond to the geometrical effect of the three possible couples of extremum detectors considered in the tracking. Furthermore, the resolution problems discussed in section III.F.1 affect the large angle tracks and distort the acceptance in the affected regions.

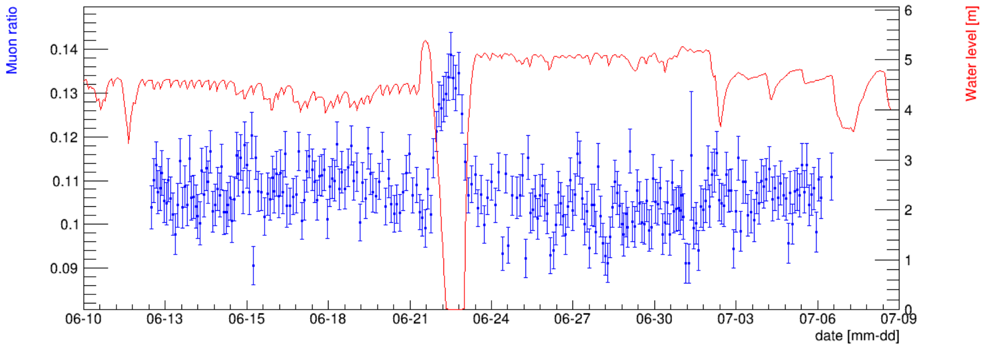

(a) Time serie.

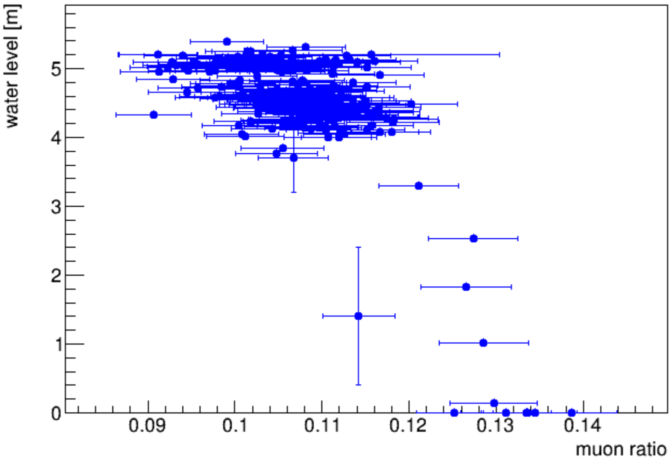

(b) Correlation.

FIGURE IV.9 – Comparison between the water level inside the tank and the ratio of the flux passing inside and outside the tank.

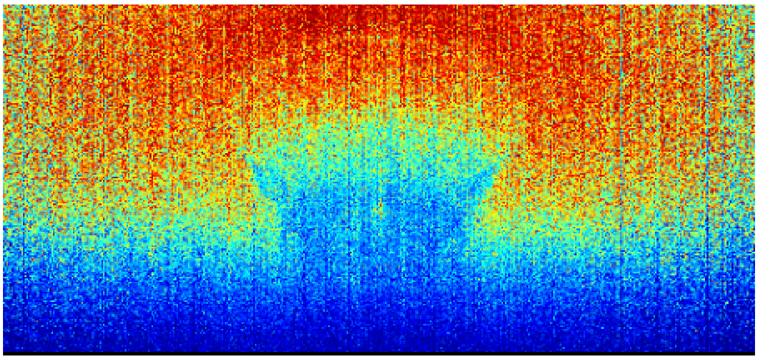

FIGURE IV.10 – Column by column normalized flux measured during the first phase of WatTo.

IV.E The ScanPyramids mission

Using the precious knowledge acquired with the prototype telescope during the WatTo experiment, observations of objects with higher scientific interest can be made. The schedule of the ScanPyramids mission made possible a collaboration[1] to study the Great Pyramid of Giza built for the pharaoh Khufu 4,500 years ago.

IV.E.1 Overview

The ScanPyramids mission is coordinated by the HIP institute (**H**eritage **I**nnovation **P**reservation) [62] and the Faculty of Engineering of Cairo. It is an association founded by Mehdi Tayoubi and Hani Helal which aims at using the last technological knowledge in order to study our cultural heritage in a nondestructive way. Following this idea, the ScanPyramids mission began to study the ancient Egyptian pyramids. This mission is conducted under the authority of the Egyptian ministry of Antiquities. However, collaborators from around the world are part of the mission. The French company Emissive is in charge of the photogrammetry measurements and the 3D modeling. The University of Laval (Canada) is in charge of infrared measurements. Along with the CEA team, two Japanese teams deployed muography instruments to study the pyramids. One comes from the Nagoya University and uses nuclear emulsions. The other one is a muon telescope built by the KEK and based on plastic scintillators. Both Japanese teams are taking data from the inside known cavities of the pyramid whereas we set up our muon telescopes outside. The aim of all the measurements is to search for unknown voids or cavities inside the great pyramid of Giza also known as the Khufu's pyramid in honor of the pharaoh who ordered its construction. A previous muography campaign was made by Alvarez in the 1960s in the Khafre's pyramid [63]. The presence or the absence of unknown voids can help the Egyptologists to unveil mysteries about the pyramid *e.g.* how it was built and what was its purpose. A sketch of the interior structure of the pyramid is shown in Figure IV.11. Another known void which does not appear on the sketch is a small chamber of $9\,\mathrm{m}^2$ behind the notch on the North-East edge of the Pyramid at $80\,\mathrm{m}$ above its base.[2]

IV.E.2 Experimental setup

From the first discussion between HIP and our CEA team in November 2015 to May 2016, three telescopes were designed, built and shipped to Egypt. The first one was named after Alhazen, the famous Arabic physicist and mathematician which was the first to scientifically describe the optic of the eye. The second one was named Alvarez as a tribute to Luis Walter Alvarez who was the first to use muons to study the Egyptian pyramids by using spark chambers inside the Khafre's pyramid. The third one was named after André Brahic, who discovered the Neptune rings. Knowing the flaws of the WatTo telescope, the mass and transport constraints, all mechanical parts have been lightened and a $77{\times}87{\times}159\,\mathrm{cm}^3$ fly-case has been used as

---

[1] While ScanPyramids was announced on 25th October, the last day of WatTo data taking was the 16th September.

[2] In order to precisely position the pyramid with respect to the muon data, a measurement of the height of specific locations along the edge have been made using precision barometers as detailed in Appendix A.

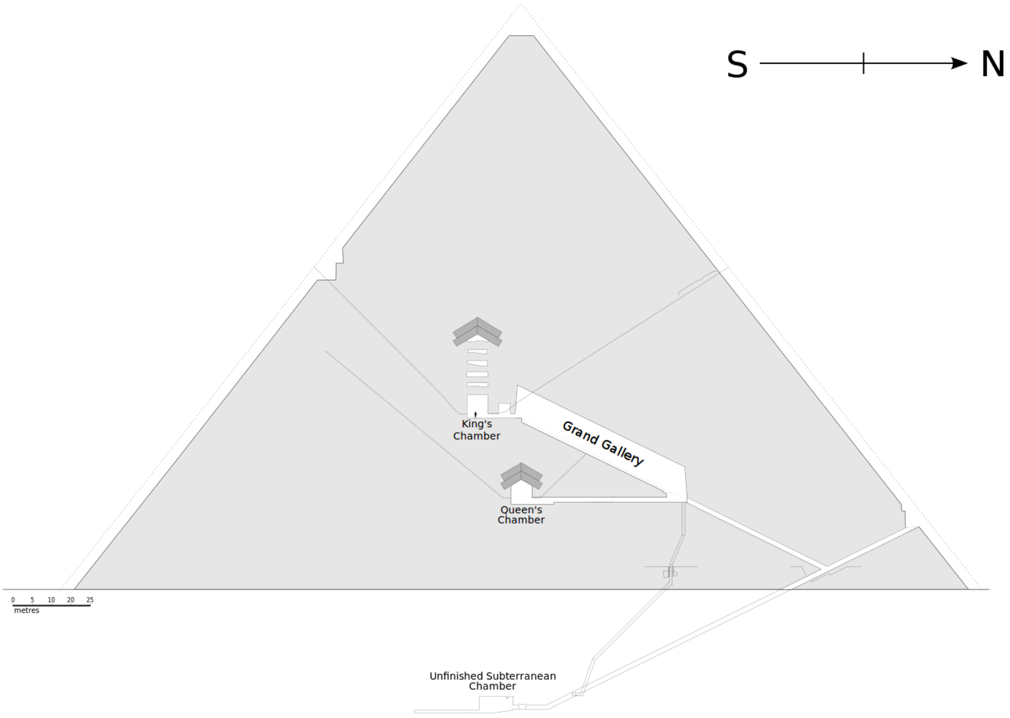

FIGURE IV.11 – Diagram showing the internal structures of the Khufu's pyramid.

an enclosure. At the beginning of June 2016, after a checkup at the Cairo University, the three telescopes were deployed on the Giza plateau. Even if the muon technology had already been tested on the Dashur pyramids by the Nagoya team, our specific technology was still untested in Egypt. The ministry of Antiquity then required that we detect an already known void to be confident in further results. This is why our three telescopes were set up in order to detect the cavity behind the North-East edge notch. This configuration allowed us to scan in the same time the upper 2/3 of the edge area in order to detect potential voids. Calculations have been made in order to determine the best position to maximize the significance of a signal induced by a void near the edge. Three main effects have to be considered. The first one is the $\cos^2(\theta)$ distribution of the cosmic muons:

$$\cos^2(\theta) = \cos^2\left(\arctan\left(\frac{\Delta z}{\sqrt{\Delta x^2 + \Delta y^2}}\right)\right) \tag{IV.23}$$

where Δx, Δy and Δz are the distances between the telescope and the cavity projected, respectively, along the north-south, the east-west and the vertical axes. Since the relative error on the flux is proportional to $1/\sqrt{N_\mu}$, the largest number of muon have to be collected in a limited amount of time. So because of the zenith angle distribution of muons, the discriminating power is increasing if the telescope points more upward, that is to say placed closer to the pyramid. The second factor is geometrical, it corresponds to the solid angle of the cavity that can be seen. Again, the larger the solid angle is, the more muons passing through the cavity will be recorded. Given an object transverse length, the solid angle decreases with the distance:

$$\Omega = \frac{1}{2}\left(1 - \sqrt{1 - \frac{L^2}{2(\Delta z^2 + \Delta x^2 + \Delta y^2)}}\right) \tag{IV.24}$$

Where L is the typical dimension of the void. The last factor is the absorption factor. Indeed, the excess of muons in the direction of the cavity is directly related to the ratio between the cavity length and the muon path length inside the pyramid. Considering the relative error on the collected muons, the excess of muons has to be maximized in order to increase the significance.

As it can be seen in Figure IV.12, the telescope position has to be carefully chosen with respect to the particular region of the pyramid that has to be studied. These plots show the different effects while pointing toward the chamber behind the North-East edge for a telescope that has to be placed on the ground which corresponds to the pyramid base plane. This configuration presents a symmetry with respect to the vertical plane of $45°$ azimuth. The cosmic flux effect forces the telescope zenith angle to be the highest possible. Since the altitude of the telescope is constrained *i.e.* it must be on the ground, the solid angle effect is very similar to the cosmic flux one. The opacity ratio effect tends to minimize the path length inside the pyramid. In this case, it favors an horizontal line of sight perpendicular to the symmetry plane so the maximum ratio corresponds to a telescope at the infinity. Taking care of these effects and the constraints on the Giza plateau, two symmetrical positions were chosen: one on the North face and one on the East face. The North position is $37\,\mathrm{m}$ away from the face and $25\,\mathrm{m}$ at the East of the center of the pyramid.

Similarly, the sensitivity factor for all void placement inside the pyramid given a telescope specific position can be computed. This sensitivity map is shown in Figure IV.13 for the North site position. In Figure IV.13c, it can be observed that the contrast decreases rapidly as the distance from the edge increases because of the size and the geometry of the pyramid.

Only one telescope was placed on the North site (Alhazen), and the two others were on the East site as shown in Figure IV.14. They were protected from the wind and the sand by thick fabric tents, the East site tent inside is pictured in Figure IV.15 during the setup.

During the whole data acquisition campaign, 3G dongles allowed the connection each telescope to the Internet. $220\,\mathrm{V}$ AC was brought to the tent to power the telescopes which had $12\,\mathrm{V}$ truck battery in case of power shortages. An AC to DC converter allows a regulator to charge the battery or switch to it. 5 B5 bottles[1] of a premixed Ar-$\mathrm{CF_4}$-$\mathrm{iC_4H_{10}}$ 95:3:2 mixture were providing gas to the telescopes. Initially filled at $120\,\mathrm{bar}$, two of them were placed at the North site and three of them at the East one but only one bottle at a time was used. At the East site, a unique gas circuit was made for both telescopes: in the direction of the gas flux, after the last detector of Brahic came the first one of Alvarez. In order not to collect too much open-sky muons and to reduce the trigger rate, the telescopes line of sight were not pointed directly toward the chamber behind the notch but more toward the center of the pyramid. Indeed, since no dynamic measurement is planned, the open-sky muons are of little interest compared to the amount of recorded data they represent (over $95\,\%$).

---

[1] B5 bottles contains $5\,\mathrm{L}$ of compressed gas.

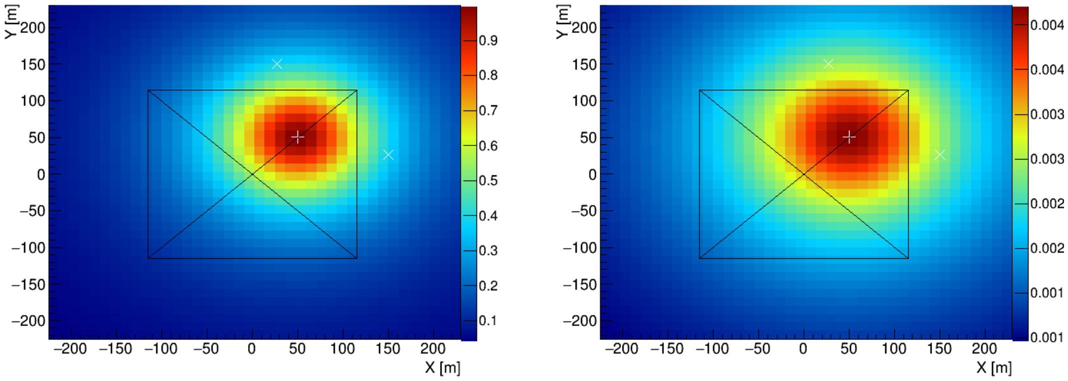

(a) Effect of the muon distribution.

(b) Effect of the solid angle.

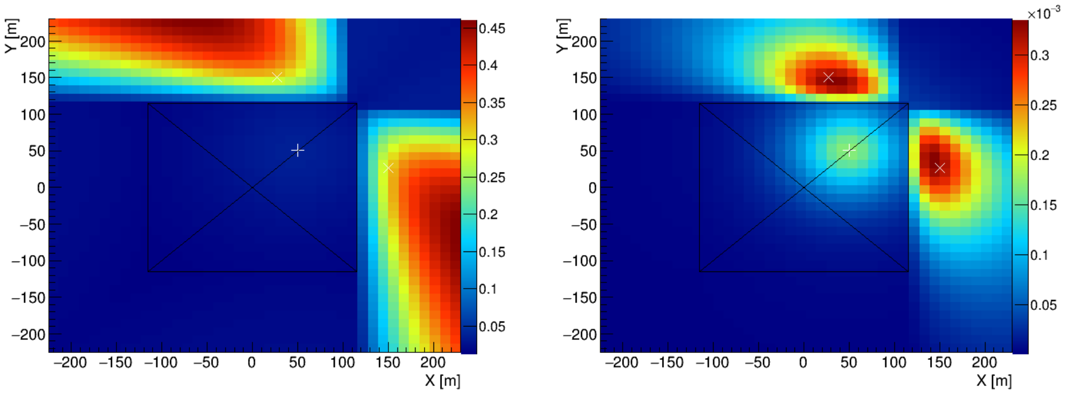

(c) Effect of the relative opacity.

(d) Combined effects.

FIGURE IV.12 – Maps used to determine the best placement. The chamber behind the notch position is the white plus and the chosen telescope positions are the white crosses.

As it can be seen in Figure IV.15, the detectors were placed in doublets. Their precise positioning is shown in Table IV.3[1].

Telescope	**positions** [mm]			
Alhazen	0	99.74	450	550
Alvarez	0	98.1	500	600
Brahic	0	99.4	450.25	550

TABLE IV.3 – Detector position along the line of sight axis for each telescope.

This particular positioning of the detectors inside the telescope presents several advantages. The first one is that it minimizes the muon track angle resolution because each doublet provides two independent position measurements at nearly the same level ($\sim 10\,\mathrm{cm}$) and the measurements of both doublets are as far as possible ($\sim 45\,\mathrm{cm}$). Another one is that it minimizes the acceptance change if a detector is malfunctioning during the campaign. The last one is that, given the self-trigger configuration, it optimizes the acceptance to avoid large angle muons that are poorly reconstructed due to the detector flaws explained in section III.F.1. Indeed, the trigger is configured

---

[1] As described in section III.G, the position of the two extremal detectors are supposed to be exact.

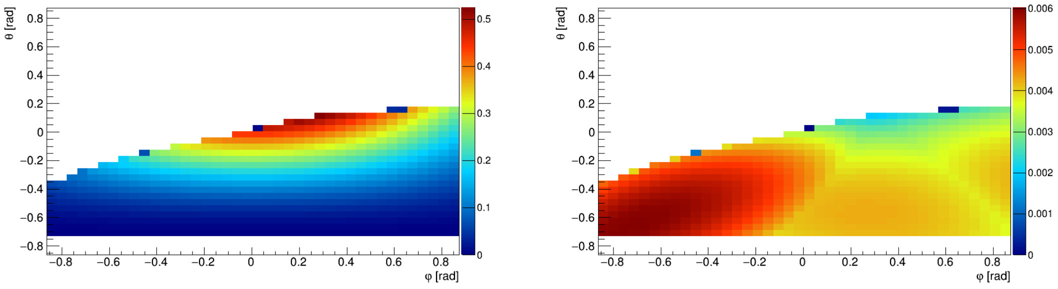

(a) Effect of the muon distribution.

(b) Effect of the solid angle.

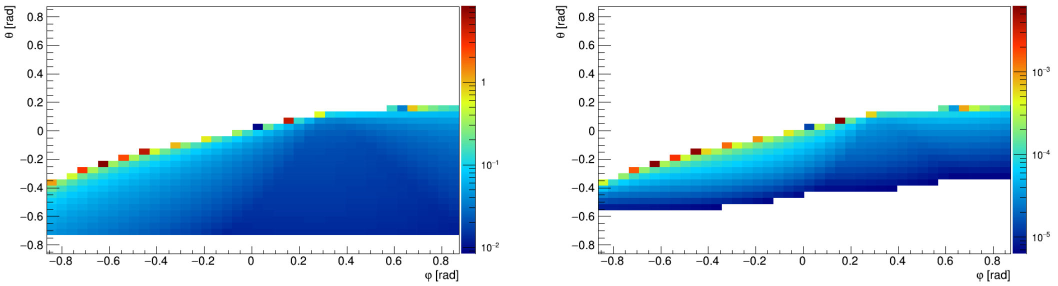

(c) Effect of the relative opacity.

(d) Combined effects.

FIGURE IV.13 – Maps of the telescope sensitivity for a chamber having the same size than the one behind the notch. Computed from the optimal position determined before with the telescope axis pointed toward the chamber behind the notch.

(a) East site tent location.

(b) North site tent location.

FIGURE IV.14 – Both site tents location around the great pyramid of Giza.

in order to select events when there is a significant signal in at least three detectors. Due to mechanical constraints, the detectors belonging to the same doublet could not be brought closer together. Knowing the position resolution of the detectors measured in section II.D.3.b and the distance between the doublet, the angular resolution is $0.9\,\mathrm{mrad}$. Taking into account this error and the multiple scattering of the muon inside the rock and along its path from the pyramid to the instrument, the extrapolated position of the muon is known with an uncertainty of $1\,\mathrm{m}$ near the pyramid edges. Since the cavities we aim to detect are a few meters wide, the level arm was chosen to get this small enough resolution.

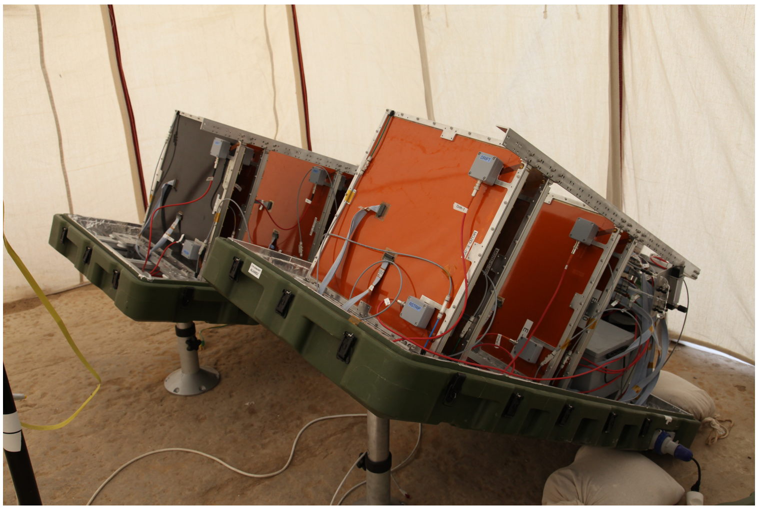

FIGURE IV.15 – Brahic (back) and Alvarez (front) telescopes inside their tent. During the setup the casing cover was not present.

IV.E.3 Acquisition specificities

Knowing the temperature conditions occurring at the Giza plateau and considering the temperature elevation due to the sun shining on the telescope's casing, some tests were made before sending the instruments to Egypt. No Micromegas had been operated at such high temperature before and the readout electronics was not designed to endure these conditions. A reduced design composed of only one detector and the whole electronics were put inside a drying oven. The proper operation of the system was recorded for temperatures up to 55 °C. However, the FEU card FPGA was operating at its critical temperature (85 °C) and the power consumption rose with the temperature because of leakage currents. To avoid any problem, an additional mechanical heat exchanger was designed to cool down the DREAM ASICs and the one of the FPGA was over-sized. An effect was observed both on the resistive MultiGen and a standard (*i.e.* metallic) Micromegas: a steady current between the micro-mesh and the anode appeared at $\sim$ 30 °C. Furthermore, this current was increasing with the temperature. It was *a posteriori* found on WatTo monitoring data as shown in Figure IV.16.[1]

Even if this effect is still not yet fully understood, it does not disrupt the data taking: it is indeed far below the maximum output current of the high voltage power supply, it does not introduce additional noise and the gain can be kept constant thanks to the method described in section III.D.4 To properly implement it, the amplitude of physical signal in each detector have to be determined. To do this, a multi-threaded software has been developed to process the data in real time. It even allows to reconstruct the muon tracks online.

Unfortunately, even with the help of automatic restart scripts, the 3G connection kept disconnecting several times a week probably because of the local 3G network. Thanks to the help of the Egyptian team of ScanPyramids, the connection could be regularly physically rebooted. The way this 3G connection gives access to the Internet to the telescopes does not allow for direct incoming connection. To be able to monitor the

---

[1] The current was measured by the CAEN A7501 module which use a $\sim 500\,\mathrm{M\Omega}$ resistance between the load and the ground to measure the current. This is why a steady current of $\sim 0.8\,\mu\mathrm{A}$ is measured even at low temperature.

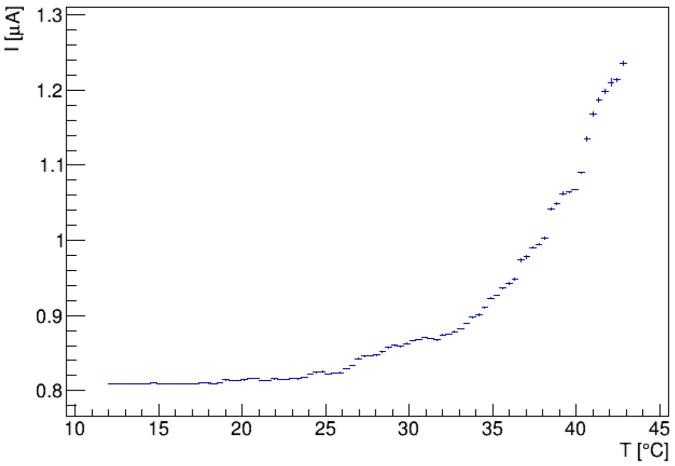

FIGURE IV.16 – Evolution of the amplification current with respect to the ambient temperature in a first version MultiGen.

data taking, the telescope had to initiate a connection to a public server in order to make a secure tunnel.

Using the expertise gathered with the WatTo experiment, a Dracal precision thermometer and barometer allowed to adjust the high voltages with respect to the environmental conditions. However, thanks to the portable air conditioner inside the tents[1], the temperature variations were not higher than the ones measured during the WatTo experiment as shown in Figure IV.17.

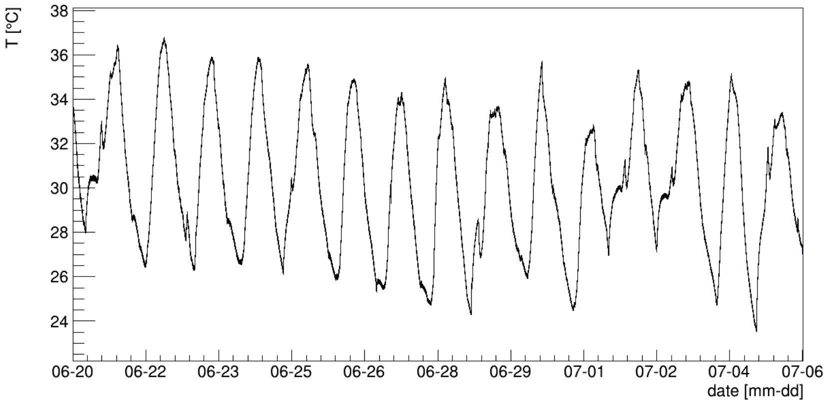

FIGURE IV.17 – Temperature inside Brahic telescope casing during the month of June 2015.

One major problem appeared during the data taking campaign concerning the Alvarez telescope. One of the four detectors suddenly malfunctioned. This detector showed a major gain inhomogeneity between its two halves. Since the separation is across the resistive strips direction, it seems to come from a default in the electrical connection between the strips and the high voltage input. Indeed, starting from the high voltage connection, the zone corresponding to the first half of the resistive strips showed a gain significantly higher than the ones farther from the input. Later

---

[1] The air conditioning was not installed because of the constraints of the telescope operation but for the well-being of the guards.

on, the detector was investigated in clean room and showed a discontinuity of the silver paste assuring the electrical connection. Because of this problem, the proper operation of the detector was not possible: either one half signal was saturated or the other half signal was too faint to pass the trigger threshold.

Due to the strong winds occurring on the Giza plateau during sand storms, the tents were blown up several times during the data taking. Concerns raised about the displacement of the telescopes during these events. To test if the telescopes moved, the flux maps before and after the event were compared to check for potential changes. No significant ones were observed so it was concluded that there was no movements. Indeed, even a slight shift of the telescope position or angle would induce a displacement of the edge which constitutes a clear singularity in the data set.

IV.E.4 Results

After three months of continuous data taking and the exhaustion of all the gas bottles, the telescopes were shut down at the end of August. Both Alhazen and Brahic telescopes gathered significant data: Alhazen recorded 11 469 737 good muons while Brahic recorded 11 624 984. However, because of the gain inhomogeneity problem, the Alvarez telescope did not acquire enough data (3 652 995 muons). As shown in Figure IV.18, the data taking was stable over time except when the gas bottles were exhausted and then changed (the 28th June for Brahic and the 29th July for Alhazen) or because of gas flow adjustments made around the 16th July for Brahic and around the 3rd August for Alhazen.

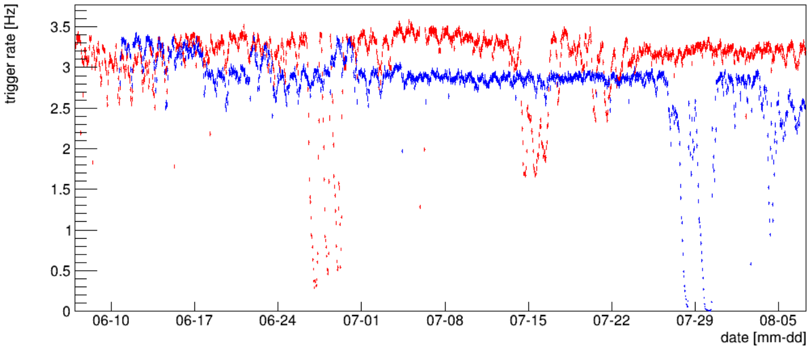

FIGURE IV.18 – Muon rate in Brahic (red) and Alhazen (blue) telescopes.

As seen in Figure IV.19, the telescopes seems to have detected up going muons. However, since the telescopes axes are about 25° above the horizon, their acceptance is large enough that they are able to detect muons crossing the telescope backwards. The component of the flux measured below the horizon is only due to this effect since the up going flux is suppressed by the flat Giza plateau. The binning of these plots is chosen such as the bin size corresponds to the position uncertainty in the pyramid since the statistics allows it[1]. Moreover, the flux map is not as relevant as the one of the WatTo experiment. Indeed, the opacity ratios are very different between the

---

[1] There is a trade-off between the bin size and the statistical fluctuations inducing an error equal to the square root of the bin content.

two cases: except from the air, the muons travel only a few meters inside absorbing material of the water tower (*e.g.* water and concrete) whereas they travel from 20 m at the level of the known cavity up to 200 m inside the pyramid's rock and eventually a few meters of air inside a void. This forced us to develop more advanced analysis techniques.

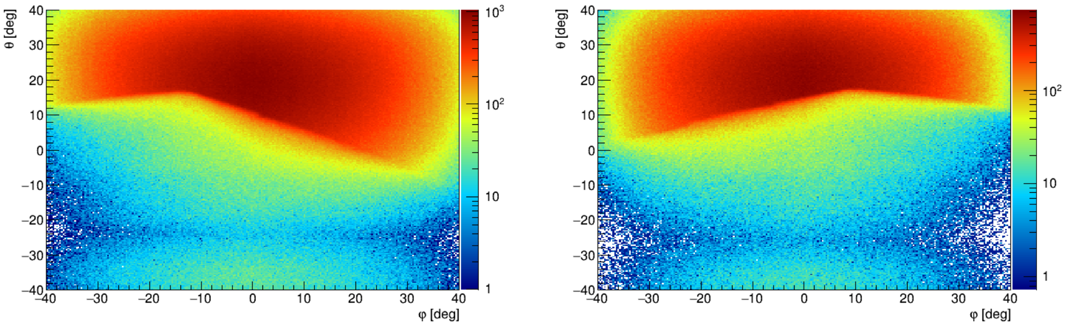

(a) Brahic data.

(b) Alhazen data.

FIGURE IV.19 – Flux map expressed in term of collected muons, in log scale.

To properly align the data with simulations or photographs, the straightforward way is to pinpoint the pyramid edges using the muon data. Since these edges correspond to a boundary between the free sky and several meters of rock, it corresponds to a strong gradient on the muon flux. In computer vision, several filters and algorithms have already been developed in order to extract this type of information. One of them is the Sobel filter [64]. It is able to compute the n^{th} order gradient along the image rows or columns. The given image is considered as a matrix were each pixel brightness is a matrix element, so to compute the gradient, the image matrix is convoluted with this 3×3 matrix:

$$K_{Sobel,x} = \begin{pmatrix} 1 & 0 & -1 \\ 2 & 0 & -2 \\ 1 & 0 & -1 \end{pmatrix} \tag{IV.25}$$

$$K_{Sobel,y} = K_{Sobel,x}^{\mathsf{T}} \tag{IV.26}$$

It is then possible to compute the gradient magnitude that is shown in Figure IV.20.

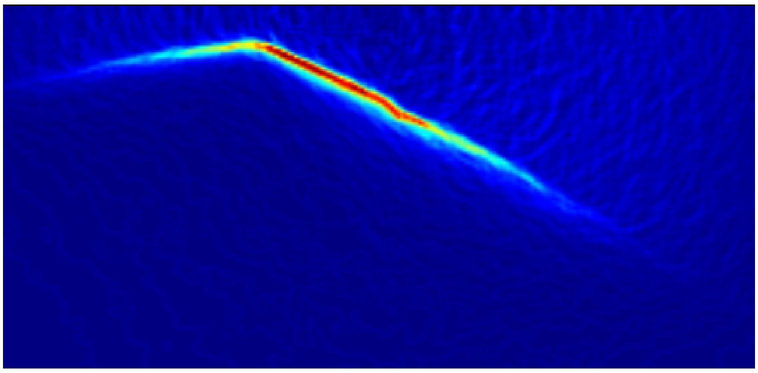

FIGURE IV.20 – Magnitude of the Sobel gradient computed with the Brahic telescope data.

An edge detector algorithm developed by Canny [65] and using this filter helped us to position precisely the edge of the pyramid as well as the notch as shown in Figure IV.21.

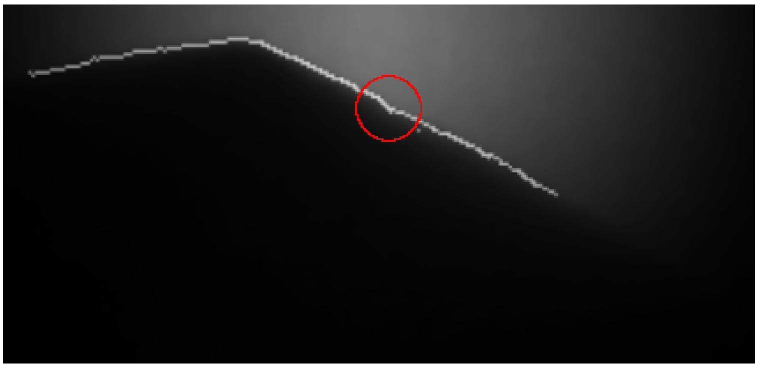

FIGURE IV.21 – Output of the Canny edge detection algorithm computed with the Brahic telescope data, the red circle indicates the notch.

Using this technique, the position of the summit and the edge equation can be determined for both Alhazen and Brahic data sets. The result is shown in Table IV.4.

Telescope	**Summit**		**Edge**
	$\boldsymbol{\theta}$ [°]	φ [°]	
Alhazen	17.6	8	$\theta = 3.14\varphi + 15.1°$
Brahic	16.8	-11.7	$\theta = -4.87\varphi + 11.1°$

TABLE IV.4 – Structure positions determined in telescope data sets.

Moreover, a void inside the pyramid will induce a local maximum of the muon flux. This extremum can be detected using the second order gradient. However, the typical size of the voids that should be detected is a few meters which corresponds to a single pixel in our image and the statistical fluctuations of the muon count produce a noise on the second order gradient. These fluctuations can be partially suppressed by introducing a smoothing which corresponds to a Gaussian blur, however, doing so will also average out the void signal. Therefore, it is not possible to detect such voids using only the image filtering as shown in Figure IV.22 even if there are hints of the chamber behind the notch in this gradient.

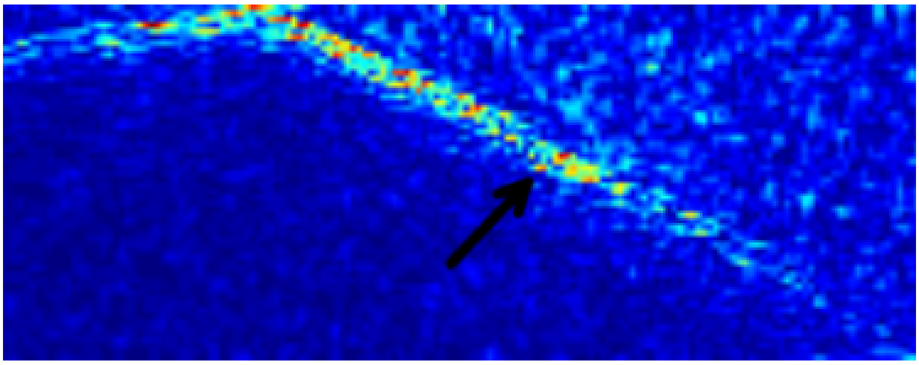

FIGURE IV.22 – Norm of the second order gradient of the muon flux measured by Brahic, the tip of the arrow indicates the chamber behind the notch position.

To be able to clearly identify voids, another technique is to plot the muon count along interesting directions. For example, because there is a chamber at $80\,\mathrm{m}$ above the ground just a few meters away from the edge means that there can be other ones along the edge at different altitudes. Making a few meter wide slices parallel to the edge can allow us to detect the known void and then hypothetical voids. As discussed in section IV.E.2, even if the flux factor will change along this type of slices, the relative opacity effect remains nearly constant. Using this technique, we were indeed able to successfully detect the chamber behind the notch at $80\,\mathrm{m}$ above the ground as shown in Figure IV.23a and Figure IV.23b. This success was mandatory for the Egyptian authorities: without it, they could not accept any further results from our instruments. Since the slices are parallel to the edge, a new coordinate system (θ', φ') can be defined such as the pyramid summit is the origin, θ' is the coordinate along the edge toward the North-East basis corner and φ' is the corresponding perpendicular coordinate in which the free sky corresponds to $\varphi' > 0$. This coordinate system is telescope dependent. The measured position of the chamber behind the notch is shown in Table IV.5.

Position	**Alhazen**	**Brahic**
θ' [°]	14.8 ± 0.3	14.1 ± 0.3
φ' [°]	-1.7 ± 0.2	-2.3 ± 0.2
θ [°]	10.7 ± 0.4	8.56 ± 0.05
φ [°]	-2.1 ± 0.4	0.0 ± 0.4

TABLE IV.5 – Measured positions of the chamber behind the notch.

Moreover, another anomaly called C1 appeared in both Brahic and Alhazen telescopes. Thanks to its measured position with respect to both telescopes as shown in Table IV.6, one can deduce that the anomaly in the two telescopes corresponds to two intersecting lines of sight that cross near the edge of the pyramid at $111\,\mathrm{m}$ above the ground. These measurements are extracted from Figure IV.23c and Figure IV.23d.

Position	**Alhazen**	**Brahic**
θ' [°]	9.1 ± 0.3	7.0 ± 0.5
φ' [°]	-2.7 ± 0.3	-1.7 ± 0.3
θ [°]	12.3 ± 0.4	12.2 ± 0.1
φ [°]	0.1 ± 0.1	-6.2 ± 0.6

TABLE IV.6 – Measured position of the C1 cavity.

However, if taken independently the signal they detect does not reach a sufficient significance to claim a discovery, but the combination of both Alhazen and Brahic telescopes data shows the discovery of a new chamber which was unsuspected at this time. The excess muon data is shown in Table IV.7. Indeed, for the chamber behind the notch, Alhazen data (resp. Brahic data) have a significance of 4.6σ (resp. 4.5σ) but as the excesses correspond to the same 3D region, combining them allow us to have a significance of 6.4σ which passes the discovery threshold. The situation is similar for the C1 discovered cavity, Alhazen (resp. Brahic) data show an excess of 4.1σ (resp. 4.0σ). The combined signal significance is then 5.7σ.

Cavity	Alhazen	Brahic	Total
Behind the notch	68.7±14.8	75.9±16.9	144.6±22.5
C1	59.2±14.5	69.8±17.5	129.1±22.7

TABLE IV.7 – Measured muon excess corresponding to both the known and the discovered cavities.

Other anomalies appeared but none of them were of sufficient significance or consistent in both Alhazen and Brahic data sets. Moreover, as presented in Figure IV.13, there might be voids in the lower part of the edge but the sensibility is too law to detect them. Egyptologists and architects formulated lots of theories concerning the pyramid and the way it was built. One of them assumed that the blocks of limestone were carried up through narrow tunnels spiraling inside the pyramid. These passages were not wide enough to take the turn at the corners of the pyramid so this theory supposes the existence of rotation chambers. Following this hypothesis, there must be several chambers, regularly spaced, along each edge, the chamber behind the notch and the C1 cavity we discovered being two of them. However, no hints of the tunnels have yet been found and the scan of the other edges to check if there are similar voids is ongoing at the time this document is written as another data taking has started in mid-January 2017.[1] At last, the interpretation of the existence of the anomalies detected during the whole ScanPyramids mission is let to the experts of the antique Egypt.

---

[1] A joint publication from all three ScanPyramids muography teams concerning the data taken in 2017 is available in [66].

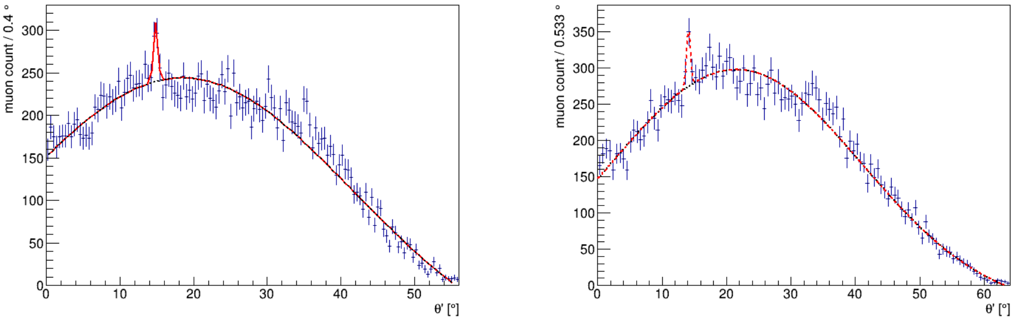

(a) Alhazen measured edge slice of $\varphi' \in [-4.4, -3.6]$ showing the chamber behind the notch induced excess.

(b) Brahic measured edge slice of $\varphi' \in [-2.5, -2.1]$ showing the chamber behind the notch induced excess.

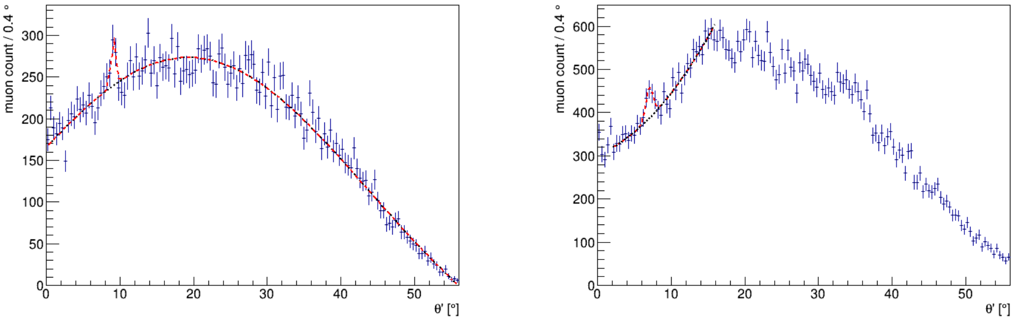

(c) Alhazen measured edge slice of $\varphi' \in [-3.0, -2.4]$ showing the C1 induced excess.

(d) Brahic measured edge slice of $\varphi' \in [-2.0, -1.4]$ showing the C1 induced excess.

FIGURE IV.23 – Slices muon count showing the excess measured for both cavities in both telescopes.

Chapter V

Scattering Muography

Absorption muography has multiple advantages such as being able to scan very large structures at once. However, it is a slow technique. In the case of smaller objects, it is possible to implement a different technique in order to reduce significantly the acquisition time.

V.A Principle

While the muons can be absorbed by matter, as it is developed in section I.C.2, they are also scattered by the medium they cross. The distribution of the scattering angle is of zero mean but its standard deviation depends on the muon momentum and the atomic number of the crossed material as shown in Equation I.10. Therefore, by measuring the deviation angle $\Delta\theta$ of each muon, a scattering density ξ can be inferred for a given mean muon momentum $p_0 = 4\,\mathrm{GeV}$, using the notations from section I.C.2:

$$\xi = \frac{E_s^2}{p_0^2 X_0} \tag{V.1}$$

The scattering standard deviation can then be expressed as:

$$\sigma_{\Delta\theta} = \frac{p_0}{p}\sqrt{s\xi} \tag{V.2}$$

This way, by measuring the scattering angle and the muon momentum, the scattering density and then the atomic number can be deduced. Moreover, by measuring the scattering position, it is possible to make a 3D map of the atomic number in a single acquisition. However, measuring a muon momentum is far more complex than tracking it. Hence, to keep the muon tomography imaging setup simple, most of the time, the momentum is not measured and is approximated by its mean. Of course, using a calorimeter with lead absorbing layers or using a trajectory bending magnet will give more accurate results.

V.A.1 Scattering measurement

In order to measure the scattering angle and position, the muon path must be measured before and after it crosses the scanned volume. In other words, because of the muon flux, there must be a tracker above and below the interesting area. It is also possible to use trackers at an angle with respect to the vertical but, in this configuration, the muon flux will be more and more reduced as the angle increases. This means that the acquisition time will increase as well.

Because the scattering angles that have to be measured are typically down to $1\,\mathrm{mrad}$[1], the angular resolution of both trackers is a key parameter. Micromegas detectors measure position, so given a position resolution, the angular one is determined by the level arm *i.e.* the distance between the detectors. However, doing so will affect the instrument acceptance and consequently the acquisition time.

V.A.2 Applications

This technique is suitable to scan any object whose size is of the order of the instrument one. For example, it is possible to scan stone statues in order to detect metallic structures inside them. These structures are used to straighten the sculpture and can help archaeologists to determine where, when and with which techniques they were made. It can also be applied to detect specific types of materials, in particular the ones containing high Z materials. In our time, many countries are vigilant about trafficking and the scattering muography can be deployed at the border control of harbors in order to detect special nuclear matter smuggling inside containers. This activity started after the pioneering work in Los Alamos [67]. Since then, it has developed through the CRIPT project [68] in Canada, an AWE founded project [69] in the UK and another in Italy [70].

The technique also elicited some interest in the field of nuclear waste. Indeed, it can help in the characterization and monitoring of waste barrels in order to detect leaks and to check the composition of the nuclear matter.

V.B Data inversion

While in absorption tomography, the opacity is directly linked to a mean density, in scattering tomography, the relation between the measurement and the 3D atomic number map is not as straightforward.

V.B.1 Principle

Measuring the scattering angle and the position gives direct information about the atomic number of the imaging volume content. However, the angle computed using the incoming and outgoing direction measurements does not correspond to a deviation angle. Indeed, it is not possible to know if multiple scatterings had occurred and in that case, each deviation angle is then hidden and only the sum is measured. The proportion of this type of event is increasing with the path length with respect to the radiation length X_0. Since both the incoming and outgoing muon paths are fully measured, not only the angle between their direction can be accessed but also the displacement $(\Delta x, \Delta y)$. It is the difference of position between the two paths locations extrapolated at the bottom of the imaging area as shown in Figure V.1 for the 2D case.

---

[1] $\sigma_\theta = 10\,\mathrm{mrad}$ for a $4\,\mathrm{GeV}$ muon passing through $5\,\mathrm{cm}$ of lead

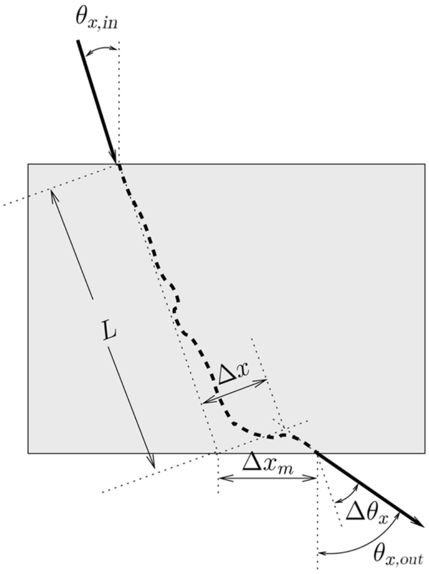

FIGURE V.1 – Sketch of the measured variables in the 2D case [71].

Of course, these two measurements are not independent: if the muon is scattered on the bottom side of the object, the displacement tends toward zero. For a single scattering:

$$\Delta x = \frac{z \tan(\Delta\theta)}{\cos(\theta_i)} \tag{V.3}$$

where θ_i is the zenith angle of the incoming muon and z is the altitude with respect to the bottom of the imaging area at which the scattering occurred. Because z is distributed uniformly between 0 and L_{tot} which is the height of the imaging area, it can be deduced that the displacement follows the same distribution than the deviation with a standard deviation of[1]:

$$\sigma_{\Delta x} = \frac{L_{tot}}{\sqrt{3}} \sigma_{\Delta\theta} \tag{V.4}$$

Furthermore, the covariance $\sigma_{\Delta\theta\Delta x}$ between the two is:

$$\sigma_{\Delta\theta\Delta x} = \frac{L_{tot}}{2} \sigma_{\Delta\theta} \tag{V.5}$$

V.B.2 The PoCA method

The collected data correspond to two half tracks: an incoming one and an outgoing one. In the perfect case, in an event where the muon was scattered only once and the position measurement is perfect, these two tracks correspond to two crossing lines. The crossing point is the scattering location and the angle between these lines is the scattering angle. However, in reality, the two tracks do not intersect because of two effects: the detector resolution and the less significant scatterings. To measure the significant scattering position and angle, the minimum sized segment between these two lines can be computed. The segment center which is named the **P**oint **o**f **C**losest **A**pproach (PoCA) can be interpreted as the scattering position. The scattering angle can be calculated using the angle between the lines direction vector whether the lines

---

[1] It uses the relation between the variance of two random variables X and Y and their expected value E: $Var(XY) = Var(X)Var(Y) + Var(X)E(Y)^2 + Var(Y)E(X)^2$.

intersect or not. Moreover, the length of the segment (**D**istance **o**f **C**losest **A**pproach, DoCA) can be used as a check for the single scattering hypothesis. Indeed, this length has to remain small with respect to the scattering point resolution if there is a unique significant scattering.

An estimate of the Z distribution can then be computed by making a 3D map of the scattering positions (*i.e.* the PoCAs) weighted by the associated scattering angle.

The main difficulties of this method are that it does not take into account the information carried by muons which are not scattered by the current voxel and it neither takes into account the acceptance effect *i.e.* the effect of muon number variation in each individual voxel.

V.B.3 ML-EM method

This method was first developed by Schultz *et al.* in [71, 72] and is based on a maximum likelihood estimation. As before, the PoCA is computed using the incoming and outgoing tracks. Using this point together with the entrance and exit points from the imaging volume defines the muon path. By dividing this volume into voxels (volumetric pixels), the list of voxels where the muon went straight through them can be computed together with the voxel in which the muon scattered *i.e.* the voxel where the PoCA is located.

The input data of this algorithm is $(\theta_{x,in}, \theta_{y,in})$ (resp. $(\theta_{x,out}, \theta_{y,out})$), *i.e.* the projection of the zenith angle of the incoming (resp. outgoing) muon path in the xz-plane and the yz-plane[1], the position where the muon enters (x_{in}, y_{in}) and exits (x_{out}, y_{out}) the imaged volume and eventually the muon momentum p.

Using these data, the scattering angle and the displacement for both projections and for each muon (indexed with i) can be computed as:

$$\Delta\theta_i = \theta_{i,out} - \theta_{i,in} \tag{V.6}$$

$$\Delta x_i = (x_{i,out} - x_{i,in}) \cos(\theta_{i,in}) - L_{tot} \sin(\theta_{i,in}) \tag{V.7}$$

where L_{tot} is the imaged volume size along the z axis. The displacement used here is the one projected along the incoming muon direction. The measured data can be grouped as M_i:

$$M_i = \begin{pmatrix} \Delta\theta_i \\ \Delta x_i \end{pmatrix} \tag{V.8}$$

Next, for each voxel, the muon path length inside it L_{ij} (where j is the voxel number) can be computed as if it traveled in it as a straight line.

$$L_{ij} = \frac{L_{tot}}{N_{vert}} \sqrt{1 + \tan^2(\theta_{ij,x}) + \tan^2(\theta_{ij,y})} \tag{V.9}$$

Where θ_{ij} is the angle at which the muon enters the voxel j and N_{vert} is the number of voxel layers along the vertical axis. The real muon path is unknown so it is approximated by two segments: from $(x_{i,in}, y_{i,in}, Z_{in})$ to the PoCA point and then from this point to $(x_{i,out}, y_{i,out}, 0)$. The set of crossed voxels $\mathcal{N}_{\mathcal{V},i}$ can then be defined

---

[1] Here the z axis is the vertical axis.

as:

$$\mathcal{N}_{\mathcal{V},i} = \{j \in [\![0, N_{\mathcal{V},tot}[\![\mid L_{ij} \neq 0\} \tag{V.10}$$

where $N_{\mathcal{V},tot}$ is the total number of voxels. The downstream muon path length T_{ij} can also be computed. It is defined as the sum of L_{ik} for every voxel $\mathcal{V}_k$ which will be crossed by the muon after the voxel $\mathcal{V}_j$:

$$T_{ij} = \sum_{k \in \mathcal{N}_{down,ij}} L_{ik} \tag{V.11}$$

$$\mathcal{N}_{down,ij} = \{k \in \mathcal{N}_{\mathcal{V},i} \mid s_i(\mathcal{V}_k) > s_i(\mathcal{V}_j)\} \tag{V.12}$$

where s_i is the curvilinear abscissa along the i^{th} muon path.

Using this information, the scattering density of each voxel ξ_j can be obtained. Using equations (V.2), (V.4) and (V.5), the covariance matrix $\Sigma_{ij,H}$ for the random variable $M_{ij,H}$ can be defined:

$$\Sigma_{ij,H} = \begin{pmatrix} \sigma^2_{\Delta\theta_{ij}} & \sigma_{\Delta\theta_{ij}\Delta x_{ij}} \\ \sigma_{\Delta\theta_{ij}\Delta x_{ij}} & \sigma^2_{\Delta x_{ij}} \end{pmatrix} = \begin{pmatrix} L_{ij} & \frac{L_{ij}^2}{2} \\ \frac{L_{ij}^2}{2} & \frac{L_{ij}^3}{3} \end{pmatrix} \frac{p_0^2 \xi_j}{p^2} \tag{V.13}$$

$$M_{ij,H} = \begin{pmatrix} \Delta\theta_{ij} \\ \Delta x_{ij} \end{pmatrix} \tag{V.14}$$

where $\Delta\theta_{ij}$ (resp. Δx_{ij}) is the angle (resp. displacement) induced by the scattering inside the j^{th} voxel. This covariance matrix can be used for each voxel but in that case the displacement and the scattering angle for each voxel $M_{ij,H}$ have to be estimated. Since it is not possible, it is denoted as hidden data with an H. The measured scattering angle is just the sum of the scattering in each vector:

$$\Delta\theta_i = \sum_{j \in \mathcal{N}_{\mathcal{V},i}} \Delta\theta_{ij} \tag{V.15}$$

However, it's more complicated for the displacement because it depends on the path downstream of the considered voxel. Indeed, the measured displacement is:

$$\Delta x_i = \sum_{j \in \mathcal{N}_{\mathcal{V},i}} \left(\Delta x_{ij} + L_{ij} \sin \left(\sum_{\substack{k \in \mathcal{N}_{\mathcal{V},i} \setminus \mathcal{N}_{down,ij} \\ k \neq j}} \Delta\theta_{ik} \right) \right) \tag{V.16}$$

Because the scattering angles are small, it can approximated it by:

$$\Delta x_i = \sum_{j \in \mathcal{N}_{\mathcal{V},i}} \left(\Delta x_{ij} + L_j \sum_{\substack{k \in \mathcal{N}_{\mathcal{V},i} \setminus \mathcal{N}_{down,ij} \\ k \neq j}} \Delta\theta_{ik} \right) = \sum_{j \in \mathcal{N}_{\mathcal{V},i}} (\Delta x_{ij} + T_{ij} \Delta\theta_{ij}) \tag{V.17}$$

By computing the correlations for each voxel, the covariance matrix Σ_{ij} for the measured data M_i is then:

$$\Sigma_{ij} = \begin{pmatrix} L_{ij} & \dfrac{L_{ij}^2}{2} + L_{ij}T_{ij} \\ \dfrac{L_{ij}^2}{2} + L_{ij}T_{ij} & \dfrac{L_{ij}^3}{3} + L_{ij}^2 T_{ij} + L_{ij}T_{ij}^2 \end{pmatrix} \frac{p_0^2 \xi_j}{p^2} = \mathcal{T}_{ij} \frac{p_0^2 \xi_j}{p^2} \tag{V.18}$$

where $\mathcal{T}_{ij}$ is defined as:

$$\mathcal{T}_{ij} = \begin{pmatrix} L_{ij} & \dfrac{L_{ij}^2}{2} + L_{ij}T_{ij} \\ \dfrac{L_{ij}^2}{2} + L_{ij}T_{ij} & \dfrac{L_{ij}^3}{3} + L_{ij}^2 T_{ij} + L_{ij}T_{ij}^2 \end{pmatrix} \tag{V.19}$$

Because each muon passes through a set of voxels, the correlation matrix describing their scattering is:

$$\Sigma_i = E_i + \sum_{j \in \mathcal{N}_{\mathcal{V},i}} \Sigma_{ij} \tag{V.20}$$

where E_i is a matrix that allows the propagation of detection errors. For a tracker with a position resolution σ_{pos} and a level arm l:

$$E_i = \frac{\sigma_{pos}^2}{l^2} \begin{pmatrix} \left(\dfrac{1}{1 + \tan^2 \theta_{i,in}}\right) + \left(\dfrac{1}{1 + \tan^2 \theta_{i,out}}\right) & 0 \\ 0 & 2l^2 \end{pmatrix} \tag{V.21}$$

The likelihood $\mathcal{L}$ one wants to maximize is then the product of the probability of each hidden scattering $M_{ij,H}$ knowing the set of ξ_j:

$$\begin{aligned} \mathcal{L} &= \prod_{i=0}^{N_{\mathcal{M}}} \prod_{j \in \mathcal{N}_{\mathcal{V}i}} \mathbb{P}(M_{ij,H} \mid \xi_j) && \text{(V.22)} \\ &= \prod_{i=0}^{N_{\mathcal{M}}} \prod_{j \in \mathcal{N}_{\mathcal{V}i}} \frac{1}{2\pi \sqrt{\det(\Sigma_{ij,H})}} \exp\left(-\frac{1}{2} M_{ij,H}^{\mathsf{T}} \Sigma_{ij,H}^{-1} M_{ij,H}\right) && \text{(V.23)} \end{aligned}$$

where $N_{\mathcal{M}}$ is the total number of muons. This way, the log-likelihood can be defined as:

$$\begin{aligned} \log(\mathcal{L}) = \sum_{i=0}^{N_{\mathcal{M}}} \sum_{j \in \mathcal{N}_{\mathcal{V}i}} \Bigg(& - \log(\xi_j) \\ & - \frac{p^2}{2\xi_j p_0^2} M_{ij,H}^{\mathsf{T}} \begin{pmatrix} L_{ij} & \dfrac{L_{ij}^2}{2} \\ \dfrac{L_{ij}^2}{2} & \dfrac{L_{ij}^3}{3} \end{pmatrix}^{-1} M_{ij,H} \\ & + \log\left(\frac{L_{ij}^2 p^2}{4\sqrt{3}\pi p_0^2}\right) \Bigg) \end{aligned} \tag{V.24}$$

Since the last term does not depend on ξ_j, it can be ignored. At last the hidden data of the second term has to be estimated knowing the measured data. It can be shown that:

$$\frac{p_i^2}{p_0^2} M_{ij,H}^{\mathsf{T}} \begin{pmatrix} L_{ij} & \frac{L_{ij}^2}{2} \\ \frac{L_{ij}^2}{2} & \frac{L_{ij}^3}{3} \end{pmatrix}^{-1} M_{ij,H} = 2\xi_j + \left(M_i^{\mathsf{T}}\Sigma_i^{-1}\mathcal{T}_{ij}\Sigma_i^{-1}M_i - \mathrm{Tr}\left(\Sigma_i^{-1}\mathcal{T}_{ij}\right)\right)\frac{\xi_j^2 p_0^2}{p_i^2} \tag{V.25}$$

By maximizing the log Likelihood, the next iteration of ξ can be determined:

$$\xi_{j,n+1} = \xi_{j,n} + \frac{\sum_{i=0}^{N_{\mathcal{M}}} \frac{\xi_{j,n}^2 p_0^2}{p_i^2}\left(M_i^{\mathsf{T}}\Sigma_i^{-1}\mathcal{T}_{ij}\Sigma_i^{-1}M_i - \mathrm{Tr}\left(\Sigma_i^{-1}\mathcal{T}_{ij}\right)\right)}{2N_{\mathcal{M}j}} \tag{V.26}$$

where $N_{\mathcal{M}j}$ is the number of muons passing through the voxel j. We made this analysis only in the xz-plane, however it can be made in the yz-plane as well so at each iteration the scattering density can be updated by the mean of the xz contribution and the yz one. The log Likelihood can then be maximized iteratively until the set of scattering density ξ_j converges.

Thanks to the help of our colleagues from the DRT/LIST (**D**irection de la **R**echerche **T**echnologique/**L**aboratoire d'**I**ntégration de **S**ystèmes et des **T**echnologies), this algorithm was implemented in order to analyze the data produced by our instruments and the simulations to predict their behavior. The difference between the two presented methods are shown in Figure V.2. It is a simulation of a MultiGen based instrument imaging three $10 \times 10 \times 10\,\mathrm{cm}^3$ bricks made with CRY and GEANT4. The bottom brick is made of lead, the middle one of iron and the top one of uranium. In this case, the PoCA algorithm can be misleading: due to the acceptance effect, it seems that the middle brick is made of a higher Z material than the two others. Indeed, more detected muons cross the middle region than the external one. However, using the ML-EM method, the Z order of each brick is restored. Moreover, the final image is cleaner so it is easier to identify regions containing material.

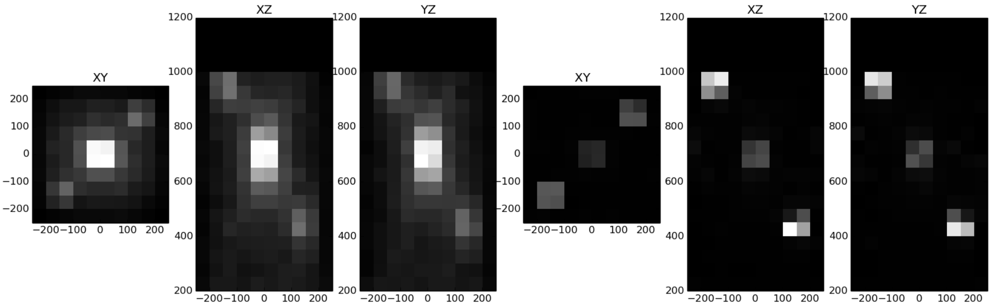

FIGURE V.2 – Simulation to compare between the PoCA method (left) and the ML-EM one (right). Three $10 \times 10 \times 10\,\mathrm{cm}^3$ bricks composed of lead, iron and uranium in ascending order (courtesy of T. Dautremer).

V.C TomoMu experiment

V.C.1 Overview

After the WatTo experiment, a small scale scattering setup has been made in order to make a proof of concept of a scattering setup using multiplexed Micromegas detector. It is a vertical scattering setup designed to image objects of small sizes ($\sim 20\,\mathrm{cm}$) using MultiGen detectors. It is portable in order to make demonstrations in science fairs or during classes. It allows us to test and benchmark the techniques and algorithms that would be deployed in the M^3 setup described in section V.D like the inversion algorithms using the PoCAs method and the ML-EM method.

V.C.2 Experimental setup

The TomoMu scattering setup shown in Figure V.3 is composed of two parts one on top of each other that can be taken apart for an easier transport. Each part can accept two MultiGen detectors in order to track muons. Between these two parts, there is the experimental area which consists of an aluminum plate that can support various objects to image. The acquisition system is the same as for the WatTo experiment. This way it can be plugged everywhere easily using a standard computer power supply. As for the telescopes deployed for the various absorption tomography campaigns, the gas used for the TomoMu operation is supplied by a premixed bottle of T2K gas or a Ar-iC_4H_{10} mixture in $90{:}10$ proportion. The maximum level arm allowed for each doublet is $45\,\mathrm{cm}$ which corresponds to $1\,\mathrm{mrad}$ angular resolution when using detectors with $300\,\mathrm{\mu m}$ position resolution like the MultiGen can achieve so far. In order to systematically test the setup imaging capabilities in various geometries, varnish coated lead bricks have been made. Two sizes were available: $5\times5\times5\ \mathrm{cm}^3$ and $5\times5\times10\ \mathrm{cm}^3$.

V.C.3 Results

The first imaging attempt has been made with a degraded setup were the aluminum plate was not yet present. A wooden chipboard plank was placed in order to hold three objects:

- a pair of pliers
- a broken limestone reinforced with a steel rod insert
- a $5\times10\times10\ \mathrm{cm}^3$ lead brick[1]

This peculiar limestone was brought to us by the LRMH (**L**aboratoire de **R**echerche des **M**onuments **H**istoriques) which is part of a French institution aiming at preserving and restoring the historical and cultural monument heritage. This broken limestone contains a steel rod to reinforce it as shown in Figure V.4d. As described in section V.A.2, they showed a great interest in this new imaging technique.

Using only one day of data and the simple PoCA method, a fine image shown in Figure V.4a was obtained. This plot shows the reconstructed scattering density weighted by the deviation angle for every scattering occurring at an altitude which

---

[1] the coated bricks were not yet ready.

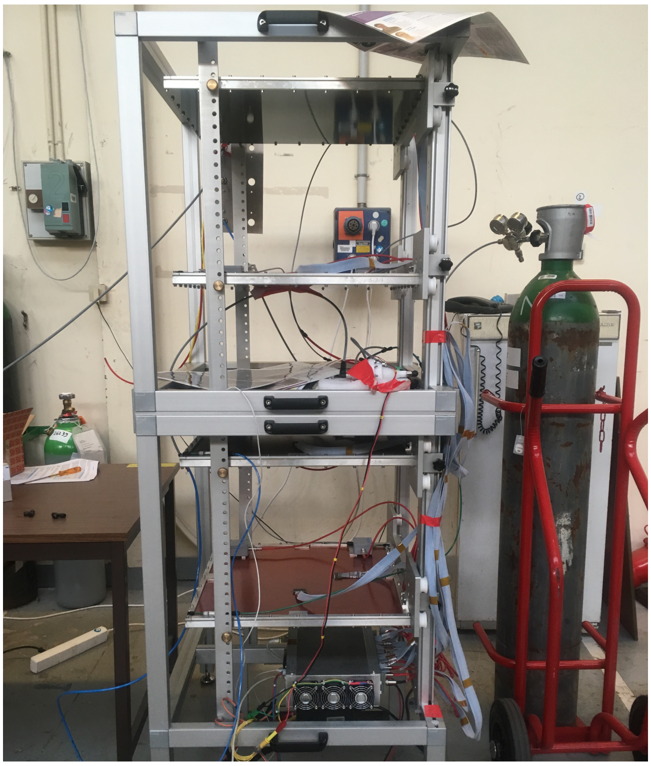

FIGURE V.3 – The TomoMu scattering setup.

is less than 5 cm afar from the wooden plank one. The three objects can perfectly be seen in this image (even if the acceptance effect makes it blurred on the sides), in particular the pliers which can be distinguished easily and the two truncated corners of the lead brick. Moreover, two horizontal separations can be seen at $y \sim 130\,\mathrm{mm}$ and $y \sim 430\,\mathrm{mm}$. These separations correspond exactly to the edges of the wooden plank. Hence, this setup is capable of separating the low density air medium from the medium density chipboard medium. A zoom on the limestone part is shown on Figure V.4b so the steel insert from the surrounding limestone can be distinguished at $x \sim 230\,\mathrm{mm}$ and $y \in [220\,\mathrm{mm}, 270\,\mathrm{mm}]$. This is possible because both the volumetric mass and the mean atomic number of the stainless steel are above the one of the limestone pointed out in Table V.1.

Material	**volumetric mass** $[\mathrm{kgm}^{-3}]$	**Mean atomic number** $\widetilde{Z}$
Lead	1.1×10^4	82
Limestone	$\sim 2.7\times10^3$	10
Stainless steel	$8\ \ \times10^3$	$\sim$26
Air	1.3	7.2
Chipboard wood	$6\ \ \times10^2$	$\sim$6

TABLE V.1 – Material atomic number and volumetric mass.

The performance improvement of the ML-EM method implemented for simulation (as in Figure V.2) can also be checked with real data using TomoMu. 3×10^5 muons were recorded while a lead brick was placed in the imaging area to produce the plots shown in Figure V.5. Unlike the simulation, the improvement is not so large but

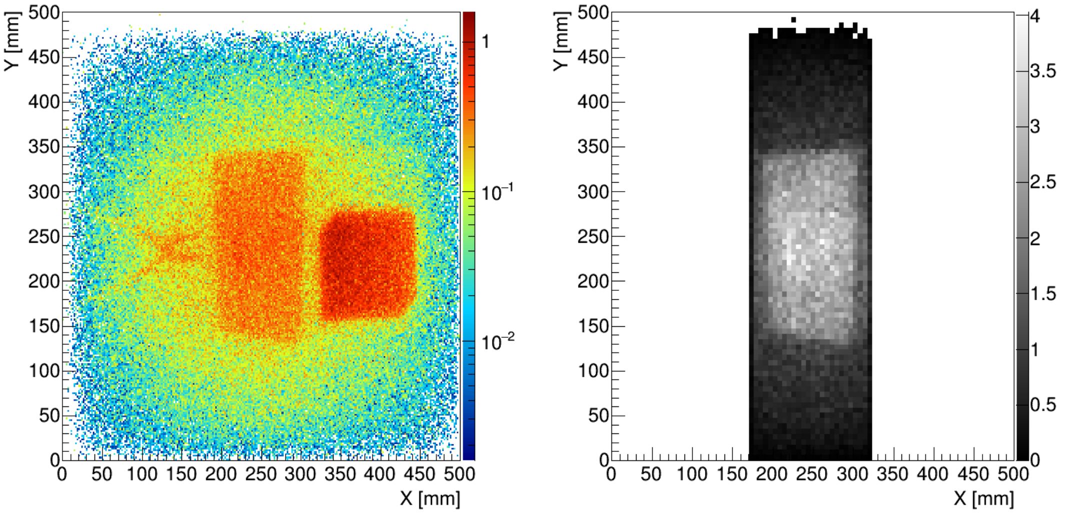

(a) From left to right: a pair of pliers, steel reinforced limestone, lead brick.

(b) Zoom on the limestone to distinguish the steel insert.

(c) Photograph of the imaged objects.

(d) Details of the opened limestone.

FIGURE V.4 – Scattering muography made with the PoCA method.

the scanned volume content is much simpler: without differences of altitude nor differences of atomic number Z.

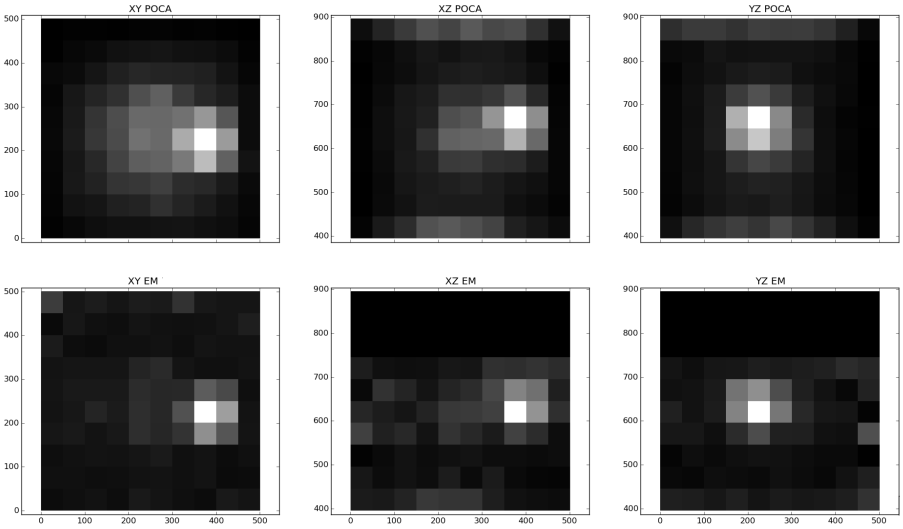

FIGURE V.5 – Tomomu data analyzed using both PoCA (top) and ML-EM (bottom) algorithms (courtesy of T. Dautremer).

Using this setup it is also possible to make an absorption tomography together with a deviation tomography on the same data set. To make the deviation tomography, the scattered muons will be taken into account whereas to make the absorption tomography the straight traveling muons which are detected in both the top and bottom trackers are used. This configuration allows to benchmark both methods and compare them. It was made using a lead brick for a $10\,\mathrm{h}$ long data taking. The results are shown in Figure V.6. The left part corresponds to the absorption results shown as the muon flux expressed in term of accumulated muons. The right part corresponds to the deviation results shown, as before, as the scattering position density weighted by the scattering angle in the altitude interval corresponding to the lead brick. As explained earlier, the use of the incoming tracker, mandatory to make a deviation tomography, allows a faster and more precise imaging. Figure V.6d shows that the lead brick is well visible in only $20\,\mathrm{min}$ of data using the scattering technique while there is no clue of it in the absorption data. Moreover there is already some hints of a high Z material in the $2\,\mathrm{min}$ scattering measure.

During the science days 2016, this setup made repeatedly the image of the letters formed by children using the coated lead bricks using reduced data set corresponding to a $20\,\mathrm{min}$ acquisition.

V.D M^3 experiment

Using the success of the tests made with the small TomoMu setup, a larger setup has been built to image large objects.

V.D.1 Overview

This setup could be built thanks to a grant from the NRBC-E program which funds new techniques to deal with the nuclear, radiological, biological and chemical threats. The goal of the M^3 experiment is to prove the feasibility of a new homeland security imaging apparatus which can detect potential smuggling of SNM (**S**pecial **N**uclear **M**atter) like uranium or plutonium like it was done by Decision Sciences in the US. The goal of the scanner was to image a container in the 20 foot equivalent format. The advantage of muon-based techniques is that they can potentially detect SNM through substantial shielding *e.g.* through lead enclosures. This type of shielding makes the existing X-ray techniques blind to their content.

V.D.2 Experimental setup

The M^3 scattering setup consists in a $4\,\mathrm{m}$ high aluminum frame supporting two trackers. Each of the trackers is composed of two layers separated by $40\,\mathrm{cm}$. These layers are made of four second version MultiGen detectors screwed together to minimize dead zones. The imaged area can then have a $1\,\mathrm{m}^2$ horizontal footprint. The bottom tracker just above the ground has a fixed altitude but the top one can be moved from the top of the bottom tracker to the maximum altitude of $4\,\mathrm{m}$ above the ground. This way, a test container can be placed between the two trackers and be imaged in realistic conditions like it has been done with the container shown in Figure V.7.

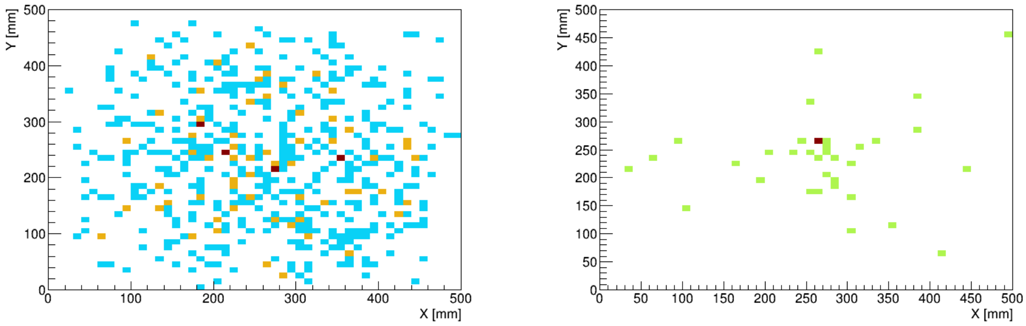

(a) Absorption, 2 min of data.

(b) Scattering, 2 min of data.

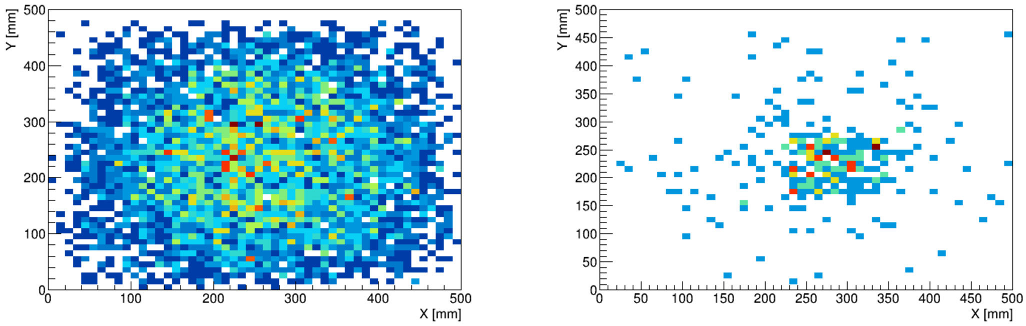

(c) Absorption, 20 min of data.

(d) Scattering, 20 min of data.

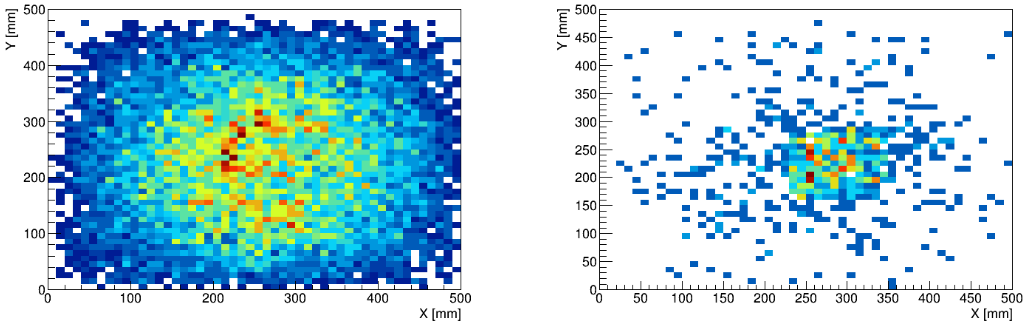

(e) Absorption, 1 h of data.

(f) Scattering, 1 h of data.

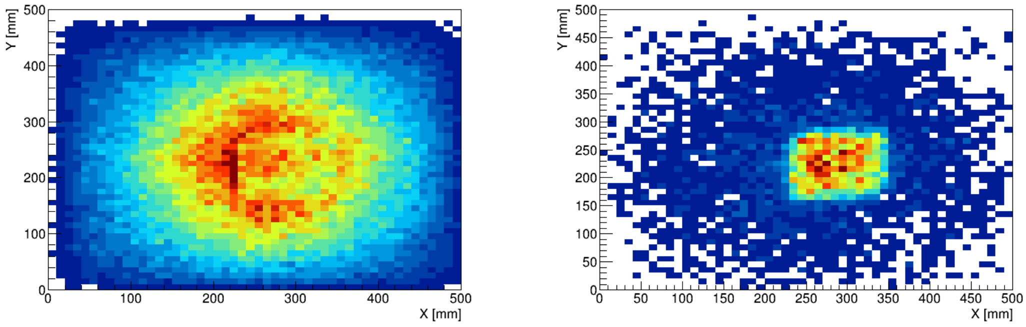

(g) Absorption, 10 h of data.

(h) Scattering, 10 h of data.

FIGURE V.6 – Comparison of both absorption and scattering methods using the same data set.

Each Micromegas layer corresponds to $8 \times 61 = 488$ electronics channels which are read by a dedicated FEU. The four FEUs are synchronized using a TCM board which

FIGURE V.7 – Container installed inside the M^3 setup to be scanned.

can provide a self-trigger. In order to select scattering relevant events, each FEU is setup to send a trigger signal to the TCM if a significant signal is present in 2 DREAMs at the same time but the TCM is firing the event acquisition only in the case that at least three FEUs send a trigger signal. The Micromegas can be flushed by mixtures of argon and isobutane in various proportions thanks to a gas mixing bay. Each doublet has an independent gas supply and the eight detectors of a doublet are supplied sequentially.

V.D.3 Acquisition specificities

Since the cosmic bench is 4 m high, the rigidity of the aluminum frame is not enough to forbid significant movements of the upper tracker compared to the bottom one. This can lead to some variations of the alignment from run to run if not enough care was taken during the manipulations between them. Moreover, several factors make the alignment corrections hard to make. Indeed, the detector position and angles are not measured with a sufficient precision so these parameters are corrected offline using the muon data. By taking calibration data without scattering objects between the two trackers, the straight traveling muons can be used to determine the position and angles of each detectors with a better precision. However, having 16 different detectors, each one having six degrees of freedom, this is a tricky process.

Being an in lab experiment, it was not designed with in-gas temperature and pressure sensors like the telescopes deployed for the absorption experiments. However, the experimental hall is poorly insulated and with a windowed roof. Indeed, high temperature changes have been observed, especially on the topmost detectors under direct sunlight. This effect led to gain variations and a steady current at the hottest hours of the day as shown in Figure V.8.

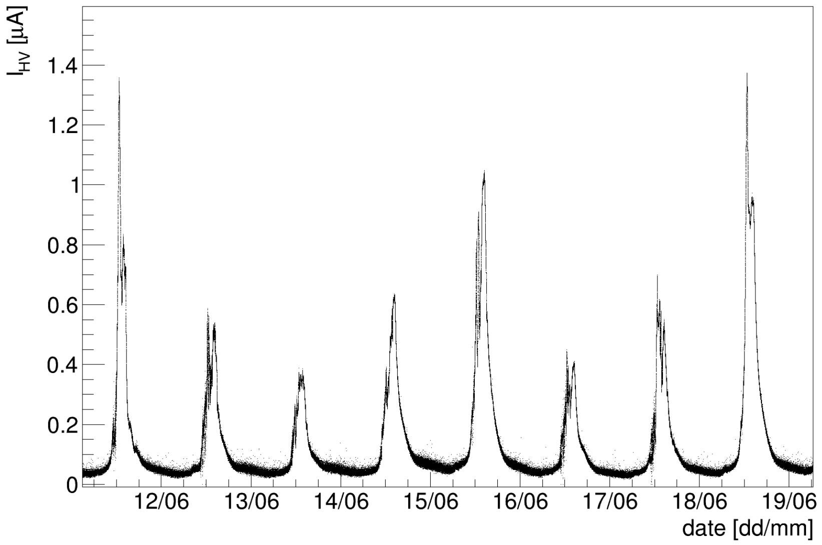

FIGURE V.8 – Time variations of the amplification current in one detector, made with $U_{HV} = 494\,\mathrm{V}$ and an Ar-iC$_4$H$_{10}$ mixture in $95{:}5$ proportion.

V.D.4 Results

Data have been taken in different configurations corresponding to different contents inside the container. To reproduce SNM smuggling conditions, we could use depleted uranium rods, lead bricks to compare with the uranium or to make some shielding and wood-chips bundles to reproduce the effect of standard (*i.e.* low Z) cargo material.

The DNDO (**D**omestic **N**uclear **D**etection **O**ffice) set detection constraints for the validation of measurement techniques: the system must be able to detect a chunk of $4\,\mathrm{kg}$ of uranium in less than $2\,\mathrm{min}$. However, the measure of the location of the uranium is not required in such small time. This way the muon scattering tomography can also be used to make a detection without imaging the volume.

To make rapid detections, the goal is to detect an excess of unusually big scattering caused by high Z material. To do so, the scattering angle distributions measured by scanning a container which does not contain SNM with one containing it has to be compared. A tool that can be used to compare probability distribution is the Kolmogorov-Smirnov test [73, 74]. This test compares two samples of a randomly distributed variable by computing the maximum distance of their cumulative distributions. In our case, for each muon $k \in [\![0, N_j[\![$ of the j^{th} data set containing N_j muons, its scattering angle $\Delta\theta_{jk}$ is computed. The cumulative distribution of muons having a scattering angle below a threshold $\alpha \in [0, \pi/2]$ is then:

$$f_j(\Delta\theta < \alpha) = \frac{\#\left\{k \in [\![0, N_j[\![\mid \Delta\theta_{jk} < \alpha\right\}}{N_j} \tag{V.27}$$

It allows to define a distance $D_{1,2}$ between the distributions from the data sets 1 and 2 as:

$$D_{1,2} = \max_{\alpha} |f_1(\Delta\theta < \alpha) - f_2(\Delta\theta < \alpha)| \tag{V.28}$$

The Kolmogorov-Smirnov test infers that the hypothesis, for the two data sets, to follow the same distribution has the probability $\mathbb{P}_{1,2}$ to be true:

$$\mathbb{P}_{1,2} = 1 - \vartheta\left(\frac{1}{2}; \frac{2iN_1N_2D_{1,2}^2}{\pi(N_1+N_2)}\right) = 2\sum_{l=1}^{\infty}(-1)^{l-1}\exp\left(\frac{-2l^2N_1N_2D_{1,2}^2}{(N_1+N_2)}\right) \tag{V.29}$$

where ϑ is the Jacobi theta function and i is the imaginary unit.

This test can be performed online by comparing the accumulated deviation angle distribution with a reference one. The results are shown in Figure V.9 and demonstrate that it is possible to distinguish between a container filled with wood-chips bags and one also containing depleted uranium rods in 1.1×10^5 events. Indeed, at this point the Kolmogorov probability (black curve) converged below $2\,\%$ which indicates that the two distributions are incompatible. Moreover, a test comparing two containers loaded with uranium (blue curve) show that the compatibility probability converge toward one in even less time (3.5×10^4 events). However, the test between two containers filled with wood-chips converge in a longer time. In fact, the scattering induced by the wood is not negligible with respect to the one in the high Z material because the traveled length ratio is high. So a non-negligible proportion of the events are significantly scattered more than one time inside the container. Nonetheless, the probability is above $80\,\%$ after 1.1×10^5 events. The convergence of these Kolmogorov tests are presented in term of event number instead of time because it depends on the muon rate. Indeed, with larger instruments, this rate will be higher, allowing a faster convergence. Further tests have to be made with more inhomogeneous content inside the container. This crude analysis is only a start and will maybe fail for tests closer to the reality *i.e.* when the container is filled with different materials.

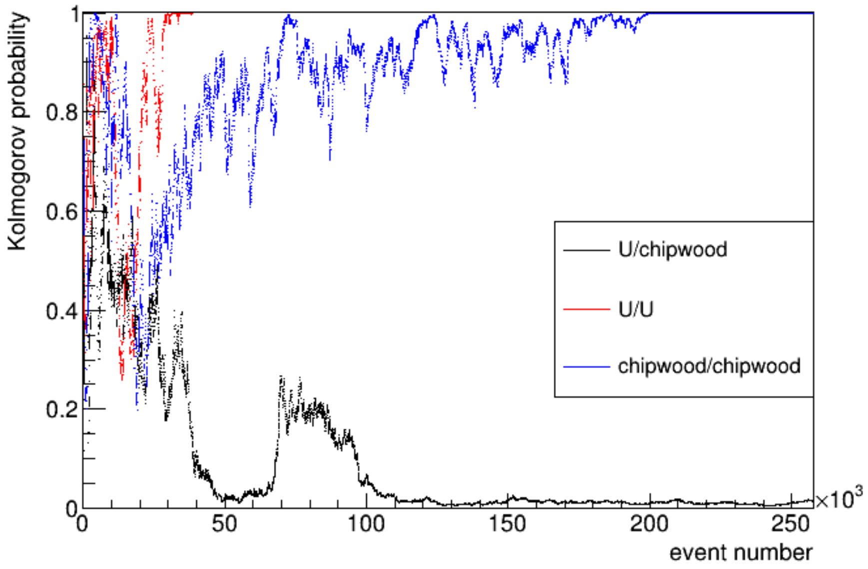

FIGURE V.9 – Kolmogorov probability in function of the accumulated event number in three different configurations.

The imaging capabilities were also checked as shown in Figure V.10. Depleted uranium rods and lead bricks were put inside the container. As expected, the uranium appears brighter than the lead even when considering the acceptance effect.

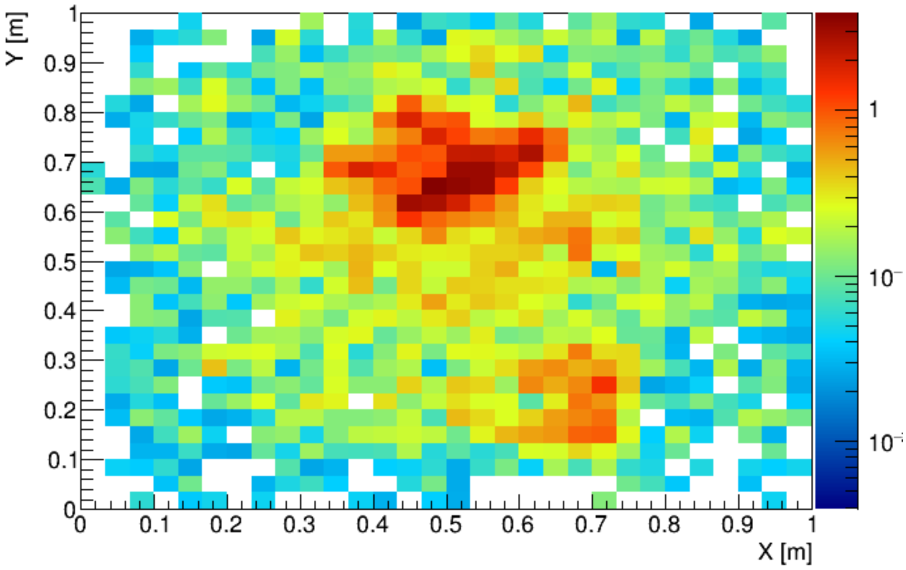

FIGURE V.10 – Scattering tomography using the weighted PoCA method of depleted uranium rods (top) and lead bricks (bottom) in one day.

Conclusion

Starting with only a couple of multiplexed Micromegas with 1D readout in 2014, the Saclay muography group activities has grown fast during these three years. Two generations of prototypes have been designed and massively produced mainly by the ELVIA company. Indeed, 40 detectors have been built which correspond to $10\,\mathrm{m}^2$ of active area. It is the largest total Micromegas detection surface ever built for a single project. Thanks to developments in electronics and detector operation, it was possible to successfully operate Micromegas trackers in the wild, undergoing large variations of both temperature and pressure. Successive improvements of the detector slow control made this operation more and more stable. All these enhancements were made under compactness and power consumption constraints, allowing the production of telescopes for muon tomography. This application which requires the deployment of instruments in the wild is an emerging alternative for an affordable, secure and nondestructive imaging technique. Using the naturally available muons coming from the interaction from the primary cosmic rays with the atmosphere, the density or atomic number content of objects can be determined. Mainly two technologies were used so far for muon tomography: scintillators and nuclear emulsions. Each one has its pros and cons: the former can make dynamic imaging while the latter has the finest resolution. The new Micromegas-based instruments made during this thesis combine the advantages of the two other techniques. They have a much finer granularity than what can be achieved with scintillators and are also suitable for dynamic studies. This performance can unlock new applications for muon tomography.

With the knowledge acquired during this three year work, both during the laboratory test and the water tower experiment, the group is able to run five muography instruments simultaneously at Giza and Saclay. The three telescopes in Egypt are making an absorption tomography of Khufu's pyramid, aiming at confirming or disproving Egyptologists theories about its purpose and construction. An already known cavity has been detected together with a new one which was completely unknown. The smaller Saclay instrument of a quarter square meter is designed to make scattering tomography. It had demonstrated the capability of this technique for various audiences such as during science fairs. The last and largest built instrument is a one meter square demonstrator able to image full containers to develop a special nuclear matter detection and finding technique for a wide range of application from homeland security to nuclear waste monitoring. A container has been scanned, showing that with sufficient detector surface, special nuclear matter can be detected in a few minutes. The performance of such an instrument comply with the DNDO constraints.

Some proofs of concept have been made, eliciting interest in the industry. In one hand, some companies contacted us to make proofs of concept corresponding to their specific field. In the other hand, they wish to collaborate with us in order to commercialize a muography instrument. Furthermore, the data taking campaign in Egypt continues with the ScanPyramids collaboration and funds have been raised for the MIMOSA project. It allows the upgrade of the M^3 instrument from one to two square meters. Moreover, two one square meter telescope for absorption tomography is being built. For applications with compactness constraints, the design of a time projection chamber dedicated to muography has started. In parallel, the flaws of the detector are investigated and a third version is being designed. The resolution problem is being addressed with the upgrade of the resistive layer. The gas leaks are also reduced thanks to the knowledge acquired from other experiments facing the same problem: the ones in space or using expensive gases like krypton.

Appendix A

Khufu's Pyramid height measurement

The same Dracal probe used for the gas monitoring allowed us to measure the altitude of specific locations on the edge of the pyramid in order to precisely replace the muon data results in 3D space.

A.1 Method

Using the pressure gradient, it is possible to compute the altitude knowing the pressure. Indeed, the hydrostatic equation states that:

$$-\vec{\nabla}P + \rho\vec{g} = 0 \tag{A.1}$$

with P the air pressure, ρ its density and $\vec{g}$ the gravitational acceleration. Furthermore, the density can be expressed in term of pressure and temperature T using the perfect gas law:

$$\rho = \frac{PM}{RT} \tag{A.2}$$

where M is the air molar mass and R the perfect gas constant. Supposing that there is no horizontal pressure gradient, the variations of pressure with the altitude follows the equation:

$$\frac{\mathrm{d}P}{\mathrm{d}z} + \frac{Mg}{RT}P = 0 \tag{A.3}$$

where the z axis is the vertical axis pointing upward. If the temperature T_0 is uniform inside the measure range then the pressure P_1 at an altitude z_1 and the pressure P_2 at an altitude z_2 are linked by:

$$P_2 = P_1 \exp\left(\frac{(z_1 - z_2)Mg}{RT_0}\right) \tag{A.4}$$

Knowing the pressure P_0 at the level of the pyramid basis, the height h of a point of the pyramid can then be computed knowing its pressure P:

$$h = \frac{RT_0}{Mg} \ln\left(\frac{P_0}{P}\right) \tag{A.5}$$

A.2 Data taking

Two barometers were used: one staying at the level of the pyramid basis, and another taking data at different location on the surface of the pyramid. The aim of the one staying on the ground was to measure the pressure to be able to make real time comparisons between the two pressures. Another goal, fulfilled by both temperature probes was to check that the temperature uniformity hypothesis was valid. Indeed, the two probes measured a mean temperature of $T_0 = 295.2\,\mathrm{K}$ with $5.8\,\mathrm{K}$ variations.

The probe was carried by professional climbers on the interesting locations of the pyramid surface, making stops in order to stabilize the measurement at these specific locations. The three more interesting location are:

- the summit
- the notch behind witch there is a known cavity
- a smaller notch which can correspond to the location of the discovered C1 cavity.

A.3 Results

Measures of pressure and temperature were made every second so the height can be computed at the same frequency. At each level, $5\,\mathrm{min}$ to $10\,\mathrm{min}$ of data were taken. The results are shown in Table A.1, the systematic error takes into account the temperature variations during the data taking and the precision of the instrument.

Location	**height** $[\mathrm{m}]$
Notch	$81.2 \pm 0.9_{(stat)} \pm 1.6_{(syst)}$
Smaller notch	$118.6 \pm 0.5_{(stat)} \pm 2.3_{(syst)}$
Summit	$141.6 \pm 0.9_{(stat)} \pm 2.8_{(syst)}$

TABLE A.1 – Height of specific location on the Khufu's pyramid surface.

The main source of uncertainty comes from the temperature variations during the data taking. So even if this measurement is compatible with the other summit measurement ($138.8\,\mathrm{m}$), it is less precise than the previous ones.

Bibliography

[1] K Nagamine *et al.* "Method of probing inner-structure of geophysical substance with the horizontal cosmic-ray muons and possible application to volcanic eruption prediction". In: *Nuclear Instruments and Methods in Physics Research Section A: Accelerators, Spectrometers, Detectors and Associated Equipment* 356.2 (1995), pp. 585–595.

[2] Victor Francis Hess. "Über Beobachtungen der durchdringenden Strahlung bei sieben Freiballonfahrten". In: *Z. Phys.* 13 (1912), p. 1084.

[3] C Patrignani *et al.* "Review of Particle Physics, 2016-2017". In: *Chin. Phys. C* 40 (2016), p. 100001.

[4] Scott E Forbush. "On the effects in cosmic-ray intensity observed during the recent magnetic storm". In: *Physical Review* 51.12 (1937), p. 1108.

[5] DJ Cooke *et al.* "On cosmic-ray cut-off terminology". In: *Il Nuovo Cimento C* 14.3 (1991), pp. 213–234.

[6] Dieter Heck *et al.* *CORSIKA: A Monte Carlo code to simulate extensive air showers*. Tech. rep. 1998.

[7] Thomas K Gaisser, Ralph Engel, and Elisa Resconi. *Cosmic rays and particle physics*. Cambridge University Press, 2016.

[8] LN Bogdanova *et al.* "Cosmic muon flux at shallow depths underground". In: *Physics of Atomic Nuclei* 69.8 (2006), pp. 1293–1298.

[9] G Bellini *et al.* "Cosmic-muon flux and annual modulation in Borexino at 3800 m water-equivalent depth". In: *Journal of Cosmology and Astroparticle Physics* 2012.05 (2012), p. 015.

[10] HA Bethe. "Moliere's theory of multiple scattering". In: *Physical Review* 89.6 (1953), p. 1256.

[11] Donald E Groom, Nikolai V Mokhov, and Sergei I Striganov. "Muon stopping power and range tables 10 MeV–100 TeV". In: *Atomic Data and Nuclear Data Tables* 78.2 (2001), pp. 183–356.

[12] William T Scott. "The theory of small-angle multiple scattering of fast charged particles". In: *Reviews of modern physics* 35.2 (1963), p. 231.

[13] CTR Wilson. "Cloud-chamber technique". In: *Proc. Roy Soc*. Vol. 85. 1911, p. 285.

[14] Hans Geiger and Walther Müller. "Elektronenzählrohr zur messung schwächster aktivitäten". In: *Naturwissenschaften* 16.31 (1928), pp. 617–618.

[15] Georges Charpak *et al.* "The use of multiwire proportional counters to select and localize charged particles". In: *Nuclear Instruments and Methods* 62.3 (1968), pp. 262–268.

[16] Albert H Walenta, J Heintze, and B Schürlein. "The multiwire drift chamber a new type of proportional wire chamber". In: *Nuclear Instruments and Methods* 92.3 (1971), pp. 373–380.

[17] Fabio Sauli. "GEM: A new concept for electron amplification in gas detectors". In: *Nuclear Instruments and Methods in Physics Research Section A: Accelerators, Spectrometers, Detectors and Associated Equipment* 386.2-3 (1997), pp. 531–534.

[18] Yannis Giomataris *et al.* “MICROMEGAS: a high-granularity position-sensitive gaseous detector for high particle-flux environments”. In: *Nuclear Instruments and Methods in Physics Research Section A: Accelerators, Spectrometers, Detectors and Associated Equipment* 376.1 (1996), pp. 29–35.

[19] William Shockley. “Currents to conductors induced by a moving point charge”. In: *Journal of applied physics* 9.10 (1938), pp. 635–636.

[20] Simon Ramo. “Currents induced by electron motion”. In: *Proceedings of the IRE* 27.9 (1939), pp. 584–585.

[21] ME Rose and SA Korff. “An investigation of the properties of proportional counters. i”. In: *Physical Review* 59.11 (1941), p. 850.

[22] Herald Genz. “Single electron detection in proportional gas counters”. In: *Nuclear Instruments and Methods* 112.1 (1973), pp. 83–90.

[23] Friedrich Paschen. “Ueber die zum Funkenübergang in Luft, Wasserstoff und Kohlensäure bei verschiedenen Drucken erforderliche Potentialdifferenz”. In: *Annalen der Physik* 273.5 (1889), pp. 69–96.

[24] Heinz Raether. “Electron avalanches and breakdown in gases”. In: (1964).

[25] S Procureur *et al.* “Operation of a resistive Micromegas in air”. In: *Nuclear Instruments and Methods in Physics Research Section A: Accelerators, Spectrometers, Detectors and Associated Equipment* 688 (2012), pp. 75–79.

[26] Ioanis Giomataris *et al.* “Micromegas in a bulk”. In: *Nuclear Instruments and Methods in Physics Research Section A: Accelerators, Spectrometers, Detectors and Associated Equipment* 560.2 (2006), pp. 405–408.

[27] T Alexopoulos *et al.* “A spark-resistant bulk-micromegas chamber for high-rate applications”. In: *Nuclear Instruments and Methods in Physics Research Section A: Accelerators, Spectrometers, Detectors and Associated Equipment* 640.1 (2011), pp. 110–118.

[28] C Bernet *et al.* “The gaseous microstrip detector Micromegas for the high-luminosity COMPASS experiment at CERN”. In: *Nuclear Instruments and Methods in Physics Research Section A: Accelerators, Spectrometers, Detectors and Associated Equipment* 536.1 (2005), pp. 61–69.

[29] Florian Thibaud. “Développement de détecteurs Micromegas pixellisés pour les hauts flux de particules et évaluation de la contribution diffractive à la leptoproduction de hadrons à COMPASS”. PhD thesis. Paris 11, 2014.

[30] P Abbon *et al.* “The Micromegas detector of the CAST experiment”. In: *New Journal of Physics* 9.6 (2007), p. 170.

[31] B Radics *et al.* “The ASACUSA Micromegas Tracker: A cylindrical, bulk Micromegas detector for antimatter research”. In: *Review of Scientific Instruments* 86.8 (2015), p. 083304.

[32] M Byszewski and J Wotschack. “Resistive-strips micromegas detectors with two-dimensional readout”. In: *Journal of Instrumentation* 7.02 (2012), p. C02060.

[33] S Procureur, R Dupré, and S Aune. “Genetic multiplexing and first results with a $50\times50\text{cm}^2$ Micromegas”. In: *Nuclear Instruments and Methods in Physics Research Section A: Accelerators, Spectrometers, Detectors and Associated Equipment* 729 (2013), pp. 888–894.

[34] S Aune *et al.* “Micromegas tracker project for CLAS12”. In: *Nuclear Instruments and Methods in Physics Research Section A: Accelerators, Spectrometers, Detectors and Associated Equipment* 604.1 (2009), pp. 53–55.

[35] S Procureur. “Micromegas trackers for hadronic physics”. In: *Modern Physics Letters A* 28.13 (2013), p. 1340024.

[36] Pascal Baron *et al.* "AFTER, an ASIC for the readout of the large T2K time projection chambers". In: *IEEE Transactions on Nuclear Science* 55.3 (2008), pp. 1744–1752.

[37] S Anvar *et al.* "AGET, the GET front-end ASIC, for the readout of the Time Projection Chambers used in nuclear physic experiments". In: *Nuclear Science Symposium and Medical Imaging Conference (NSS/MIC), 2011 IEEE*. IEEE. 2011, pp. 745–749.

[38] D Attie *et al.* "The readout system for the CLAS12 Micromegas vertex tracker". In: *Real Time Conference (RT), 2014 19th IEEE-NPSS*. IEEE. 2014, pp. 1–11.

[39] S Bouteille *et al.* "Large resistive 2D Micromegas with genetic multiplexing and some imaging applications". In: *Nuclear Instruments and Methods in Physics Research Section A: Accelerators, Spectrometers, Detectors and Associated Equipment* 834 (2016), pp. 187–191.

[40] Atsuhiko Ochi *et al.* "Carbon sputtering technology for MPGD detectors". In: *PoS TIPP2014* 351 (2014).

[41] P Baron *et al.* "Operational experience with the readout system of the MINOS vertex tracker". In: *Real Time Conference (RT), 2016 IEEE-NPSS*. IEEE. 2016, pp. 1–3.

[42] C Adloff *et al.* "Environmental study of a Micromegas detector". In: (2009).

[43] Fabio Sauli. *Principles of operation of multiwire proportional and drift chambers*. Tech. rep. European Organization for Nuclear Research, 1977.

[44] A Sharma and Fabio Sauli. "A Measurement of the first Townsend coefficient in argon based mixtures at high fields". In: *Nuclear Instruments and Methods in Physics Research Section A: Accelerators, Spectrometers, Detectors and Associated Equipment* 323.1-2 (1992), pp. 280–283.

[45] M Frotin *et al.* "Sealed operation, and circulation and purification of gas in the HARPO TPC". In: *arXiv preprint arXiv:1512.03248* (2015).

[46] M Dixit. "Development of high resolution Micro-Pattern Gas Detectors with wide readout pads". In: *Journal of Instrumentation* 5.03 (2010), P03008.

[47] Chris Hagmann, David Lange, and Douglas Wright. "Cosmic-ray shower generator (CRY) for Monte Carlo transport codes". In: *Nuclear Science Symposium Conference Record, 2007. NSS'07. IEEE*. Vol. 2. IEEE. 2007, pp. 1143–1146.

[48] Archana Sharma and Rob Veenhof. "Properties of some gas mixtures used in tracking detectors". In: *SLAC Journal, ICFA* 16 (1998).

[49] Paul VC Hough. "Machine analysis of bubble chamber pictures". In: *International conference on high energy accelerators and instrumentation*. Vol. 73. 1959, p. 2.

[50] EP George. "Cosmic rays measure overburden of tunnel". In: *Commonwealth Engineer* 455 (1955).

[51] Hiroyuki KM Tanaka *et al.* "High resolution imaging in the inhomogeneous crust with cosmic-ray muon radiography: The density structure below the volcanic crater floor of Mt. Asama, Japan". In: *Earth and Planetary Science Letters* 263.1 (2007), pp. 104–113.

[52] F Ambrosino *et al.* "The MU-RAY project: detector technology and first data from Mt. Vesuvius". In: *Journal of Instrumentation* 9.02 (2014), p. C02029.

[53] J Marteau *et al.* "Muons tomography applied to geosciences and volcanology". In: *Nuclear Instruments and Methods in Physics Research Section A: Accelerators, Spectrometers, Detectors and Associated Equipment* 695 (2012), pp. 23–28.

[54] Kevin Jourde *et al.* "Monitoring temporal opacity fluctuations of large structures with muon radiography: a calibration experiment using a water tower". In: *Scientific reports* 6 (2016).

[55] C Cârloganu *et al.* "Towards a muon radiography of the Puy de Dôme". In: *Geoscientific Instrumentation, Methods and Data Systems Discussions* 2 (2012), pp. 765–780.

[56] Arturo Menchaca-Rocha. "Searching for cavities in the Teotihuacan Pyramid of the Sun using cosmic muons experiments and instrumentation". In: *International Cosmic Ray Conference*. Vol. 4. 2011, p. 325.

[57] H Gómez *et al.* "Feasibility study of archaeological structures scanning by muon tomography". In: *AIP Conference Proceedings*. Vol. 1672. 1. AIP Publishing. 2015, p. 140004.

[58] Douglas Bryman, James Bueno, and Joel Jansen. "Blind test of muon geotomography for mineral exploration". In: *ASEG Extended Abstracts* 2015.1 (2015), pp. 1–3.

[59] S Bouteille *et al.* "A Micromegas-based telescope for muon tomography: The WatTo experiment". In: *Nuclear Instruments and Methods in Physics Research Section A: Accelerators, Spectrometers, Detectors and Associated Equipment* 834 (2016), pp. 223–228.

[60] SolidRun. *Hummingboard Carrierboard Professional Documentation*. 2015. URL: `https://wiki.solid-run.com/doku.php?id=products:imx6:hummingboard:hbpro` (visited on 2017-07-01).

[61] SolidRun. *MicroSom i.MX6 Quad Documentation*. 2015. URL: `https://wiki.solid-run.com/doku.php?id=products:imx6:microsom:quad` (visited on 2017-07-01).

[62] Heritage Inovation Preservation. *HIP ScanPyramids*. 2017. URL: `http://www.hip.institute` (visited on 2017-07-01).

[63] Luis W. Alvarez *et al.* "Search for Hidden Chambers in the Pyramids". In: *Science* 167.3919 (1970), pp. 832–839. ISSN: 00368075, 10959203. URL: `http://www.jstor.org/stable/1728402`.

[64] Irwin Sobel and Gary Feldman. "A 3x3 isotropic gradient operator for image processing". In: *a talk at the Stanford Artificial Project in* (1968), pp. 271–272.

[65] John Canny. "A computational approach to edge detection". In: *IEEE Transactions on pattern analysis and machine intelligence* 6 (1986), pp. 679–698.

[66] Kunihiro Morishima *et al.* "Discovery of a big void in Khufu's Pyramid by observation of cosmic-ray muons". In: *Nature* (2017), nature24647.

[67] Konstantin N Borozdin *et al.* "Surveillance: Radiographic imaging with cosmic-ray muons". In: *Nature* 422.6929 (2003), pp. 277–277.

[68] V Anghel *et al.* "Construction, commissioning and first data from the CRIPT muon tomography project". In: *Nuclear Science Symposium and Medical Imaging Conference (NSS/MIC), 2012 IEEE*. IEEE. 2012, pp. 738–742.

[69] P Baesso *et al.* "Toward a RPC-based muon tomography system for cargo containers." In: *Journal of Instrumentation* 9.10 (2014), p. C10041.

[70] Silvia Pesente *et al.* "First results on material identification and imaging with a large-volume muon tomography prototype". In: *Nuclear Instruments and Methods in Physics Research Section A: Accelerators, Spectrometers, Detectors and Associated Equipment* 604.3 (2009), pp. 738–746.

[71] Larry J Schultz *et al.* "Statistical reconstruction for cosmic ray muon tomography". In: *IEEE Transactions on Image Processing* 16.8 (2007), pp. 1985–1993.

[72] Larry Joe Schultz. "Cosmic ray muon radiography". PhD thesis. Portland State University, 2003.

[73] Andrei Nikolaevich Kolmogorov. "Foundations of probability". In: (1933).

[74] Nickolay Smirnov. "Table for estimating the goodness of fit of empirical distributions". In: *The annals of mathematical statistics* 19.2 (1948), pp. 279–281.

université PARIS-SACLAY
ÉCOLE DOCTORALE
PHENIICS
Irfu

Titre : Développement et applications de détecteurs gazeux à micro-pistes pour la tomographie muonique

Mots clefs : Micromegas, MPGD, muographie, technique d'imagerie, pyramides d'Égypte, securité du territoire, matière nucléaire

Résumé : Cette thèse décrit les premiers essais de tomographie muonique par absorption et par déviation en utilisant des détecteurs Micromegas à haute granularité. Cette technique d'imagerie utilisant les rayons cosmiques gratuits, sans dangers et disponibles partout a démontré sa capacité à imager des objets de tailles variées. Afin de construire des outils compacts, précis, et portables, utiliser une voie d'électronique pour lire chaque motif de lecture est impossible. Pour éviter ce problème, des détecteurs multiplexés ont été conçus, testés et mis en situation dans différentes conditions. Il a été tiré parti des dernières améliorations concernant le détecteur Micromegas telles que le multiplexage génétique ou la lecture 2D par pistes sous une couche résistive. Les prototypes qui ont été fabriqués ont atteint une résolution de 300 μm sur une surface d'un quart de mètre carré en ne nécessitant que 61 voies d'électronique.

Grâce à ces détecteurs, des campagnes de prise de données ont été faites, à la fois dans l'environnement semi-contrôlé du centre CEA de Saclay et sur le plateau de Gizeh en Egypte. Ces deux campagnes ont permis d'imager avec succès le chateau d'eau du CEA Saclay ainsi que la pyramide de Khéops et ce malgré les conditions extrêmes que les télescopes à muon ont endurées. Des variations de température de plusieurs dizaines de Kelvin ont été enregistrées alors que l'acquisition de données se déroulait de manière stable, c'est-à-dire que les variations du gain n'impactaient pas le système d'auto déclenchement. Cette stabilité a été rendue possible grâce à un ajustement des hautes tensions vis-à-vis des conditions environnementales. Cela constitue la première mondiale concernant le fonctionnement d'un dispositif de reconstruction de trace à base de Micromégas en extérieur. En parallèle des expériences de muographie par déviation ont été menées. Un dispositif imageant des objets de petite taille est capable de distinguer divers matériaux sur une échelle de temps de l'ordre d'une journée. Une plus grande installation a permis d'imager un conteneur entier. La résolution du problème inverse a été faite en utilisant à la fois l'algorithme simple dit du PoCA ainsi qu celui de maximisation de vraisemblance proposé dans la littérature.

Title: Development and applications of micro-pattern gaseous detectors for muon tomography

Keywords: Micromegas, MPGD, muography, imaging technique, Egyptian pyramids, homeland security, SNM

Abstract: This thesis describes the first attempts to perform both absorption and scattering muon tomography using high granularity Micromegas detectors. This imaging technique using the free, available and harmless cosmic ray muons radiation shows great possibilities to study various sized objects. In order to make compact and precise portable devices, using one channel of electronics per readout pattern is not possible. To avoid this problem multiplexed detectors have been designed, extensively tested and used in numerous conditions. The latest developments in Micromegas design have been used such as the genetic multiplexing and the 2D strip readout using a resistive layer. The prototypes made were able to achieve a 300 μm resolution at the scale of 50 cm while using only 61 channels of electronics.

Using these detectors, muography data taking campaigns have been performed both in the semi-controlled environment of the Saclay site of CEA and in the wild of the Giza plateau in Egypt. These two campaigns succeeded in imaging the CEA Saclay water tower and the Khufu's pyramid despite the extreme conditions endured by the Micromegas muon telescopes. Large temperature variations of a few tens of Kelvin have been recorded together with a stable operation *i.e.* an even gain ensuring a steady self triggering system. This stability was achieved using high voltage variations with respect to the environmental conditions. Together with this very first worldwide operation of a Micromegas-based tracker outside a laboratory, scattering muographies have also been done. A small setup imaging handheld objects performed well in separating various materials in time scales of the order of the day while a bigger 1 m^2 setup allowing the scan of a full container was successfully operated. The inversion of the ill-posed problem of the muon scattering was performed using the crude PoCA method and the maximum likelihood one described in literature.

Université Paris-Saclay
Espace Technologique / Immeuble Discovery
Route de l'Orme aux Merisiers RD 128 / 91190 Saint-Aubin, France